COORDINATED CONTROL OF VSC BASED MULTI-TERMINAL DC (VSC-MTDC) POWER GRID

by

Shimeng Huang

B.S. Tsinghua University, 2008

M.S. University of Pittsburgh, 2010

Submitted to the Graduate Faculty of
the Swanson School of Engineering in partial fulfillment
of the requirements for the degree of

Doctor of Philosophy

University of Pittsburgh

2015

UNIVERSITY OF PITTSBURGH

SWANSON SCHOOL OF ENGINEERING

This dissertation was presented

by

Shimeng Huang

It was defended on

July 8, 2015

and approved by

Zhi-Hong Mao, Ph.D., Associate Professor

Gregory Reed, Ph.D., Professor

Ching-Chung Li, Ph.D., Professor

Thomas McDermott, Ph.D., Assistant Professor

William Stanchina, Ph.D., Professor

Mingui Sun, Ph.D., Professor

Dissertation Advisors: Zhi-Hong Mao, Ph.D., Associate Professor,

Gregory Reed, Ph.D., Professor

COORDINATED CONTROL OF VSC BASED MULTI-TERMINAL DC (VSC-MTDC) POWER GRID

Shimeng Huang, PhD

University of Pittsburgh, 2015

Voltage source converter based multi-terminal DC (VSC-MTDC) system has raised great interest in academia and power industry. The maturing VSC technology has made such system possible for future medium and high voltage applications. Inspired by the success of DC based power distribution on electric ships, a number of VSC-MTDC systems have been proposed in literature for power grid innovation. However, there are still major technology obstacles to overcome before a VSC-MTDC grid come to utilization. Compared to the maturing technology on device level, research is still needed on the system and operation level. High dynamics and controllability of the VSC brings both opportunity and risks. Controllers must be carefully designed on grid level to fulfill multiple control objectives and coordinate local converter actions.

This work provides a comprehensive solution for MTDC system from modeling to control design. The procedure and tool sets are designed to be applied to various system setups and control schemes, so that it can be applied to multiple MTDC applications. First, thorough study on the VSC-MTDC system is conducted through analytical modeling and simulation. A systematic modeling method for general VSC-MTDC system is proposed. It contains a two-stage procedure that is generalizable to arbitrary system setup and configuration. A small signal state space representation which includes local and network dynamics can be obtained. A novel reconfigurable controller concept is then proposed to address multiple control strategies and communication constraints in system level. Design of such controller is formulated into a standard LMI optimization problem so it can be efficiently solved even for large scale system. Using the proposed control design method, different control schemes can be easily explored through unified methodology and procedure. We demonstrated that existing control schemes for MTDC power balancing can be covered by this control structure.

The proposed modeling and control design method is applied to four-terminal HVDC systems of multiple grid applications. Different control topologies and operation modes are evaluated and compared. Practical aspects such as LMI parameter tuning guideline and specifications for different applications are discussed.

TABLE OF CONTENTS

LIST OF TABLES

LIST OF FIGURES

PREFACE

I would like to express my most sincere and deepest gratitude to my advisor, Dr.Zhi-Hong Mao, for his support and guidance. He has been a great mentor in academia and a respectfully kind friend in life. I would also like to thank my co-advisor, Dr. Gregory Reed, for guiding me through amazing research projects and industrial collaboration, which have greatly inspired this dissertation.

I would like to further extend my thanks to my dissertation committee: Dr. Ching-Chung Li, Dr. Thomas McDermott, Dr. William Stanchina, and Dr. Mingui Sun. Their advise and support have motivated me to improve and complete this study.

In addition, I wish to thank my parents, Zhelin Huang and Weiping Ke, as well as my beloved family, for always being supportive to my choices and believing in me.

Finally, thanks to Junqing Wei, my soul mate and dear husband, for his love and respect, and for always inspiring me to become a better self. It has been a long and hard journey, but you make it filled with adventure and fun.

1.0 INTRODUCTION

1.1 BACKGROUND AND MOTIVATION

The past two decades witness the emerging of DC based power technology. With an ever increasing number of installation, systems like high-voltage DC (HVDC) and static compensator (STATCOM) have proved their merit in today's power industry. Inspired by the fast development in power electronics and the worldwide growing demand on upgrading existing power systems, more innovative DC systems have been proposed. As a promising solution for renewable power integration, Multi-terminal DC(MTDC) system is one of the technology that is becoming a vibrate research area while also raise interests in power industry.

It is generally believed that the AC-DC voltage source converter (VSC) is to be used to construct a MTDC grid. This type of converter is a relatively new invention that utilize insulated gate bipolar transistor (IGBT) to have full control of gate switching. Compared to conventional current source converter (CSC), a.k.a line-commutated converter (LCC), VSC allows easier extension to MTDC and support various network topologies. Even in a back-to-back DC setup, VSC has the advantage of reducing requirement on AC stiffness and supporting change of power flow direction. In recent years, VSC has reached to maturity with increased power rating and efficiency, making VSC-MTDC possible for multiple high-voltage and medium-voltage applications.

The idea of medium-voltage MTDC power distribution was first proved on electric ship design, and is now taken to distribution grid by pioneering researchers [1]. The light-weight interface with AC and DC renewable source has made it an attractive alternative for micro-grid backbone. Quite a number of publications on VSC-MTDC are devoted to the application for off-shore wind power collection [2, 3, 4, 5, 6]. It becomes competitive choice against AC grid due to the better property of underwater DC transmission cable. In the transmission area, some recent conceptual designs propose to use MTDC system for power sharing and frequency support among multiple AC areas [7, 8, 9]. A meshed MTDC supergrid is also believed to be the most possible backbone of a pan-European interconnected system that allows the massive integration of renewable energy sources in the system [10, 11].

Despite its great potential in the future power grid, VSC-MTDC still need to overcome major obstacles before coming to reality [10, 7]. Besides fundamental technical barrier like DC circuit protection, there are still many unknowns from the control and operation perspective:

- Compared to existing power system structures, MTDC's are mostly in conceptual and planning stage, we are in general lack of data, models and simulation tools to understand the system dynamics. There is also little knowledge on system's transient and steady-state response to disturbance and faults.

- There is no determined control and communication architecture. It is a large design space to explore for engineering the system to desired function within realistic constraints.

- There is no standard for DC grid. Control and operation objectives are not as well defined as in AC grid.

- We are still lack of knowledge on the interaction between a MTDC and existing AC grid, and how it will impact the grid stability.

Generally speaking, high dynamics and controllability on the VSC terminals brings both opportunity to improve dynamics of existing grid as well as risk of introducing undesired control conflicts, which may end up disturbing the overall system stability. Therefore, systematic procedure need to be developed to determine and weigh control objectives and design control and communication accordingly. Stability need to be considered carefully on the grid level. And control and communication structure must be able to coordinate the control action of all converters.

1.2 RESEARCH OBJECTIVE

The objective of this study is to modeling and study interactions among converters in a DC grid, develop a control design method that can coordinate local controllers to stabilize the grid and achieve optimal operation in system level.

The subject under study is a VSC-MTDC network, which can be connected with varieties of AC components, including local wind generation, loads(constant power loads and motors), and AC transmission lines connecting with other AC areas. Such system (Figure 1(a)) can be applied as backbone of a microgrid or a DC segmentation out of future transmission network. The basic structure of the research subject is a meshed DC network shown in Figure 3(a). It has VSC's on edge nodes, serving the connection between DC and AC systems. And within the DC system, connections without converter are possible. This structure cannot support arbitrary DC voltage level transforming. Therefore DC-DC converters will be required when transmission is merging to distribution, or when the system contains DC storage or DC renewable sources (e.g. solar power). This leads to a more complex network with a hybrid of DC-DC and DC-AC converters (Figure 1(c)). Due to the lack of mature design of grid level DC-DC converter, existing research on multi-terminal DC system mainly focused on the basic DC network in Figure 3(a).

The essence of the problem is that there are multiple interconnected but physically distributed devices with fast dynamics and high controllability, each serves its own local performance objectives. Control must be designed in a way to coordinate their actions, so the local objectives can be achieved without threatening stability of the networked system. The feature of this work is that we consider the physically interconnected system as a whole instead of decomposing it into local subsystems. Stability issues imposed by interconnections will be studied. We then design a hierarchical control structure to both fit the distributed nature of the MTDC grid and coordinate the subsystems to stabilize the overall networked system. The main goal of this thesis is to:

First Establish analytical model for the full VSC-MTDC system. Then conduct thorough study on its dynamics.

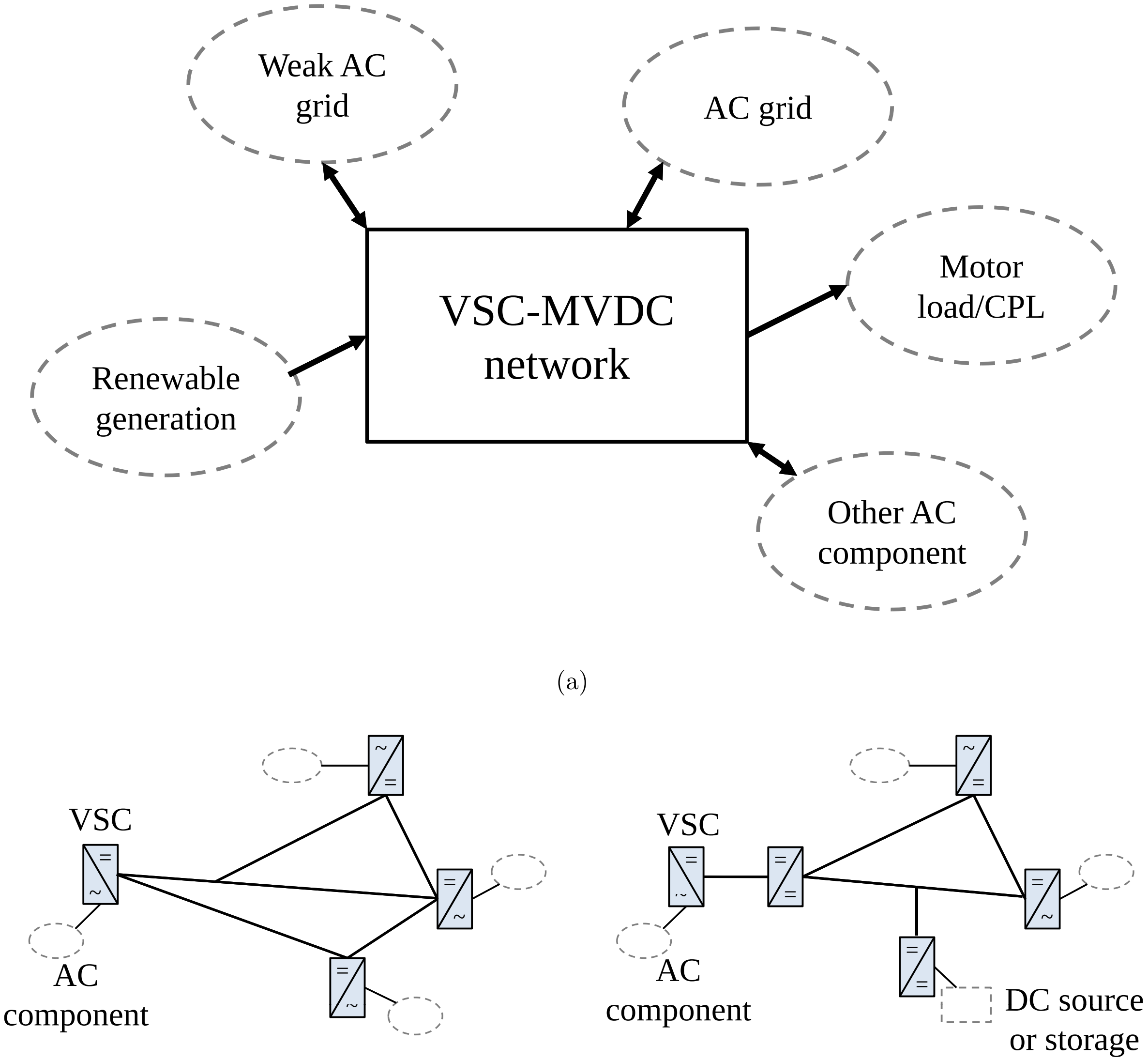

(a)

(b)

(c)

Figure 1: Abstract representation of research subject

Second Design a reconfigurable control architecture with corresponding optimization algorithm. So we can explore different control schemes through a unified methodology, and find the proper controller for the VSC-MTDC system to coordinate the converters' action.

1.3 CONTRIBUTIONS OF THE THESIS

This study proposes a systematic and innovative procedure to model VSC-MTDC system and formulating control problems. The principles, procedure and controller structure developed from this study can be generalized to multiple MTDC applications. The main contributions of the thesis are:

- A systematic modeling method for general VSC-MTDC system. The procedure contains two stages that decouples modeling on local and network level. Moreover, all directional quantities are defined without loss of generality. So it can be applied to arbitrary system configurations with different network topology and various AC-side components. Additional routines such as model assembling, adjustment and operating point solution are proposed to deal with various practical modeling issues.
- Identify local and global control objectives of MTDC systems, understand their couplings from a thorough study of existing local controls and applications of VSC.
- A novel reconfigurable controller concept based on state feedback control. It addresses multiple control topologies and communication constraints by setting feedback gain matrix into a set of nonzero patterns. Several existing control schemes can be covered under this unified formulation.
- Formulating the control problem into a standard LMI optimization so it can be efficiently solved efficiently by several third party tools. Practical aspects such as specification for different MTDC applications and convergence improvement are discussed.
- A detailed guideline of LMI parameters tuning for MTDC system control design. By tracking the movement of eigenvalues, different sets of parameters are identified to address

two main pair of trade-off: trade-off between control performance and cost; and trade-off between local and global control objectives.

In summary, this thesis provides a comprehensive solution for MTDC system from modeling to control design. The whole procedure and tool sets are designed to be applied to various system setups and control schemes, so that it can be applied to general MTDC studies.

1.4 OUTLINE OF THE THESIS

The study is conducted by analytical modeling, theoretical analysis and time domain simulations. The outline of the thesis is:

Chapter 2 A short literature review on converter technologies, VSC-MTDC control methods and general control theories on interconnected systems.

Chapter 3 Propose a systematic and unified modeling method for general VSC-MTDC systems. It is a two-stage procedure that provides proper isolation between modeling at subsystem level and network level, so that it can be applied to arbitrary system configuration with different network topologies and various AC-side components. At subsystem level, existing VSC control schemes and applications are thoroughly reviewed, modeled and simulated. At system level, small signal state-space representation is derived.

Chapter 4 Several state space tools are introduced for MTDC analysis and control design. A reconfigurable state-feedback controller for MTDC system is proposed to address different control topologies and communication constraints. And a LMI optimization problem is formulated to solve the controller.

Chapter 5 The proposed modeling and control design method is applied on a four-terminal HVDC system. Four different control topologies is tested by configuring the gain matrix

K into different nonzero patterns in LMI algorithm. Under each control schemes, we demonstrate the tuning of LMI coefficients and study the resulting close-loop eigenvalues and time domain performance.

Chapter 6 Another test case of off-shore wind integration is studied. The slow local dynamics of wind farm connected VSC is modeled using our two-stage modeling procedure. The proposed control design method is then applied to address 3 possible operation modes of wind integration system.

Chapter 7 Summarizes the thesis and provides suggestions for future work.

2.0 LITERATURE REVIEW

2.1 CONTROL OF VSC-MTDC SYSTEM

Modeling and control of a single VSC has been extensively studied in the past two decades [12, 13, 14]. The most outstanding achievement is enabling the independent control of real and reactive power exchange, which has become the key feature of the converter. VSC-based technology on STATCOM and back-to-back power transmission has been proven to be of great merit. It is generally believed that DC technology can help improve the controllability of the power system. For instance, Clark et al. [15] propose to segment large AC grid with back-to-back HVDC interconnection, and use its controllability on power flows to prevent propagation of disturbance. However, when extended to multi-terminal system, the network topology somewhat downgrade the controllability on power flow. Van Hertem et al. [10] pointed out that though each terminal can independently control the power exchange between its AC and DC sides, flow congestion and DC voltage instability are still possible to occur. In fact, accurate power flow control is considered a major challenge of some MTDC system.

In a DC power network, change of voltage is in fact capacity charging and discharging due to the change of power flow. In a back-to-back HVDC system, balancing of input and output power is done by setting one converter to DC voltage control mode [14]. It has long been suggested to extend this strategy to MTDC system by having one slack converter in DC voltage control mode so that the others can freely decide its power injection [6, 16, 8]. However, this design requires the slack converter to swallow all input/output power difference. Besides, there is no guarantee that the DC voltage on the rest converters would stay within a proper range for the VSC to operate [14].

Some other works [17, 18] propose a distributed control scheme for the DC voltage, which let all converters share the task of power balancing. These works point out the similarity between AC frequency control and DC voltage control, and propose a simple droop control to achieve global power balancing by local observation and control. The benefit of droop control is to avoid conflicts between set values on distributed converters. However, unlike AC system, there does not exist a nominal voltage in a DC system. Chaudhuri et al. [19] have shown that local droop control may perform poorly because of this reason. To tackle this problem, Berggren et al. and Chaudhuri et al. [20, 19] propose to use global observation, which requires communication between converters.

Despite these efforts to improve droop control performance, it is after all a P controller. In AC system, secondary control (i.e. automatic generation control (AGC)) is required to complement its static error. The same control scheme is briefly suggested for DC system in [10]. However, the essential assumption of AGC is that the nominal frequency is the same in the entire interconnected system [21]. It can be implied that it is unlikely to directly transfer the primary and secondary control scheme onto DC system, especially for large scale DC grid. In a word, we believe there are great opportunities to explore innovative control design for the future MTDC grid. And it must be carefully designed to coordinate the control actions on all converters.

2.2 CONTROLLER STRUCTURE OF INTERCONNECTED SYSTEM

An MVDC system generally is a large, interconnected network. Mathematical description of this network involves differential and algebraic equations with a high-dimensional variable space. The network also requires the coordination of a large number of local actions. Either an entirely decentralized or centralized control structure cannot handle the high dimensionality in MVDC control satisfactorily. Existing methods for on-line control are focused at the local level and are mostly decentralized, non-cooperative designs (Figure 2(a)). These designs can reduce dimensionality in control, but local controllers lack global observation of the subsystems in the MVDC grid and thus cannot achieve high performance network-wide [22].

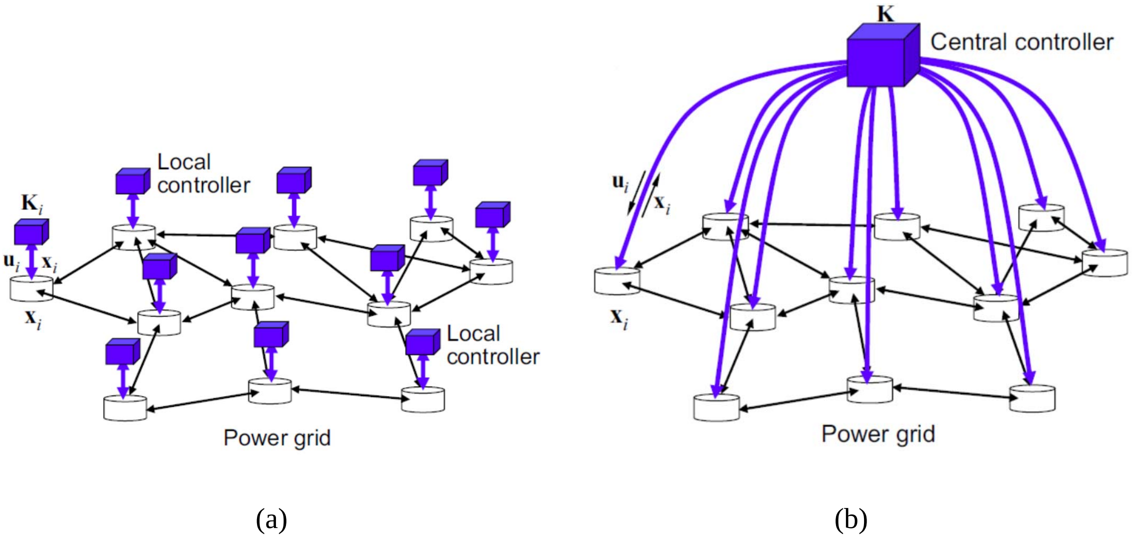

Figure 2: Abstract network representations of (a) a decentralized, non-cooperative control architecture and (b) an entirely centralized control architecture

In contrast, centralized control (Figure 2(b)) can achieve globally optimal performance, assuming that the central controller has sufficient power of computation and there are no delays or losses of data during communication. However, the reality is that the control system must face both computational and communicational constraints. In particular, when communication constraints such as time delays are present, a centralized architecture of control is potentially inferior to a tmore decentralized one [23].

Compared with entirely decentralized or centralized control, hierarchical control with cooperative components has been a more popular choice of control architecture [24]. A large body of existing literature has been contributed to the decentralized, cooperative control for large-scale systems (e.g., see survey papers and books [25, 26, 27, 28]). The optimal design of decentralized and cooperative control has been widely studied since at least the 1970s (e.g. [29, 30, 31]). In recent years, a trend has been to converge control, communication, and computation in the design of decentralized structure for networked control systems [32, 33]. In most of the existing research works, the topology of the control and communication structure is known prior to synthesis, and optimal design for decentralized or distributed control is performed subject to this particular structure.

3.0 MODEL OF MTDC SYSTEM

In this chapter, we introduce a systematic procedure to obtain small signal representation of MTDC systems. Figure 3(a) illustrates a typical MTDC system, which consists of multiple converters interconnected through DC cables. We assumed that all converters are VSC's, and they each could connect to a different type of AC system, such as AC power grid, wind farm, and load, etc. The entire MTDC network can be divided into subsystems that are coupled through DC grid. A subsystem, as shown in Figure 3(b), is defined to represents the local dynamic of a converter together with its AC-side component. To obtain analytical model of the MTDC network, we follow a two-stage procedure: converter modeling and DC grid modeling. It provides proper isolation between modeling at subsystem level and network level, so that the modeling method is generalizable to arbitrary system configuration, such as different network topologies and various AC-side components for individual converters. Besides, the resulting model can be easily reconfigured when the system is changed, making it convenient to explore different designs of a MTDC.

In Section 3.1, state space models of various VSC subsystems is derived and simulated. In Section 3.2, DC network model is introduced, and subsystem models are assembled together into the overall system model. Finally in Section 3.3, a numerical routine is presented to solve the operating point of the small signal model.

3.1 MODEL OF VSC SUBSYSTEM

In the first stage of our modeling procedure, state space representations of each subsystem are derived. Note that subsystem-level control is also modeled at this stage. The state space

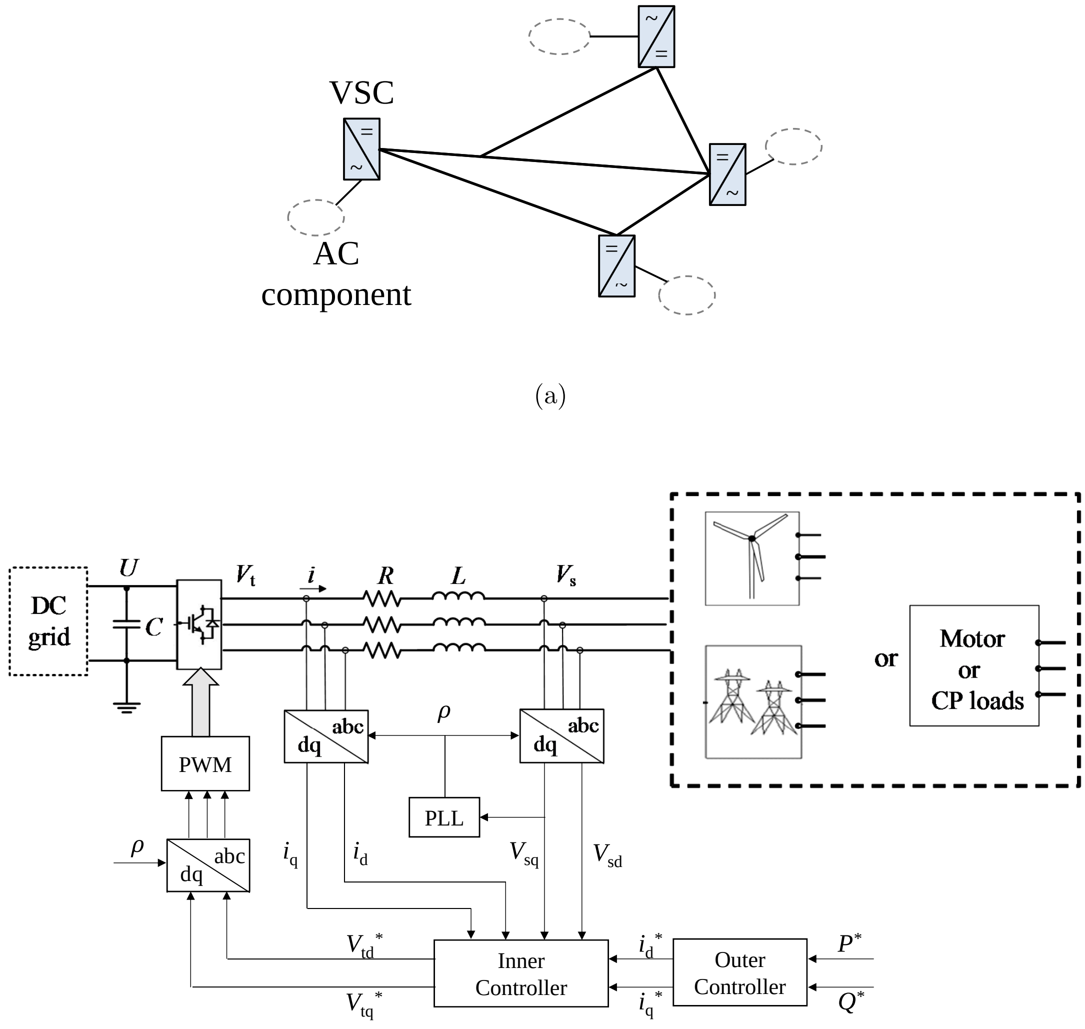

(a)

(b)

Figure 3: Decompose the modeling of MTDC: (a) A MTDC system (b) A subsystem consists of a converter and its AC-side component

model is a set of first-order differential equations describing the subsystem's small signal dynamic behavior, which can be expressed in a matrix form of

$$\dot{\mathbf{x}}_k = \mathbf{A}_{kk}\mathbf{x}_k + \mathbf{B}_k\mathbf{u}_k + \mathbf{B}_{ck}\mathbf{u}_{ck}, \tag{3.1}$$

where k is the index of the kth terminal in MTDC. In (3.1), $\mathbf{x}_k$ is local state variables of the subsystem, which are obtained from both AC-side and DC-side equations of terminal k. The inputs are divided into two groups: $\mathbf{u}_k$ represents local inputs that can be determined within a subsystem; $\mathbf{u}_{ck}$ are inputs that are influenced by other terminals, such as DC current flows into or out of a converter. Variables in $\mathbf{u}_{ck}$ are temporarily modeled as input at this stage, their dynamic behavior will be studied in Section 3.2.

Mathematical modeling for VSC connecting to varieties of AC systems can be found in the literature. These include stiff or weak AC grid [34, 35, 16], wind generation [36], and constant power load [37]. Like these works, we use average model [38, 13] to represent the converters in this paper. Switching of power electronics inside VSC is not modeled, because it is much faster than AC or DC-side dynamics under study. Converter's average model provides sufficient approximation for the purpose of system stability analysis and control design while greatly reduced model's complexity. In this section, VSC subsystem models for several major converter applications is introduced.

3.1.1 VSC connecting to AC power grid

We follow a modeling procedure similar to [13] to obtain (3.1) for VSC connecting to AC power grid. Equivalent circuit of the subsystem is shown in Figure 4. On the AC-side, VSC is connected to the grid through a phase reactor and a transformer. Together they can be represented by a combined impedance $Z = R + j\omega L$. On its AC-side, VSC can be viewed as a three-phase AC voltage source V_t. So the basic equation of this circuit is :

$$V_\text{t} - V_\text{s} = Ri + L\frac{di}{dt},$$

in which V_s is the AC system voltage at the point of common coupling(PCC).

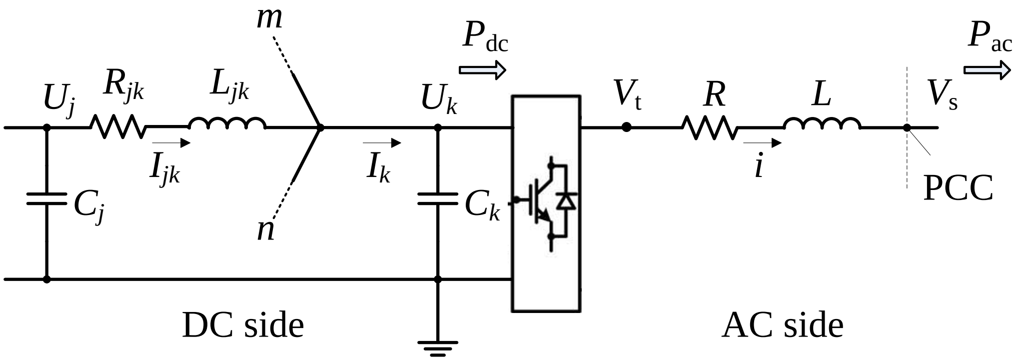

Figure 4: Equivalent circuit of a VSC

The equation is then transformed to a synchronized rotating *dq* reference frame:

$$\begin{aligned}\frac{di_{\mathrm{d}}}{dt} &= -\frac{R}{L}i_{\mathrm{d}} + \omega i_{\mathrm{q}} + \frac{1}{L}(V_{\mathrm{td}} - V_{\mathrm{sd}}) \\ \frac{di_{\mathrm{q}}}{dt} &= -\omega i_{\mathrm{d}} - \frac{R}{L}i_{\mathrm{q}} + \frac{1}{L}(V_{\mathrm{tq}} - V_{\mathrm{sq}})\end{aligned} \tag{3.2}$$

Note that the *dq* transformation projects three-phase quantities onto two orthogonal axes *d* and *q*, which are rotating synchronically with PCC voltage V_{s}. The synchronization is implemented by a phase-lock loop(PLL) that align V_{s} with one of the axes. In this paper, it is arbitrarily assumed to be the *d* axis. As long as PLL remains stable, equation:

$$V_{\mathrm{sd}} = |V_{\mathrm{s}}| \;\text{ and }\; V_{\mathrm{sq}} = 0 \tag{3.3}$$

always hold. The purpose of *dq* transformation is to reduce control complexity: First, it brings the three-phase quantities down to two-dimensional, leading to simpler control structure; Second, the rotating reference frame transform sinusoidal signals to DC like quantities, which greatly reduces the requirement on controller bandwidth. As a result, control on *dq* reference frame is widely deployed in VSCs.

Real and reactive power output to AC grid can be expressed in *dq*-frame quantities by the following derivation:

$$\begin{aligned} P + jQ &= V_{\mathrm{s}} \cdot i^* \\ &= (V_{\mathrm{sd}} + jV_{\mathrm{sq}})(i_{\mathrm{d}} - ji_{\mathrm{q}}) \\ &= (V_{\mathrm{sd}} i_{\mathrm{d}} + V_{\mathrm{sq}} i_{\mathrm{q}}) + j(V_{\mathrm{sq}} i_{\mathrm{d}} - V_{\mathrm{sd}} i_{\mathrm{q}}) \end{aligned} \tag{3.4}$$

Substitute (3.3), we got

$$\begin{aligned} P &= V_{\mathrm{sd}} i_{\mathrm{d}} \\ Q &= -V_{\mathrm{sd}} i_{\mathrm{q}} \end{aligned} \tag{3.5}$$

AC and DC-side dynamics of VSC is related through the conservation of real power. As shown in Figure 4, when ignoring the loss on switching and phase reactor, real power entering the converter's DC-side should equal to that being injected to AC grid, i.e.

$$P_{\mathrm{dc}} = P_{\mathrm{ac}} = P.$$

While P is expressed in (3.5) on the AC-side, it should subject to the following relation on DC-side: real power taken from DC grid at terminal k is the sum of the power converted to AC and the instant charging on large capacitor C_k. This derives:

$$\frac{dU_k}{dt} = -\frac{1}{C_k}\frac{P}{U_k} + \frac{1}{C_k} I_k.$$

The nonlinear DC-side equation can be linearized around operating point P_0 and U_{k0} as

$$\frac{dU_k}{dt} = -\frac{1}{C_k U_{k0}} P + \frac{P_0}{C_k U_{k0}^2} U_k + \frac{1}{C_k} I_k \tag{3.6}$$

Combining (3.2),(3.5),and (3.6), we have the open-loop state space model of a converter connecting to a strong AC grid in form of (3.1):

$$\begin{bmatrix} \dot{i}_{\mathrm{d}k} \\ \dot{i}_{\mathrm{q}k} \\ \dot{U}_k \end{bmatrix} = \begin{bmatrix} -\frac{R_k}{L_k} & \omega_k & 0 \\ -\omega_k & -\frac{R_k}{L_k} & 0 \\ -\frac{V_{\mathrm{sd}k}}{C_k U_{k0}} & 0 & \frac{P_{k0}}{C_k U_{k0}^2} \end{bmatrix} \begin{bmatrix} i_{\mathrm{d}k} \\ i_{\mathrm{q}k} \\ U_k \end{bmatrix} + \begin{bmatrix} \frac{1}{L_k} & 0 \\ 0 & \frac{1}{L_k} \\ 0 & 0 \end{bmatrix} \begin{bmatrix} V_{\mathrm{td}k} - V_{\mathrm{sd}k} \\ V_{\mathrm{tq}k} - V_{\mathrm{sq}k} \end{bmatrix} + \begin{bmatrix} 0 \\ 0 \\ \frac{1}{C_k} \end{bmatrix} I_k \tag{3.7}$$

Since the object of this research is MTDC grid-level control, the converter-level controllers are considered as part of the modeling work. Instead of designing innovative control scheme

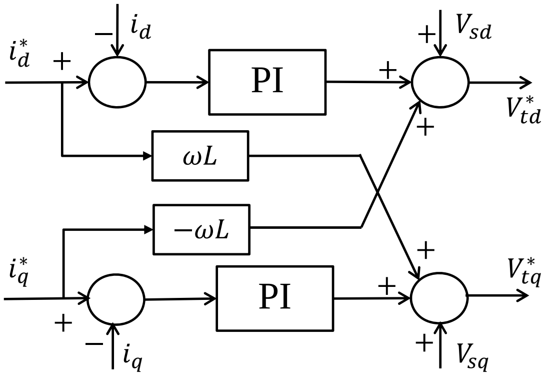

Figure 5: Control diagram of the inner-loop current controller

for converters, we just model the behavior of existing controllers that are commonly used in VSCs. A common control design for VSC contains two cascaded control loops: a current control inner-loop and an application-specific outer-loop. Feedforward decoupling technique and PI controller are used to achieve independent control of real and reactive power that is being exchanged with the AC grid. The controllers are introduced and close-loop model of the subsystem is derived in the following sections:

3.1.1.1 Current control inner-loop We first assume the AC system is stiff, so voltage V_{sd} and V_{sq} remains constant. The current i that flow through phase reactor can then be controlled through converter's AC voltage V_{td} and V_{tq}, which is the control input of VSC.

Figure 5 shows the block diagram of inner controller. It contains a cross feedforward compensate path to cancel out the coupling term between d axis and q axis in (3.7). The decoupled open-loop system has first order dynamics between i and V_{t} on both axes, each can be controlled by a PI controller. On d axis, to have i_{d} tracking a reference value i_{d}^*, inner controller takes the control error and output a set value V_{td}^*. The same structure is also used on q axis. The two control outputs can then be transformed back to a three-phase quantity. Note that the set value of V_{t} still need to be transformed into PWM signal and executed by converter. But the delay of this procedure is negligible compared to the dynamics of (3.7).

To model the close-loop system with inner PI controller in state space, augment the open-loop model (3.7) with states $\mathbf{z}$ introduced by the I controllers, i.e. the integrated errors on d and q branch:

$$\begin{bmatrix} \dot{\mathbf{x}} \\ \dot{\mathbf{z}} \end{bmatrix} = \begin{bmatrix} \mathbf{A}\mathbf{x} + \mathbf{B}\mathbf{u} \\ \mathbf{y} - \mathbf{r} \end{bmatrix} = \begin{bmatrix} \mathbf{A} & 0 \\ \mathbf{C} & 0 \end{bmatrix} \begin{bmatrix} \mathbf{x} \\ \mathbf{z} \end{bmatrix} + \begin{bmatrix} \mathbf{B} & 0 \\ 0 & \mathbf{I} \end{bmatrix} \begin{bmatrix} \mathbf{u} \\ \mathbf{r} \end{bmatrix} \tag{3.8}$$

in which $\mathbf{r} = \begin{bmatrix} i_\mathrm{d}^* & i_\mathrm{q}^* \end{bmatrix}^\top$ is the reference in Figure 5 and

$$\mathbf{x} = \begin{bmatrix} i_\mathrm{d} & i_\mathrm{q} & U \end{bmatrix}^\top, \quad \mathbf{u} = \begin{bmatrix} V_\mathrm{td} & V_\mathrm{tq} \end{bmatrix}^\top$$

$$\mathbf{A} = \begin{bmatrix} -\frac{R_k}{L_k} & 0 & 0 \\ 0 & -\frac{R_k}{L_k} & 0 \\ -\frac{V_{\mathrm{sd}k}}{C_k U_{k0}} & 0 & \frac{P_{k0}}{C_k U_{k0}^2} \end{bmatrix}, \quad \mathbf{B} = \begin{bmatrix} \frac{1}{L_k} & 0 \\ 0 & \frac{1}{L_k} \\ 0 & 0 \end{bmatrix}, \quad \mathbf{C} = \begin{bmatrix} \mathbf{I} & 0 \end{bmatrix}$$

are from (3.7). Since inner-loop control is purely local, all terminal indexes are removed from states for simplification, and the coupling term with other terminals is also omitted. Moreover, compared to (3.7), term ω_k is canceled in $\mathbf{A}$ by the cross feedforward paths shown in Figure 5, and AC system voltage V_s is also cancelled in $\mathbf{u}$.

Next introduce control parameters k_P and k_I, so that the PI controllers in Figure 5 are written in form $k_\mathrm{P} + \dfrac{k_\mathrm{I}}{s}$. In the close-loop system, we can then express $\mathbf{u}$ in (3.8) as a linear combination of states and references:

$$\begin{aligned} \mathbf{u} &= -\begin{bmatrix} k_\mathrm{P} & 0 & 0 \\ 0 & k_\mathrm{P} & 0 \end{bmatrix} \mathbf{x} - \begin{bmatrix} k_\mathrm{I} & 0 \\ 0 & k_\mathrm{I} \end{bmatrix} \mathbf{z} + \begin{bmatrix} k_\mathrm{P} & 0 \\ 0 & k_\mathrm{P} \end{bmatrix} \mathbf{r} \\ &= -\begin{bmatrix} k_\mathrm{P}\mathbf{I} & 0 \end{bmatrix} \mathbf{x} - k_\mathrm{I}\mathbf{I}\mathbf{z} + k_\mathrm{P}\mathbf{I}\mathbf{r} \end{aligned} \tag{3.9}$$

Substitute (3.9) into the augmented system (3.8), we can derive the state space expression of close-loop system

$$\dot{\mathbf{x}}_\mathrm{c} = \mathbf{A}_\mathrm{c}\mathbf{x}_\mathrm{c} + \mathbf{B}_\mathrm{c}\mathbf{r}, \tag{3.10}$$

in which $\mathbf{x}_\mathrm{c} = \begin{bmatrix} \mathbf{x} & \mathbf{z} \end{bmatrix}^\top$ is the augmented states, and

$$\mathbf{A}_{\mathrm{c}} = \begin{bmatrix} \mathbf{A} & 0 \\ \mathbf{C} & 0 \end{bmatrix} - \begin{bmatrix} \mathbf{B} \\ 0 \end{bmatrix} \begin{bmatrix} k_{\mathrm{P}}\mathbf{I} & 0 & k_{\mathrm{I}}\mathbf{I} \end{bmatrix}, \quad \mathbf{B}_{\mathrm{c}} = \begin{bmatrix} k_{\mathrm{P}}\mathbf{B} \\ -\mathbf{I} \end{bmatrix}$$

At this point, we get the model of VSC with inner-loop control. While other parameters are from system specification, control gains k_{P} and k_{I} need to be picked. And they can be chosen following a well established method [13, 14]. It is introduced next as part of subsystem modeling. From (3.10), we can derive the close-loop transfer function between i_{d} and i_{q} and their references. Since close-loop dynamics on d and q axes are decoupled and identical, we arbitrarily use i_{d} in the following derivation:

$$\frac{I_{\mathrm{d}}(s)}{I_{\mathrm{d}}^*(s)} = \frac{G(s)}{1+G(s)}$$

in which the loop gain is

$$G(s) = (k_{\mathrm{p}} + \frac{k_{\mathrm{i}}}{s})\frac{1}{Ls+R} = (\frac{k_{\mathrm{p}}}{Ls})\frac{s+k\mathrm{i}/k_{\mathrm{p}}}{s+R/L}.$$

Note in the denominator that the VSC has a pole determined by phase reactor parameters:

$$s = -\frac{R}{L}.$$

Common values of R and L make this pole very close to zero. So a compensator zero is usually used to cancel it out, and thus we have

$$\frac{k_{\mathrm{i}}}{k_{\mathrm{p}}} = \frac{R}{L} \tag{3.11}$$

After the zero pole cancellation, the close-loop transfer function of i_{d} becomes

$$\frac{I_{\mathrm{d}}(s)}{I_{\mathrm{d}}^*(s)} = \frac{1}{(L/k_{\mathrm{p}})s+1},$$

a first order system with time constant

$$\tau_{\mathrm{i}} = L/k_{\mathrm{p}}. \tag{3.12}$$

From (3.11) and (3.12), we can derive the rule by which proportional and integral gains of inner control can be calculated from phase reactor parameters and expected close-loop time constant:

$$k_{\mathrm{P}} = \frac{L}{\tau_{\mathrm{i}}}, \quad k_{\mathrm{I}} = \frac{R}{\tau_{\mathrm{i}}}. \tag{3.13}$$

Time constant τ_{i} is usually selected very small for fast current tracking response. It can be arbitrarily small with the only constraint that the current controller dynamics must be sufficiently slower than switching frequency of power electronics. It is suggested that bandwidth of the close-loop system is smaller than 1/10 of the VSC's switching frequency in rad/s. Typically, τ_{i} ranges from 0.5ms to 5ms for a VSC [14].

Figure 6 shows the step response of an example VSC with R=0.0015p.u., L=0.15p.u. at base value 100kV, 200MVA and 60Hz. A 5ms time constant is used for inner controller. It shows that, under inner-loop control, i_{d} and i_{q} are fully decoupled, and each can track its reference at expected speed.

Now we have fully derived the average model of VSC with inner-loop current control which can be used for subsystem simulation. However, it may not be controllable due to the zero pole cancellation in(3.11). To apply state space design methods to the system, an equivalent minimal realization is also derived to guarantee controllability and observability. Written in form of (3.1), we have:

$$\begin{bmatrix} \dot{i}_{\mathrm{d}k} \\ \dot{i}_{\mathrm{q}k} \\ \dot{U}_k \end{bmatrix} = \begin{bmatrix} -\frac{1}{\tau_{\mathrm{i}k}} & 0 & 0 \\ 0 & -\frac{1}{\tau_{\mathrm{i}k}} & 0 \\ -\frac{V_{\mathrm{sd}k}}{C_k U_{k0}} & 0 & \frac{P_{k0}}{C_k U_{k0}^2} \end{bmatrix} \begin{bmatrix} i_{\mathrm{d}k} \\ i_{\mathrm{q}k} \\ U_k \end{bmatrix} + \begin{bmatrix} \frac{1}{\tau_{\mathrm{i}k}} & 0 \\ 0 & \frac{1}{\tau_{\mathrm{i}k}} \\ 0 & 0 \end{bmatrix} \begin{bmatrix} i^*_{\mathrm{d}k} \\ i^*_{\mathrm{q}k} \end{bmatrix} + \begin{bmatrix} 0 \\ 0 \\ \frac{1}{C_k} \end{bmatrix} I_k. \tag{3.14}$$

3.1.1.2 Real and reactive power control outer-loop Reference value of the inner controller i_{d} and i_{q} is set by the outer controller. The purpose of this outer-loop is to control real and reactive power P and Q being exchanged between VSC and its AC side. Based on (3.5), as long as V_{sd} is relatively well regulated, real power P is determined by i_{d} while reactive power Q is determined by i_{q}. As a result, P and Q can be independently controlled through the decoupled d and q axes.

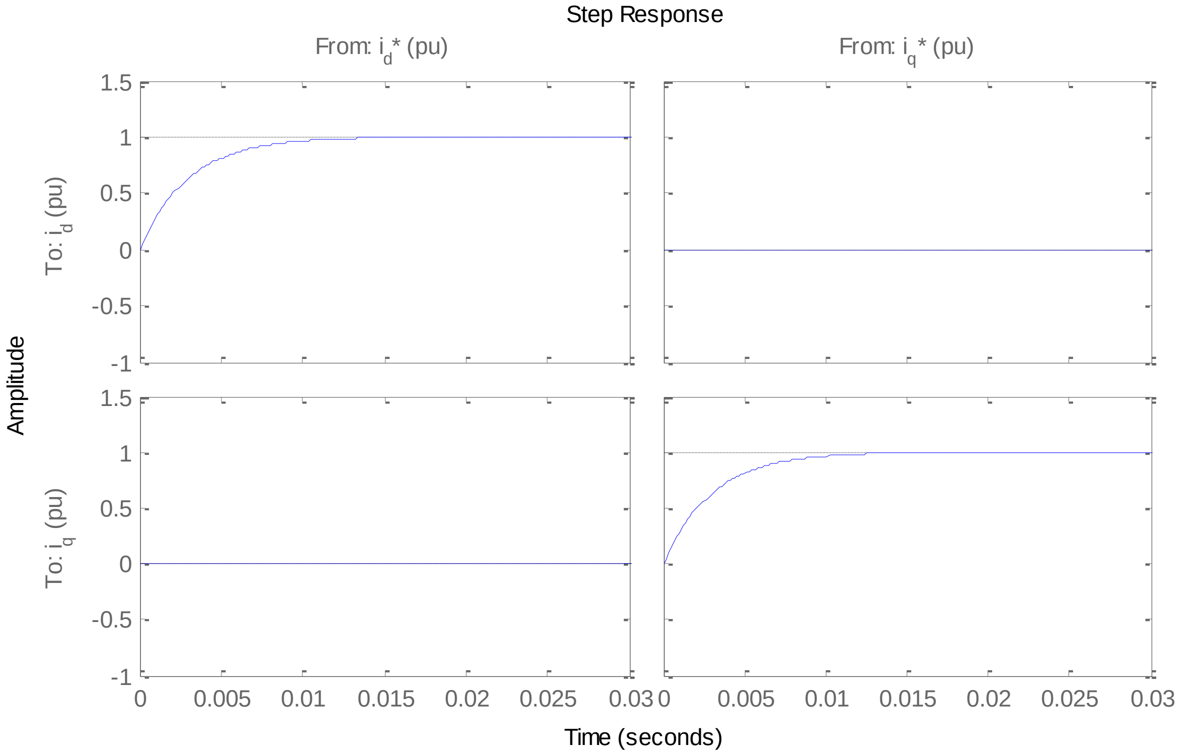

Figure 6: Step response of an example VSC's inner-loop control

Figure 7 shows the diagram of VSC's outer controller. Either real or reactive power control contains two parts: 1) a feedforward branch that directly calculates reference current using (3.5); 2)an optional feedback control loop that eliminates control error in case measurement of V_{sd} is not accurate. The two controllers work in parallel, or only the open-loop control is used for simplicity. In general, dynamics of real and reactive power control is dominated by the faster feedforward control.

$$\begin{aligned} i_{\mathrm{d}}^{*} &= \frac{P^{*}}{V_{\mathrm{sd}}} + (k_{\mathrm{pp}} + \frac{k_{\mathrm{ii}}}{s})(P^{*} - P) \\ i_{\mathrm{q}}^{*} &= -\frac{Q^{*}}{V_{\mathrm{sd}}} - (k_{\mathrm{pp}} + \frac{k_{\mathrm{ii}}}{s})(Q^{*} - Q) \end{aligned} \tag{3.15}$$

(3.15) is the mathematical description of Figure 7. Due to the immediate reaction of feedforward control, PI control parameters k_{pp} and k_{ii} are usually picked small and can be easily tuned as long as no major overshoot is introduced. The two integrators in outer control

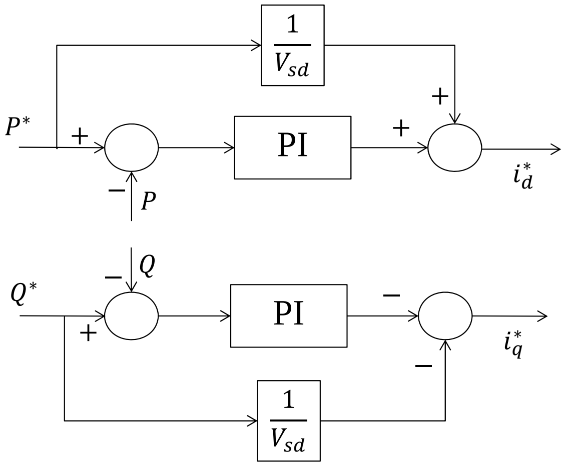

Figure 7: Control diagram of the outer-loop power controller

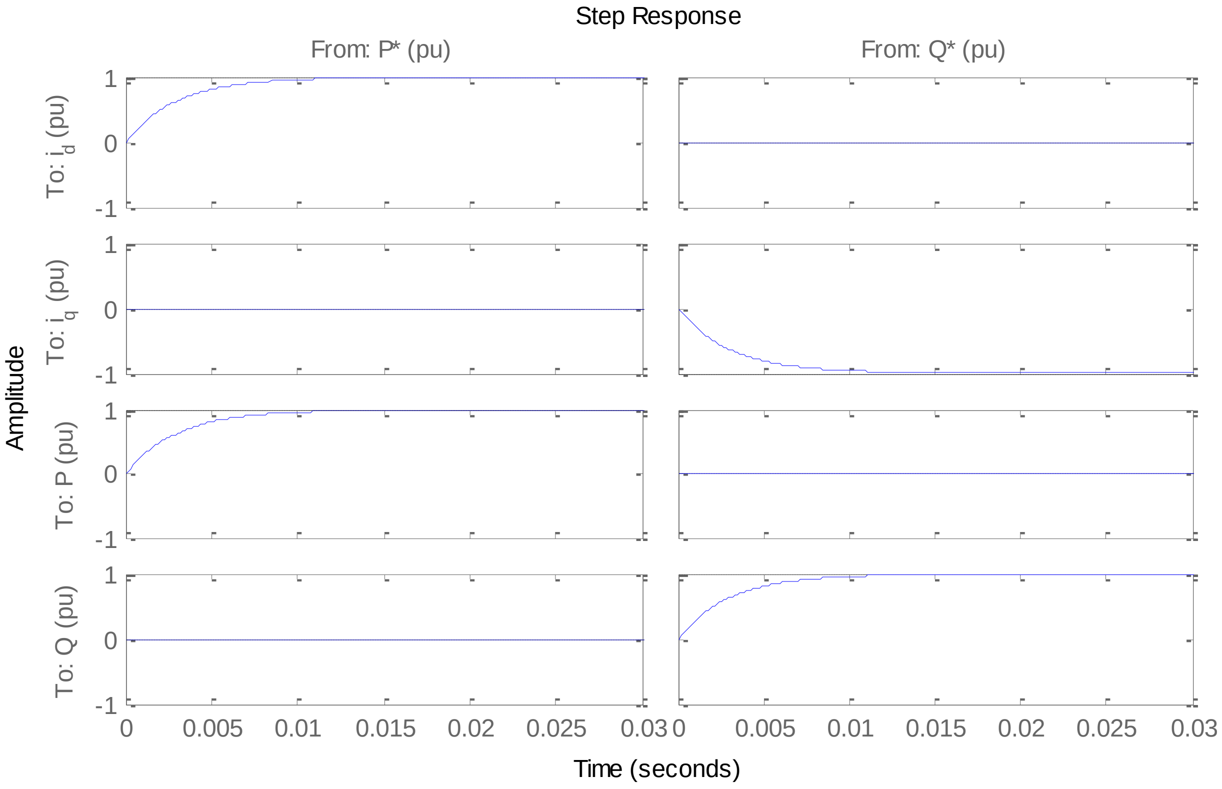

Figure 8: Step response of an example VSC's outer-loop control

also introduce two extra states. The state space expression of the close-loop system can be obtained using the same augmented equation in (3.10). For outer control, plant matrices $\mathbf{A}$ and $\mathbf{B}$ are that of the close-loop inner system, while

$$\mathbf{C} = \begin{bmatrix} V_{\mathrm{sd}} & V_{\mathrm{sq}} & 0 \\ V_{\mathrm{sq}} & -V_{\mathrm{sd}} & 0 \end{bmatrix}$$

is the observation matrix for real and reactive power. For close-loop system of outer control, the new input $\mathbf{u} = \begin{bmatrix} P^* & Q^* \end{bmatrix}^\top$ is the power references. And the feedforward branches can be easily added to input coefficient matrix B_{c} of the close-loop model.

Figure 8 shows the outer-loop response to step change of real and reactive power reference. It is the same example VSC in section 3.1.1.1, with R=0.0015p.u., L=0.15p.u. And a 5ms time constant is selected for the inner controller. It shows that P and Q can be controlled independently by the outer controller. And they each track their references at the same speed of inner controller. This is because of the feedforward control can instantly calculate the input to inner controller.

It is noted that this fast open-loop effect cannot be represented by eigenvalues of close-loop system matrix. To capture this first order dynamics in further system analysis and control design, we also derive an equivalent minimal realization:

$$\begin{bmatrix} \dot{P}_k \\ \dot{Q}_k \\ \dot{U}_k \end{bmatrix} = \begin{bmatrix} -\frac{1}{\tau_{\mathrm{i}k}} & 0 & 0 \\ 0 & -\frac{1}{\tau_{\mathrm{i}k}} & 0 \\ -\frac{V_{\mathrm{sd}k}}{C_k U_{k0}} & 0 & \frac{P_{k0}}{C_k U_{k0}^2} \end{bmatrix} \begin{bmatrix} P_k \\ Q_k \\ U_k \end{bmatrix} + \begin{bmatrix} \frac{1}{\tau_{\mathrm{i}k}} & 0 \\ 0 & \frac{1}{\tau_{\mathrm{i}k}} \\ 0 & 0 \end{bmatrix} \begin{bmatrix} P_k^* \\ Q_k^* \end{bmatrix} + \begin{bmatrix} 0 \\ 0 \\ \frac{1}{C_k} \end{bmatrix} I_k. \tag{3.16}$$

3.1.1.3 AC voltage regulation Reactive power tracking is usually not a direct control goal for a VSC subsystem. When connecting to stiff AC systems, reference Q^* is usually constant zero. However, when it is connected to a weak AC network, of which the AC voltage level is not constant at PCC, the reactive power control on q axis can be used to regulate AC voltage V_{s}.

Figure 9 shows the circuit we use to simulate a weak AC connection. Inductor L_{g} is added between PCC and the ideal voltage source so V_{s} at PCC becomes a variable. And a simple load is added in parallel to VSC to create disturbance on V_{s}.

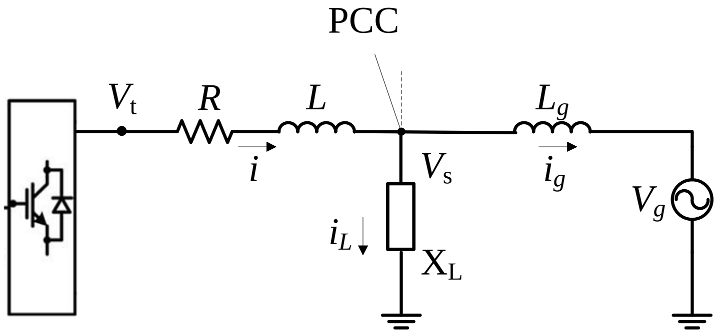

Figure 9: Equivalent circuit of a VSC connected to a weak AC system

The strength, or weakness, of an AC system is measured by short circuit ratios(SCR). It is defined by SCR $= S/P_{\mathrm{d}}$, in which S is PCC's three phase short circuit level in MVA at nominal AC system voltage V_{s0}, and P_{d} is the VSC's rated DC power in MW. An AC system is considered stiff when SCR > 3.0, weak when $2.0 <$ SCR < 3.0, and very weak when SCR < 2.0. From its definition, we can derive that the test circuit's SCR is determined by per unit value of L_{g} (base value V_{s0}, P_{d} and ω_0, where ω_0 is the nominal value of angular velocity at PCC):

$$\mathrm{SCR} = \frac{V_{\mathrm{s0}}^2}{\omega_0 L_{\mathrm{g}} \cdot P_{\mathrm{d}}} = \frac{1}{L_{\mathrm{g}}(\mathrm{p.u.})}.$$

For a weak AC connection, when the PLL remains stable, an extra I controller on the q axis control branch(Figure 10) can regulate AC voltage V_{s} [39, 14]. With the assumption that PLL is stable, (3.3) is still valid. So V_{s} regulation is equivalent to V_{sd} regulation. The compensator shown in Figure 10 is to be in cascade with the reactive power control outer loop. The output of the I controller sets the reference value Q^* for the outer controller.

In this design, the outer and inner controller structure remains the same as for stiff AC system. Even though the inner loop control (Figure 5) treats ω and V_{sd} as constant for decoupling an compensation, these two variables can also be measured in real-time for this purpose. It is also mentioned in [14] that nominal value ω_0 can be used instead to still get good decoupling result. However, this requires good regulation of V_{s}. The close-loop dynamics of V_{sd} need to be significantly slower than the time constant of inner controller.

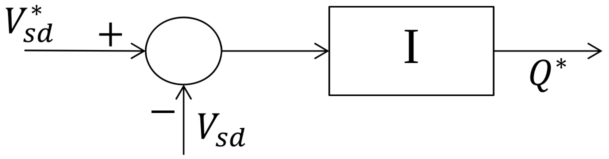

Figure 10: Diagram of AC voltage regulation compensator

The AC voltage regulator in Figure 10 is verified in our test circuit. The same example VSC is used, parameters: R=0.0015p.u.,L=0.15p.u. at base value 100kV, 200MVA and 60Hz. Real and reactive power controller is tuned to have 5ms time constant. For the weak AC circuit, set Lg=0.5p.u. so SCR is 2.0. And the integration gain for V_{sd} control is tuned by Bode plot of the system, shown in Figure 11(a). Considering the characteristics of disturbance on load is often unknown in practice, large phase margin of about 90° is chosen for good robustness. Figure 11(b) plots the simulation result. A set of events is tested in this run:

- At 0.1s a 0.1p.u. step change is placed on V_{sd}^* to show the step response of voltage regulation. It shows slower response than inner controller to reduce its influence on current control.
- At 0.7s a 0.1p.u. step change happens on P^* to show that the real and reactive power control is still decoupled around the operating point.
- At 1s a gradual and then at 1.8s a step load current disturbance are introduced to show AC voltage can be regulated under small disturbance.

It is noted that there are limitations and conditions for this AC voltage control to work well. First it uses PLL, so dynamics of V_{s} cannot exceed the bandwidth of PLL or it becomes unstable. Second its stability is proved around an operating point of V_{s} and P. While V_{s} is supposed to be regulated to a certain value, this condition limits the capability of real power tracking to relatively small bias from the real power operating point. Even though the real and reactive power control is still independent in the inner controller's perspective, fast

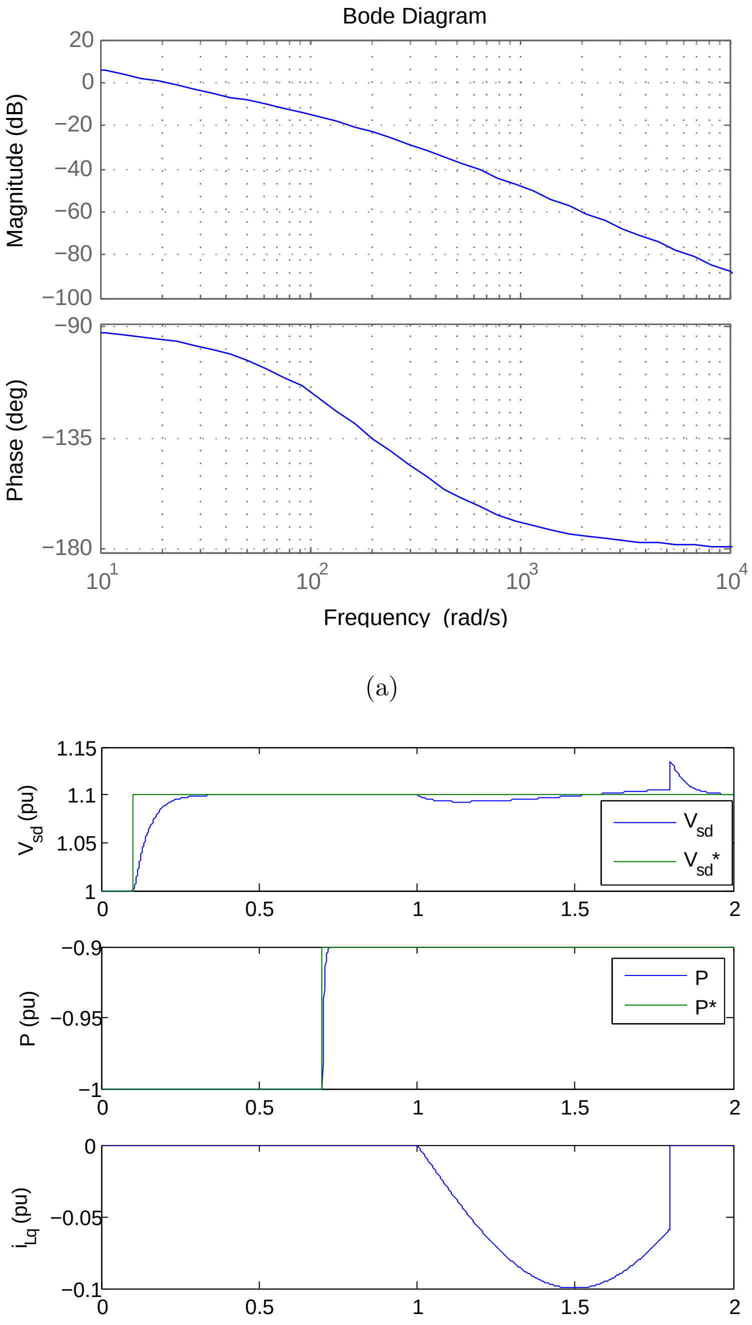

(a)

(b)

Figure 11: AC voltage regulation of example VSC connecting to a weak AC system. (a) Bode plot of the system with AC voltage compensator (b) Simulation result

and large real power change at PCC imposes disturbance on V_s that can cause instability on PLL. As a result, this voltage regulator is most commonly used on STATCOM, a VSC for the sole purpose of AC voltage regulation instead of real power exchange. Stand alone AC voltage regulation equipment like STATCOM is often added to a weak AC connection in addition to the converter to improve stiffness on the AC side. We find this AC voltage control through q axis works well in simulation with proper ramping or saturation of ΔP^* for SCR > 2.0. For very weak AC system, real power transmission level is further limited, VSC connecting to system with SRC $= 1$ can only transmit 0.4p.u. power using traditional controller [40].

When connecting to a very weak AC system whose SCR < 2.0, innovative control of VSC is still an active research topic. The main difficulty is to understand and control PLL's transient under large disturbance of V_s. Durrant et al. [41] derived an average VSC model which includes linearized PLL dynamics. However, due to the high order and nonlinear nature of PLL, such model stands only within very tight operating boundary. In our simulation, we also find it very hard to get good approximation of very weak AC system using just one linear model. Farag et al. [42] uses a similar linearization method but obtained multiple linear models around 52 operating points. An LMI method is then used to design a robust controller for these operating points. Such method requires intensive modeling effort on a single subsystem, thus can be very challenging to generalize for multi-terminal system. Besides the effort on detailed PLL modeling and control, another recent trend is to find alternatives to PLL [35, 43, 40, 44]. In [40] a model predictive control approach is introduced by Beccuti et al. to achieve real power control, AC voltage regulation and dq frame synchronization through one MIMO controller. While in [35, 43], Zhang et al. proposed to directly control the phase and magnitude of V_s so that dq frame alignment is not needed. Under this control, the VSC shows similar dynamics as a synchronous machine and enables 0.86p.u. power transmission from a system with SCR $= 1.2$ in simulation. This controller is verified in [44] through simulation to integrate offshore wind generation by a VSC-HVDC link to a weak AC.

Since these new control concepts are still evolving and to be verified in industrial implementation. Only the traditional control method in Figure 10 is modeled in this work.

AC voltage regulation is considered a local control goal and is not coupled to real power control because detailed transient of PLL is not modeled. Instead, limitation on real power operating point and magnitude of ΔP^* is considered as extra control requirements on the subsystem containing a weak AC. Moreover, ramping of P^*, if wanted, can be equivalently modeled by a larger time constant on the real power control.

3.1.1.4 DC voltage regulation Voltage regulation on DC side plays an important role in a VSC based DC system. One can see on the DC side of Figure 4 that voltage U_k indicates the charging of large capacitor C_k. When U_k increase, C_k is charging, implying that the DC grid is accumulating power. On the other hand, when U_k decrease, C_k is discharging, implying that the DC grid is loosing power. In other word, DC voltage is the indicator of power balance in a DC network, comparable to frequency in an AC grid. And thus the DC voltage regulation is thus as critical as primary control in AC system.

Since only real power is exchanged between AC and DC side of a VSC, DC voltage can be controlled through P control branch on d axis. This means that the two important control goals: real power tracking and DC voltage regulation, are controlled through the same input V_{td}^* of VSC. So some mechanism is needed to select or weigh between the two.

In a two terminal DC system, such as traditional HVDC or MVDC connection, power control and voltage regulation can be simply divided onto rectifier and inverter. Since the system is to transmit desired amount of power stably through a single DC link, it is common to have one terminal working in power tracking mode and the other in DC voltage regulation mode. In DC voltage regulation mode, outer controller on d axis is replaced by a PI feedback control of U_k, which is shown in Figure 12(a). This controller directly set reference for inner i_{d} controller. And a negative sign is added to control error because our defined positive direction of i_{d} and P is discharging the DC side.

In an MTDC system, control strategies for power balancing is still an active research topic:

- One earlier control scheme is the slack converter method, which is directly generalized from two terminal technology. Using this method, we have $N-1$ converters out of a N-terminal system working fully in real power tracking mode, and set the rest one VSC

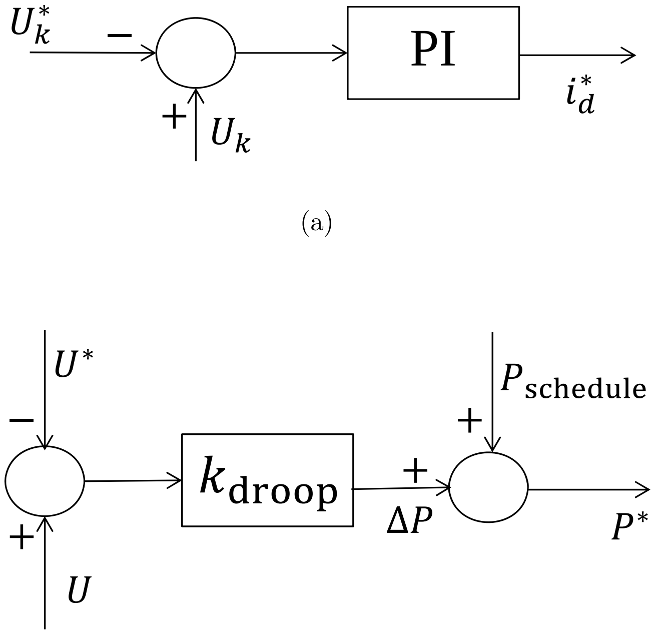

(a)

(b)

Figure 12: Two control schemes of DC voltage regulation: (a) DC voltage PI control in d axis outer loop (b) DC voltage droop control

to be the “slack” that works solely on DC voltage regulation. The control of the slack converter is the same as that in traditional HVDC system (Figure 12(a)). This is the basic power balancing scheme commonly adopted in MTDC researches [6, 45, 16, 46]. It is very simple but with obvious disadvantages. First the voltage regulation VSC takes all power disturbance in the system, which can impose great stress to its AC side frequency and voltage stability. Second, no power transmission can be scheduled for this voltage regulation VSC. Last but not least, there is no redundancy for DC voltage regulation in the system in case of fault or failure on the slack converter.

- To share the task of power balancing among multiple terminals, a voltage droop control method has been proposed in several papers[18, 17]. This control structure is adopted from primary control of AC frequency regulation. Figure 12(b) shows one implementation of such droop controller. The droop gain k_{droop} is basically a P controller which take the DC voltage error and generate a small adjustment ΔP on scheduled power reference P_{schedule}. The two are combined as real power reference P^* for the outer controller. The reason for using only a P controller is to allow some control error. Due to their tightly coupled DC sides, such control error can avoid conflict among terminals. This allows the controller in Figure 12(b) to be deployed on multiple VSCs in an MTDC system.

DC side dynamics is determined by the overall MTDC system, so we consider DC voltage regulation as a global control goal. The control design and performance will be studied after deriving the full model of MTDC.

3.2 MODEL OF DC CABLE NETWORK

In the second stage, models of subsystems are assembled into one system level model. At this stage, we first use circuits laws to derive state space model of the DC cable network. This introduces a new set of state variables $\mathbf{x}_{\text{c}}$, which represents the couplings among subsystems. An example of this type of state variables is the current on DC cables. Based on the coupling model, $\mathbf{u}_{\text{c}k}$ from stage one can now be expressed as a set of functions of $\mathbf{x}_c$:

$$\mathbf{u}_{\text{c}k} = F(\mathbf{x}_{\text{c}}).$$

Then we can connect the subsystems by substituting these equations to (3.1).

In this paper, π-circuit is used to model DC connection between two nodes in the network. The capacitors in the π-circuits combines both cable capacitor and VSC's DC side capacitor, while value of the later is dominant. Equivalent circuit of the DC cable network is shown on the DC side of Figure 4. without loss of generality, we define all current flows from nodes with lower index to nodes with higher index. If the actual current is in the opposite direction, its value will be negative in our model. For the DC circuit network, current through inductor and voltage across capacitor are the natural choice of state variables. As dynamics of U_k is already modeled in subsystem level, we only introduce new states:

$$\mathbf{x}_{\text{c}} = \begin{bmatrix} \cdots & i_{jk} & \cdots \end{bmatrix}^\top .$$

Each DC connection will introduce one state variable. So the length of vector $\mathbf{x}_{\mathrm{c}}$ equals to the total number of DC branches, n_{branch}, in the network. We then derive the dynamics of all I_{jk}, and use them to re-express the coupling input I_k in the subsystem model:

$$\begin{aligned} \frac{dI_{jk}}{dt} &= -\frac{R_{jk}}{L_{jk}} I_{jk} + \frac{1}{L_{jk}} (U_j - U_k) \\ I_k &= \sum_{j=1}^{k-1} I_{jk} - \sum_{j=k+1}^{n_{\text{branch}}} I_{kj} \end{aligned} \tag{3.17}$$

For a general network topology, it is possible to have intermediate nodes that are in the joint of multiple DC cables but not in connect to a VSC. However such topology is rarely used in existing MTDC design and studies. So such intermediate nodes are not considered in our model for simplification of expression.

State space representation of a N-terminal DC system can be assembled by stacking up local states $\mathbf{x}_k$ from index 1 to N, then arranging coupling states $\mathbf{x}_{\mathrm{c}}$ at the end of the state vector. The resulting linear model would take the form:

$$\begin{aligned} \begin{bmatrix} \dot{\mathbf{x}}_1 \\ \dot{\mathbf{x}}_2 \\ \vdots \\ \dot{\mathbf{x}}_N \\ \dot{\mathbf{x}}_c \end{bmatrix} &= \begin{bmatrix} \mathbf{A}_{11} & 0 & \cdots & 0 & \mathbf{A}_{1\mathrm{c}} \\ 0 & \mathbf{A}_{22} & \cdots & 0 & \mathbf{A}_{2\mathrm{c}} \\ \vdots & \vdots & \ddots & \vdots & \vdots \\ 0 & 0 & \cdots & \mathbf{A}_{NN} & \mathbf{A}_{N\mathrm{c}} \\ \mathbf{A}_{\mathrm{c}1} & \mathbf{A}_{\mathrm{c}2} & \cdots & \mathbf{A}_{\mathrm{c}N} & \mathbf{A}_{\mathrm{cc}} \end{bmatrix} \begin{bmatrix} \mathbf{x}_1 \\ \mathbf{x}_2 \\ \vdots \\ \mathbf{x}_N \\ \mathbf{x}_{\mathrm{c}} \end{bmatrix} \\ &+ \begin{bmatrix} \mathbf{B}_1 & 0 & \cdots & 0 \\ 0 & \mathbf{B}_2 & \cdots & 0 \\ \vdots & \vdots & \ddots & \vdots \\ 0 & 0 & \cdots & B_N \\ 0 & 0 & \cdots & 0 \end{bmatrix} \begin{bmatrix} \mathbf{u}_1 \\ \mathbf{u}_2 \\ \vdots \\ \mathbf{u}_N \end{bmatrix} . \end{aligned} \tag{3.18}$$

In (3.18), system matrix is mostly block diagonal with sparse coupling elements on the side. Subsystem matrix $\mathbf{A}_{ii}$ can be of different dimension depending on type of AC system and level of modeling detail of terminal i. Input matrix is also a block matrix because all control inputs are local and cannot directly effect states of other terminals. The all zero rows at the bottom have the same number of rows as $\mathbf{x}_c$'s dimension. This indicates that no input can directly affect coupling states in DC network.

The two-stage model generation method is implemented in a MATLAB script and can be applied to arbitrary MTDC setup. Moreover, the resulting state space model can be easily adjusted or reconfigured. When there is a change in subsystem i, we can simply change $\mathbf{A}_{ii}$ and B_i. Even dimension change in $\mathbf{A}_{ii}$ can be easily handled with adding or removing all zero rows in $\mathbf{A}_{ic}$ and columns in $\mathbf{A}_{ci}$. Similarly when change is wanted on DC network, either parameter or topology, it can be implemented by adjusting a few coupling elements on the side of system matrix without disturbing the subsystem models. This enables researchers to conveniently explorer different system setups and make adjustment on their MTDC design.

3.3 OPERATING POINT

For an N-terminal MTDC system, (3.18) is a linear small signal model around operating point

$$\begin{bmatrix} P_{10} & \cdots & P_{N0} & U_{10} & \cdots & U_{N0} \end{bmatrix}^\top,$$

in which P_{k0} and U_{k0} are the steady state power and DC voltage at terminal k, $k = 1 \cdots N$. While P_{k0}'s are usually specified by grid operator during scheduling, most U_{k0}'s are to be determined. This is a special property of DC power grid comparing to an AC grid. While there is only one nominal frequency in an AC network, power flow in DC grid is driven by voltage difference between two nodes. Thus the steady state DC voltage is different from one terminal to another. Interestingly, voltage in DC grid is not only indicator of power balance but also key factor for power flow control. In other word, it plays both roles of frequency and phase in an AC system. In this section, we introduce the method being used to solve the operating point.

In steady state, P_{k0}'s and U_{k0}'s should obey the following circuit law:

$$\begin{aligned} \mathbf{I}_{\mathrm{DC}} &= -\mathbf{Y}\mathbf{U}_{\mathrm{DC}} \\ P_k &= U_k I_k \end{aligned} \tag{3.19}$$

in which $\mathbf{Y}$ is the admittance matrix of the DC network, $\mathbf{I}_{\mathrm{DC}} = \begin{bmatrix} \cdots & I_k & \cdots \end{bmatrix}^\top$, and $\mathbf{U}_{\mathrm{DC}} = \begin{bmatrix} \cdots & U_k & \cdots \end{bmatrix}^\top$. Remind that definition of I_k, U_k and P_k can all be find in Figure 4.

Matrix $\mathbf{Y}$ can be constructed based on (3.17). In steady state, we can derive

$$\begin{aligned} I_k &= \sum_{j=1}^{k-1} \frac{U_j - U_k}{R_{jk}} - \sum_{j=k+1}^{N} \frac{U_k - U_j}{R_{kj}} \\ &= \begin{bmatrix} R_{1k}^{-1} & \cdots & R_{k-1,k}^{-1} & -\sum_{j=1}^{N} R_{jk}^{-1} & R_{k,k+1}^{-1} & \cdots & R_{k,N}^{-1} \end{bmatrix} \mathbf{U}_{DC} \end{aligned} \tag{3.20}$$

In (3.20), $R_{jk} = R_{kj}$ because connection between any two terminals is single and bidirectional. If connection does not exist between terminal j and k, $R_{jk} = \infty$. Finally, $R_{kk} = 0$ as connection is not defined from a terminal to itself. From (3.20), we have the kth row of matrix $\mathbf{Y}$ as

$$\mathbf{Y}_k = -\begin{bmatrix} R_{1k}^{-1} & \cdots & R_{k-1,k}^{-1} & -\sum_{j=1}^{N} R_{jk}^{-1} & R_{k,k+1}^{-1} & \cdots & R_{k,N}^{-1} \end{bmatrix}$$

Cancelling $\mathbf{I}_{\mathrm{DC}}$ from (3.19), we get a set of N equations between P_{k0}'s and U_{k0}'s:

$$\mathbf{Y}\mathbf{U}_{\mathrm{DC}} + \begin{bmatrix} \vdots \\ P_k U_k^{-1} \\ \vdots \end{bmatrix} = 0 \tag{3.21}$$

For an N-terminal, it is common to specify operating power for $N-1$ terminals and select DC voltage level for the rest one terminal. Without loss of generality and for the purpose of notation simplification, set terminal N to be the one with known U_{N0}. So the goal is to solve $\mathbf{U}_x = \begin{bmatrix} \cdots & U_{k0} & \cdots \end{bmatrix}^\top$, $k = 1, \cdots, N-1$ and P_{N0}.

Partition matrix $\mathbf{Y}$ from the last row and column:

$$\mathbf{Y} = \begin{bmatrix} \mathbf{Y}_{11} & \mathbf{y}_{12} \\ \mathbf{y}_{21} & y_{22} \end{bmatrix} \tag{3.22}$$

We can rewrite (3.21) in two parts:

$$\begin{aligned}
&\mathbf{Y}_{11}\mathbf{U}_x + \mathbf{y}_{12}U_{N0} + \begin{bmatrix} \vdots \\ P_{k0}U_{k0}^{-1} \\ \vdots \end{bmatrix} = 0 \quad k = 1, \cdots, N-1 \\
&\mathbf{y}_{21}\mathbf{U}_x + y_{22}U_{N0} + U_{N0}^{-1}P_N = 0
\end{aligned} \tag{3.23}$$

The first part contains $N-1$ nonlinear equations of unknown vector $\mathbf{U}_x$. It can be solved by Newton method. Substitute the solved $\mathbf{U}_x$ back into (3.23), we can directly get the last unknown P_N in the second part.

To solve the first part, define

$$\mathbf{f}(\mathbf{U}_x) = \mathbf{Y}_{11}\mathbf{U}_x + \mathbf{y}_{12}U_{N0} + \begin{bmatrix} \vdots \\ P_{k0}U_{k0}^{-1} \\ \vdots \end{bmatrix}.$$

We get its Jacobian matrix:

$$\mathbf{J_f}(\mathbf{U}_x) = \mathbf{Y}_{11} - \mathrm{diag}(P_{10} \quad \cdots \quad P_{N-1,0}) \begin{bmatrix} U_{10}^{-2} \\ \vdots \\ U_{N-1,0}^{-2} \end{bmatrix}.$$

Initial all elements of $\mathbf{U}_x$ with U_{N0}, the solution can then be numerically searched by the following iterative process:

- Solve $\mathbf{J_f}(\mathbf{U}_x^{(i)})\Delta\mathbf{U}_x = -\mathbf{f}(\mathbf{U}_x^{(i)})$ for $\Delta\mathbf{U}_x$.
- Let $\mathbf{U}_x^{(i+1)} = \mathbf{U}_x^{(i)} + \Delta\mathbf{U}_x$

Since the given U_{N0} provides good initial guess to all terminals' DC voltages. The Newton algorithm can converge very fast within a few iterations. Solving (3.23) is equivalent to a DC analysis on a circuit of $N-1$ power source and one voltage source. Since power source is not available in most circuit simulators, this routine of Newton algorithm becomes quite helpful to MTDC model generation.

3.4 SUMMARY

In this chapter, a systematic method is proposed to obtain small signal state space model of MTDC systems. It is a two-stage procedure that provides proper isolation between modeling at subsystem level and network level, so that it can be applied to arbitrary system configuration with different network topologies and various AC-side components.

In Section 3.1, models of a VSC subsystem is derived. A subsystem contains a VSC and its AC side components, so all local dynamics and control goals can be addressed. Detailed literature review is conducted on multiple VSC applications at subsystem level. Average circuit simplification and the basic double loop control structure of VSC are described and modeled. Extensions for different AC and DC side control applications is also presented. Correctness of these subsystem models are verified in simulation.

In Section 3.2, the DC network model is derived. The model assembling procedure is then introduced and the overall system model is presented.

In Section 3.3, dimension of operating point and its degree of freedom is discussed. Steady state equations are derived from circuit laws that the operating point must obey. Due to the nonlinearity of the set of equations, an numerical routine based on Newton method is proposed to solve the operating point.

4.0 LMI-BASED CONTROL DESIGN

Obtaining the state space model opens up the door to many control design techniques in modern control theory. But due to the distributed nature of MTDC system, information constraints must be imposed to get feasible controllers. We decide that LMI-based design method is the proper tool for this problem. In this section, we will introduce how different control structures are modeled. It is also explained why and how the control design is formulated as a LMI optimization problem, which can be efficiently solved in Matlab [47, 48].

4.1 RECONFIGURABLE STATE-FEEDBACK CONTROL FOR MTDC SYSTEM

To have a reconfigurable controller model, we consider the most commonly used control law: constant-gain, full-state feedback control.

$$\mathbf{u} = \mathbf{K}\mathbf{x} \tag{4.1}$$

The system under control is now described by

$$\dot{\mathbf{x}} = (\mathbf{A} + \mathbf{B}\mathbf{K})\mathbf{x} \tag{4.2}$$

Different controller structures can be indicated by different nonzero patterns of the control gain matrix **K**. Figure 13 illustrates some possible control schemes in form of **K**'s nonzero pattern. The white regions in **K** are all zeros, while the shaded regions can have nonzero elements.

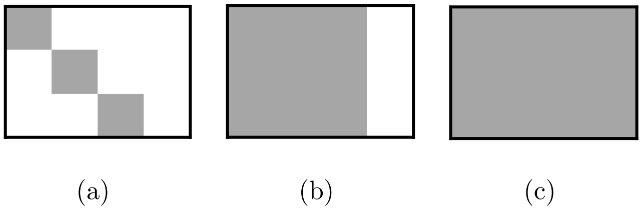
(a) (b) (c)

Figure 13: Use $\mathbf{K}$'s nonzero patterns to represent different controller structures

Figure 13(a) represents a set of distributed controllers. Each nonzero block of $\mathbf{K}$ can be seen as a local controller, because when applying control law (4.1), local control outputs $\mathbf{u}_k$ is obtained merely through linear combination of local states $\mathbf{x}_k$. Note that the all-zero columns in $\mathbf{K}$ means that coupling states on DC cables are not used by controllers, considering the scenario where sensor is not available on cables or communication is not fast enough to feedback these data in real time. The basic droop control of DC voltage falls into this category, as a special case with only one nonzero element (droop gain) in the local control gain matrix. If a subsystem does not participate in droop control, for example a CPL or a wind generator in MPPT mode, the columns in $\mathbf{K}$ corresponding to its local states will be all zeros, like for the coupling states.

Similarly, Figure 13(b) describes the control scheme when communication between terminals is available. In this case, controller can determine local control output based on states of multiple subsystems. Control methods with global observation [20, 19] can be modeled with such $\mathbf{K}$.

Last but not least, Figure 13(c) is a full-state feedback control structure, which further requires sensors or estimator for the coupling states. The physical meaning of the later two nonzero patterns can be two-fold: enabling cooperative behavior among distributed controllers through communication, or serving as a slower higher level centralized controller for the purpose of secondary control and power flow management.

To summarise, specification on matrix $\mathbf{K}$'s nonzero pattern constrains the information structure of our distributed MIMO system, so we can easily configure the control architecture based on what's available in the real system. Furthermore, it provides an efficient way to study the trade-off between performance and communication cost, as various communication topologies can be easily modeled in an unified method.

4.2 LMI-BASED CONTROL DESIGN

To design control for the MTDC system, we need to find feedback gain matrix $\mathbf{K}$ that: (1) can stabilize the system; (2) has practical control gains; (3) matches with specified nonzero pattern. Because of the third requirement, popular design techniques based on full-state feedback, such as LQR, cannot be directly applied. In this paper, we choose a LMI-based method that can numerically search for the desired $\mathbf{K}$.

Starting with the first requirement, to ensure the global asymptotic stability of the closed-loop system (4.2), we need to search for a control gain $\mathbf{K}$ and Lyapunov function

$$V(\mathbf{x}) = \mathbf{x}^\top \mathbf{P}\mathbf{x} \tag{4.3}$$

with matrix $\mathbf{P}$ being symmetric so that $\mathbf{P} > 0$ (positive definite) and

$$(\mathbf{A} + \mathbf{B}\mathbf{K})^\top \mathbf{P} + \mathbf{P}(\mathbf{A} + \mathbf{B}\mathbf{K}) < 0. \tag{4.4}$$

Note that (4.4) is not linear in the unknown $\mathbf{P}$ and $\mathbf{K}$, so it is generally difficult to solve this matrix inequality. To avoid such difficulty, we follow a procedure proposed in [25] and introduce new matrices:

$$\mathbf{Y} = \tau \mathbf{P}^{-1}\,(\tau > 0) \text{ and } \mathbf{L} = \mathbf{K}\mathbf{Y}$$

with which we can rewrite $\mathbf{P} > 0$ and (4.4) as

$$\mathbf{Y} > 0 \text{ and } \mathbf{Y}\mathbf{A}^\top + \mathbf{A}\mathbf{Y} + \mathbf{L}^\top \mathbf{B}^\top + \mathbf{B}\mathbf{L} < 0.$$

Any feasible $\mathbf{Y}$ and $\mathbf{L}$ subject to the above inequalities can produce a control gain matrix

$$\mathbf{K} = \mathbf{L}\mathbf{Y}^{-\mathbf{1}}$$

which ensures global asymptotic stability of system (4.2).

In order to prevent control gains from becoming unacceptably large, we need to add conditions to bound the norm of $\mathbf{K}$. We include the following inequalities about $\mathbf{L}$ and $\mathbf{Y}$ to bound $\|\mathbf{K}\|_2$ implicitly:

$$\begin{bmatrix} -\kappa_{\mathrm{L}}\mathbf{I} & \mathbf{L}^\top \\ \mathbf{L} & -\mathbf{I} \end{bmatrix} < 0 \text{ and } \begin{bmatrix} \mathbf{Y} & \mathbf{I} \\ \mathbf{I} & \kappa_{\mathrm{Y}}\mathbf{I} \end{bmatrix} > 0 \tag{4.5}$$

where κ_{L} and κ_{Y} represent scalar variables, while $\mathbf{I}$ refers to identity matrix. Using the Schur complement formula [49], it can be seen that (4.5) is equivalent to the constraints $\|\mathbf{L}\|_2 < \sqrt{\kappa_{\mathrm{L}}}$ and $\|\mathbf{Y}^{-1}\|_2 < \kappa_{\mathrm{Y}}$, which imply $\|\mathbf{K}\|_2 \leq \|\mathbf{L}\|_2\|\mathbf{Y}^{-1}\|_2 < \sqrt{\kappa_{\mathrm{L}}}\kappa_{\mathrm{Y}}$.

Furthermore, to satisfy an arbitrary nonzero pattern of $\mathbf{K}$, we can require that matrix $\mathbf{L}$ has the identical nonzero pattern as that of matrix $\mathbf{K}$ and matrix $\mathbf{Y}$ has a diagonal form [50].

Finally, to improve robustness of the close-loop system, an extra term $\alpha^2\mathbf{x}^\top\mathbf{H}^\top\mathbf{H}\mathbf{x}$ is introduced to measure the level of uncertainty system (4.2) can tolerate.Note that $\mathbf{H}$ is a constant square matrix, and α is a scalar parameter. For a given $\mathbf{H}$, the larger α is, the more robust the system will be.

Taking into account the bound of $\|\mathbf{K}\|_2$ and the robustness measurement, the original stabilization problem (4.4) is converted to the following LMI optimization problem in variables γ, κ_{Y}, κ_{L}, Y, and L:

$$\text{Minimize } a_1\gamma + a_2\kappa_{\mathrm{Y}} + a_3\kappa_{\mathrm{L}}, \text{ subject to}$$

$$\begin{gathered} \begin{bmatrix} \mathbf{YA}^\top + \mathbf{AY} + \mathbf{L}^\top\mathbf{B}^\top + \mathbf{BL} & \mathbf{I} & \mathbf{YH}^\top \\ \mathbf{I} & -\mathbf{I} & 0 \\ \mathbf{HY} & 0 & -\gamma\mathbf{I} \end{bmatrix} < 0 \\ \mathbf{Y} > 0, \ \begin{bmatrix} -\kappa_{\mathrm{L}}\mathbf{I} & \mathbf{L}^\top \\ \mathbf{L} & -\mathbf{I} \end{bmatrix} < 0, \text{ and } \begin{bmatrix} \mathbf{Y} & \mathbf{I} \\ \mathbf{I} & \kappa_{\mathrm{Y}}\mathbf{I} \end{bmatrix} > 0 \end{gathered} \tag{4.6}$$

in which γ is defined by $\gamma = 1/\alpha^2$, so that minimizing γ is equivalent to maximizing the margin α. As one can see, the cost function contains one term γ for improving performance and two terms κ_{Y} and κ_{L} for reducing control effort. They are weighted by positive coefficients a_1, a_2 and a_3. In addition to the three weights, $\mathbf{H}$ is another important set of parameters that can greatly influence the close-loop system response. Not only does it set the tolerance of uncertainty for each state, it can be used to differentiate relative importance among the states. If certain state needs more effort to be stabilized or reach to desired response speed, we can increase its corresponding elements in $\mathbf{H}$. Placement of close-loop eigenvalues can also be adjusted through $\mathbf{H}$, by studying participation factor of states. Guidelines for choosing $\mathbf{H}$ will be further demonstrated in Section 5.1.

The LMI-based design method provides a numerical alternative for finding control gain matrix $\mathbf{K}$ under information constraints, which cannot be solved by standard LQR. However, arbitrary nonzero pattern is achieved at the cost of a reduced solution space. Recall that matrix $\mathbf{Y} = \tau\mathbf{P}^{-1}$ is forced into diagonal form, which greatly limits the choice of Lyapunov function (4.3). One can often relax $\mathbf{Y}$ to be in block-diagonal form, when specified nonzero pattern can be preserved after multiplied by inverse of such $\mathbf{Y}$. Most block-wise nonzero pattern, for instance in Figure 13(a) and Figure 13(b), satisfies this condition. In this case, we can still specify communication topology among subsystems but not the controller structure inside. The later is in general insignificant, because the resulting control effort within a nonzero block will concentrate only on a few critical gains, which are usually consistent with manually-designed controllers. We will show in Section 5 that the proposed method can be used for droop gain selection, with $\mathbf{K}$ specified in structure of Figure 13(a).

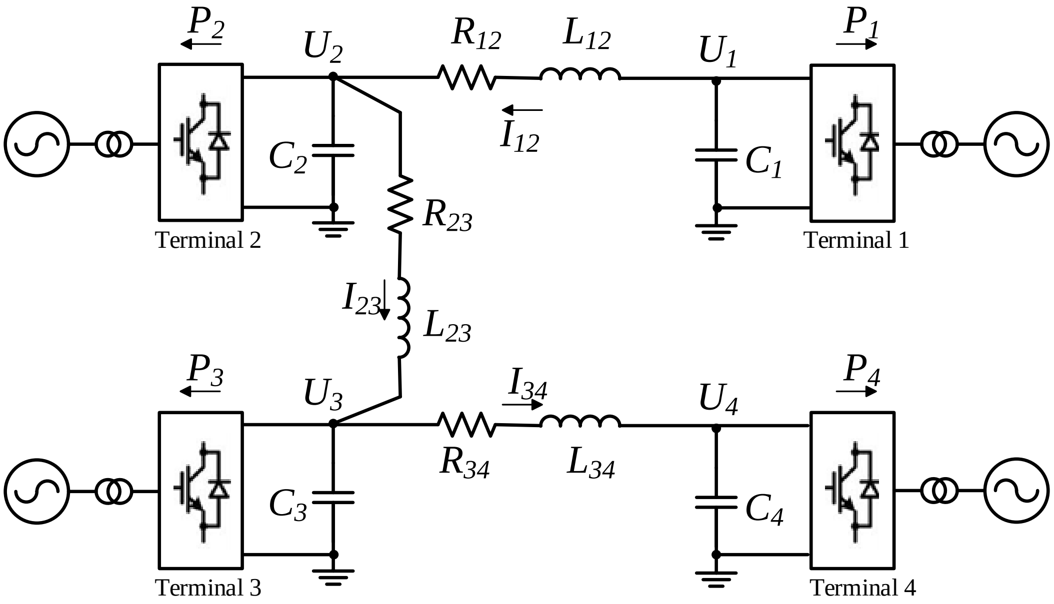

Figure 14: Study case of a four-terminal system.

5.0 CASE STUDY OF A FOUR-TERMINAL SYSTEM INTERCONNECTING AC AREAS

In this chapter, a four-terminal HVDC system presented by Prieto-Araujo et al. [18] is used to demonstrate the proposed method. Compare to the study in [18], which treats all VSCs as ideal sources in the DC network, we consider a more detailed model that includes local dynamics of VSC subsystems. The test case was originally for off-shore wind power integration. However in this chapter, we start with a simpler application of four interconnected AC grids. And the full test case will be studied in Chapter 6.

As shown in Figure 14, the terminals each ties to an AC grid, and they are interconnected through HVDC backbone. The system parameters and operating points are shown in Table 1. All per unit values are based on nominal value of 100MW, 150kV and 50Hz. The power operating points indicate that terminal 1 and 4 are exporting power from the DC system, while terminal 2 and 3 are injecting power. The DC voltage operating points are solved by the numerical routine described in Section 3.3. For the AC components, real and reactive power exchange with converters are controlled locally by controller described in Section 3.1.1.2. The local close-loop dynamic can be determined by time constants τ_{dk} and τ_{qk}, due to the zero-pole cancellation caused by local current controller.

Table 1: Table of parameters

DC grid parameters			
Parameter	Value (p.u.)	Parameter	Value (p.u.)
R_{12}	0.0022	L_{12}	0.0070
R_{23}	0.0011	L_{23}	0.0035
R_{34}	0.0018	L_{34}	0.0056
C_k, $k = 1, \ldots, 4$	11		
Operating point			
Parameter	Value (p.u.)	Parameter	Value (p.u.)
P_{10}	0.6000	U_{10}	0.9659
P_{20}	-0.5000	U_{20}	0.9673
P_{30}	-0.5000	U_{30}	0.9674
P_{40}	0.3988	U_{40}	0.9667
AC current control close-loop parameters			
Parameter	Value	Parameter	Value
τ_{dk}, $k = 1, \ldots, 4$	1 ms	τ_{qk}, $k = 1, \ldots, 4$	1ms

Eigenvalue and participation factor of the open-loop MTDC system are studied to understand its dynamic response. Here, the open-loop system is defined as the MTDC grid without DC voltage regulation. Its input, $\begin{bmatrix} \cdots & P_k^* & \cdots \end{bmatrix}^\top$, are reference values of real power, which are controlled locally at the converters. Figure 15 shows eigenvalues of the system's minimal realization, which has 15 states. For each real or complex conjugate pair of eigenvalues, their related states are listed in the attached text boxes. Note that in this paper, all eigenvalues are plotted in per-unitized scale, so real and imaginary axises are scaled by $2\pi f_0$, in which f_0 is the nominal frequency. There are 8 overlapping real eigenvalues on the left of Figure 15. These fast first-order modes each independently represents a local close-loop control on d or q axis of the four converters. The rest eigenvalues, one real and three complex conjugate pairs, are related to the open-loop dynamic of the DC grid. Among them, the marginally stable pole on origin is participated equally by the four DC voltages on terminals. On the other hand, the complex eigenvalues, of which each conjugate pair corresponds to an oscillation mode, get various participation among DC-side states. So in Figure 15, these participating states are listed in descending order of absolute participation factor. Based on this modal analysis, we need to stabilize and properly damp the DC related modes, in order to regulate the MTDC system. The participation factor will also be useful for the fine tuning of our control design algorithm.

In the following sections, we use the proposed LMI-based method to design control for the four-terminal study case. Different control structures are considered for the control goal of DC voltage regulation.

5.1 DISTRIBUTED VOLTAGE REGULATION

We first consider a distributed control scenario, where nonzero pattern of $\mathbf{K}$ is in the form of Figure 13(a). In this case, all terminals are participating the DC voltage regulation but only use feedback of local measurements.

To solve problem (4.6) we use YALMIP, a toolbox for specifying and solving optimization problems [48]. Nonzero pattern of matrix $\mathbf{L}$ and $\mathbf{Y}$ can be specified by defining only their nonzero entries as optimization variables. For choice of parameters, we start with $a_1 = a_2 = a_3 = 1$ and $\mathbf{H} = \mathbf{I}$. Note that matrix $\mathbf{H}$ has the same dimension as the system matrix. Here, we limit it to diagonal form $\mathrm{diag}(\dots, h_i i, \dots)$ to reduce number of parameters. Because

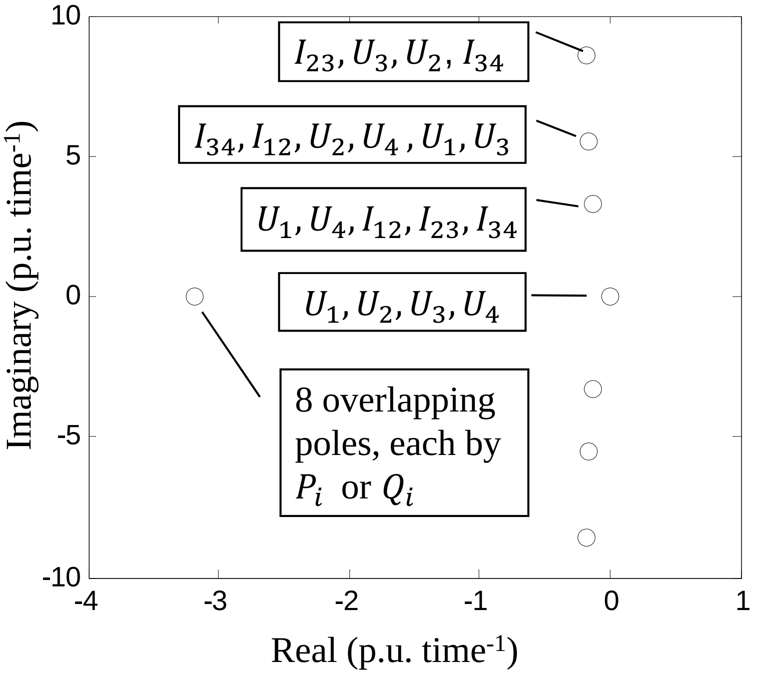

Figure 15: Eigenvalues of the open-loop system and their participating states

the uncertainty term $\alpha^2\mathbf{x}^\top\mathbf{H}^\top\mathbf{H}\mathbf{x}$ is scaled by α, which has been addressed by the weighted cost function in (4.6), norm of $\mathbf{H}$ becomes less important. However, since parameter h_{ii} corresponds solely to state x_i, it is useful for adjusting the behavior of an arbitrary state.

For the studied system under distributed control scenario, state feedback gain $\mathbf{K}$ is a 8-by-15 matrix with four nonzero blocks $\mathbf{K}_k$, $k = 1, \dots, 4$, each represents the distributed controller for its corresponding Terminal k. Here we use entries of $\mathbf{K}_1$ from the solved $\mathbf{K}$ to illustrate the inside of a nonzero block:

$$\mathbf{K}_1 = \begin{array}{c} \\ \Delta P_1^* \\ \Delta Q_1^* \end{array} \begin{array}{c} \begin{array}{ccc} \Delta P_1 & \Delta Q_1 & \Delta U_1 \end{array} \\ \begin{pmatrix} 0.3 & 0 & -77 \\ 0 & -0.003 & 0 \end{pmatrix} \end{array}.$$

Notice that there is one dominant entry, which is the gain of DC voltage increment ΔU_1 to control input ΔP_1^*. The same is observed in all other $\mathbf{K}_k$'s, each representing the local

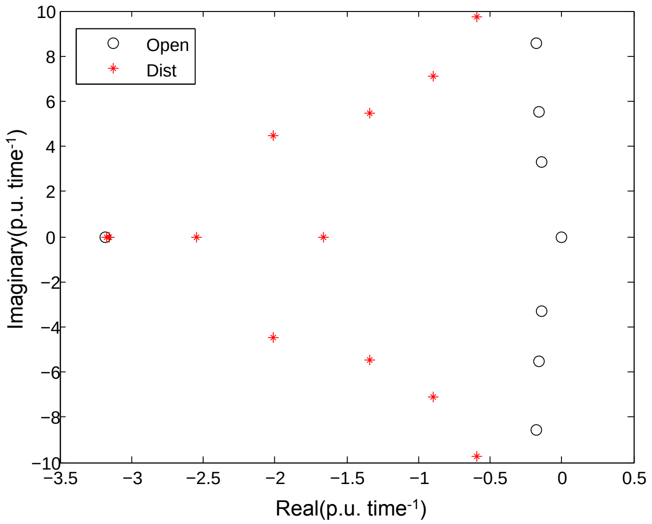

(a)

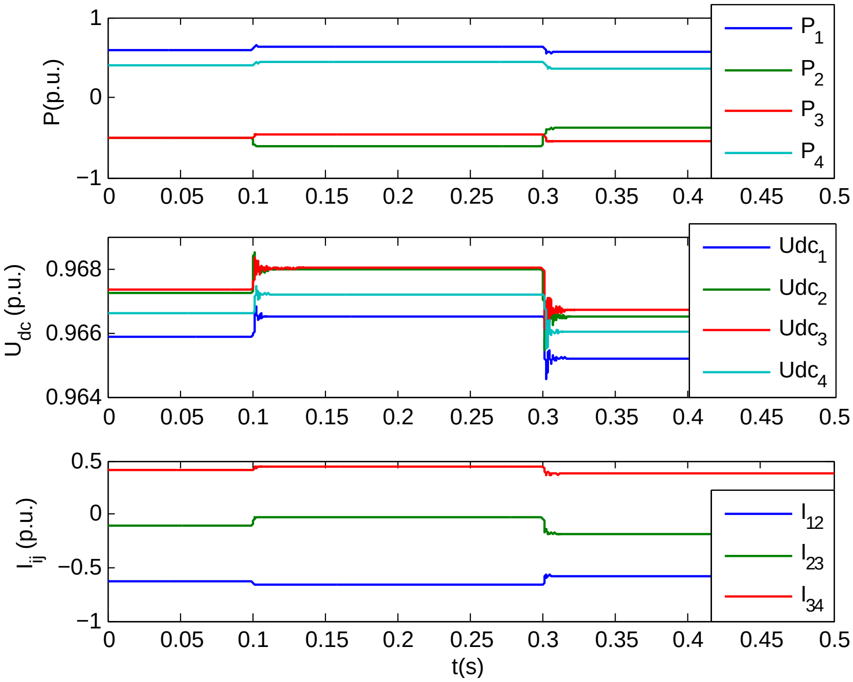

(b)

Figure 16: Close-loop dynamics of the MTDC system with **K** in distributed form solved by LMI optimization: (a)Eigenvalues (b)Simulation

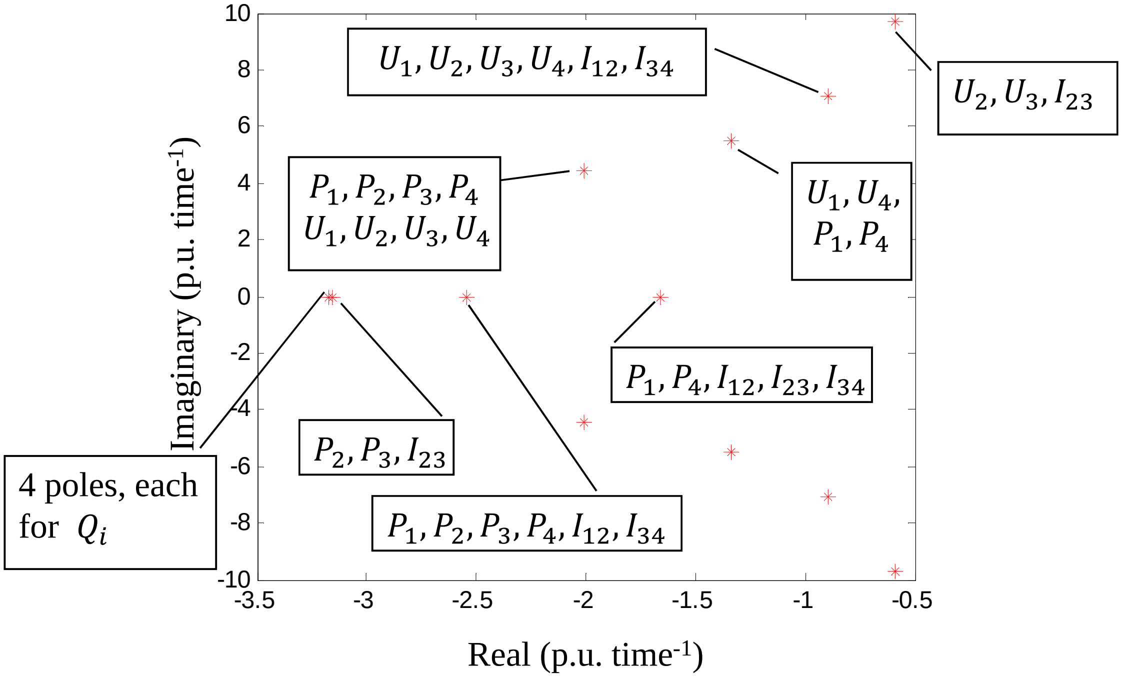

Figure 17: Participating states for close-loop eigenvalues in Figure 16(a)

control gain matrix of terminal k. If ignore the other very small entries, the distributed controllers are equivalent to droop controller:

$$\Delta P_k^* = K_{droop} \Delta U_k.$$

This implies that the LMI algorithm will automatically concentrate control effort on relevant states even without further nonzero specification within $\mathbf{K}_k$. So the LMI design approach can be used for droop gain selection, in case a simpler droop controller is preferred over state feedback controller in application.

After applying the solved gain matrix $\mathbf{K}$, close-loop dynamics of the studied system is shown in Figure 16: Close-loop eigenvalues are plotted in Figure 16(a) in red stars. while their related states is listed in Figure 17. Comparing with the open-loop eigenvalues (plotted in black circles), one can have the following observations:

- For the close-loop complex eigenvalues, which are all related to DC grid, their real parts are more negative compared to the open-loop ones. This results from the stabilizing effect from control gain matrix $\mathbf{K}$.
- The four real eigenvalues related to local reactive power control are not influenced by DC voltage control, due to the decoupling of real and reactive power control in local controllers. It can also be seen from entries of $\mathbf{K}$ that the controller has almost no effect on reference reactive power Q_i^*.
- The rest eigenvalues are originally one-to-one related to local control of P_i in open-loop system. But in close-loop system, $\mathbf{K}$ couples local DC voltages with real power controllers, which further introduce the physical coupling of DC grid. As a result, we could see participation of multiple terminals' and DC cables' states on these modes. Slower dynamics of the DC grid drags these eigenvalues toward right, i.e. larger time constant. It is the reason why there are three close-loop real eigenvalues closer to origin, compared with their open-loop counterparts. The fourth open-loop real eigenvalue related to P_i has merged with the one on origin, and they together become a complex conjugate pair in the close-loop system, which is related to all real power and DC voltage states.
- Control gain matrix $\mathbf{K}$ does not impose any mode that is faster than the inner controllers on VSCs.

Simulation of the close-loop system is shown in Figure 16(b). The analyzed scenario corresponds to disturbance on power extracted by Terminal 2, which brings P_2^* down by 0.2 p.u. at 0.1 second, then increase it by 0.4 p.u. at 0.3 second. It can be observed that all converters adjust their real power to compensate for the disturbance. DC states is regulated fairly well despite small high order oscillation on DC voltages. Maximum overshoot of voltage is 0.0014 p.u., while settling time being smaller than 17ms.

For the rest of this section, we are going to discuss the tuning of LMI parameters. The same MTDC system and control structure, i.e. nonzero pattern of gain matrix $\mathbf{K}$, is used to illustrate how to trade-off between control effort and performance, and how to adjust behavior of certain state or mode.

We first look at the three coefficients a_1, a_2, and a_3 in LMI cost function. Since both a_2 and a_3 are related to $\|\mathbf{K}\|$, one can trade-off control effort and performance by adjusting them

Table 2: Control effort and performance with different values of weight coefficient

$[a_1, a_2, a_3]$	$\|\mathbf{K}\|$	α	$\max(\|U_{k\infty} - U_{k0}\|)$ (p.u.)	U_k overshoot (p.u.)	Settling time (s)
$[0.05, 1, 1]$	10	0.009	0.0053	0.00022	0.0162
$[0.1, 1, 1]$	16	0.010	0.0032	0.00038	0.0157
$[0.5, 1, 1]$	49	0.012	0.0011	0.00040	0.0153
$[1, 1, 1]$	77	0.014	0.00074	0.00052	0.0099
$[1, 0.5, 0.5]$	119	0.015	0.00050	0.00057	0.0101
$[1, 0.1, 0.1]$	287	0.018	0.00024	0.00045	0.0097

as a group. The same disturbance on Terminal 2 is applied in simulation. Table 2 summarizes control effort and performance measurements using different $[a_1, a_2, a_3]$ combinations when $\mathbf{H} = \mathbf{I}$. It can be seen that larger a_1 leads to larger control gains but better response. Note that larger control gain does not lead to larger static real power bias from the system's operating point. The converters end up sharing the disturbance on real power to achieve the balance of input and output power. Close-loop eigenvalues of the same set of coefficients is shown in Figure 18, from which one can observe the following two trends of movement as $\|\mathbf{K}\|$ increases:

- The complex eigenvalues (DC grid related) move toward the left with larger control gain. This is in accordance with the DC voltage response in Table 2, showing smaller overshoot and faster settling time.
- The real eigenvalues that are originally related to real power control in open-loop system will first shift to left when small $\|\mathbf{K}\|$ is used. But they become less negative with higher value of control gains. This is because larger $\|\mathbf{K}\|$ imposes stronger coupling between the fast real power control loop and the slow dynamics of DC grid. Remind that the DC voltage is regulated through small adjustment ΔP_k^* on real power set values P_{k0}^*, making the overall reference value of real power control $P_k^* = P_{k0}^* + \Delta P_k^*$. the rightward movement of these real eigenvalues implies that the more converter k contributes to

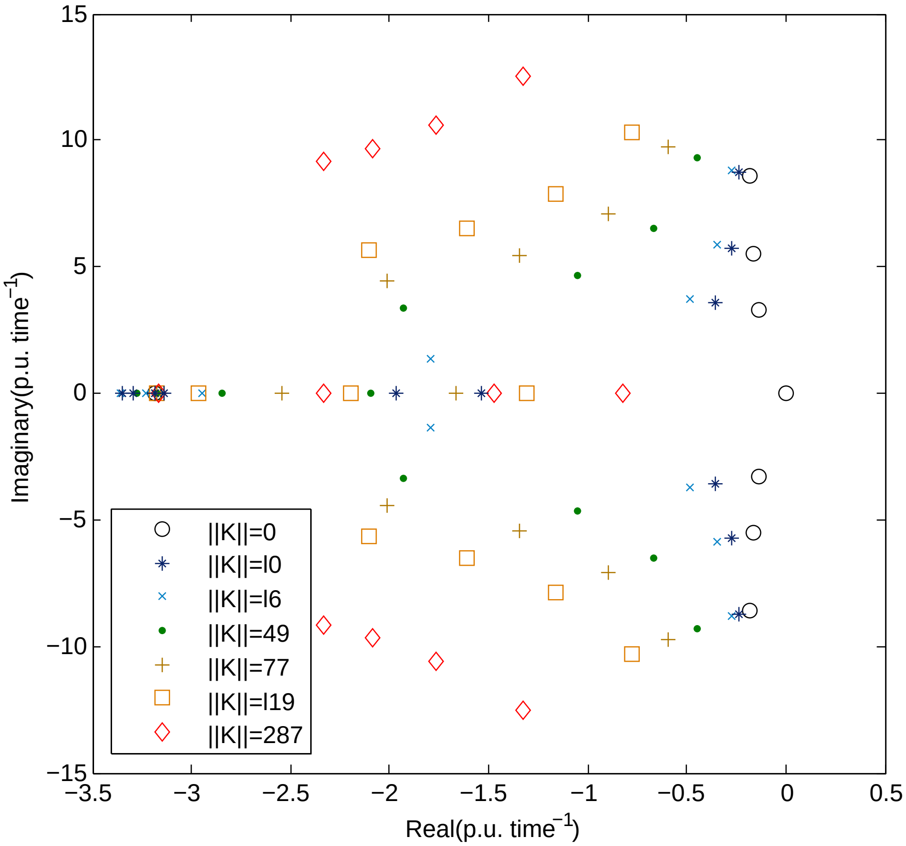

Figure 18: Close-loop eigenvalue with different values of $\|\mathbf{K}\|$ listed in Table 2.

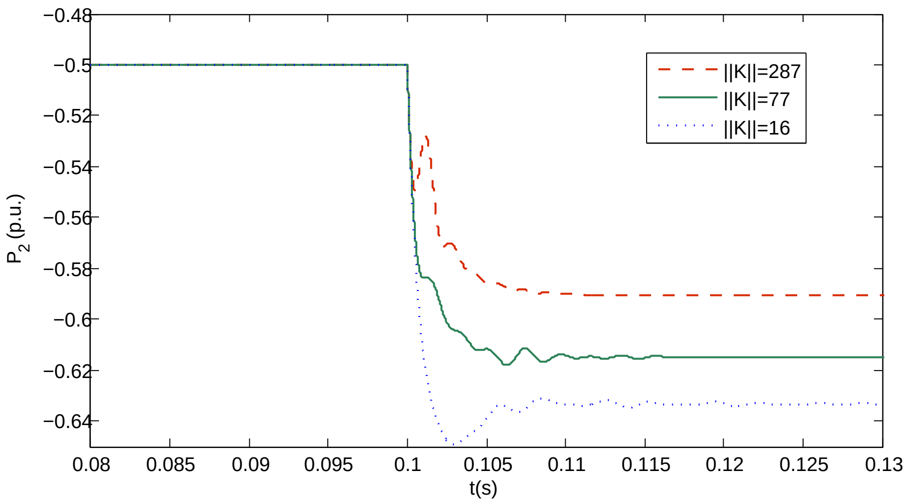

Figure 19: P_2 response to -0.2 p.u. step change of P_2^* using different $\mathbf{K}$

Table 3: Control effort and performance with different $\mathbf{H}$

Parameters	$\|\mathbf{K}\|$	$\max(\|U_{k\infty} - U_{k0}\|)$(p.u.)	U_k overshoot (p.u.)
Baseline	16.2	0.0032	0.0004
$H_{\mathrm{q-axis}} = 5$	16.2	0.0032	0.0004
$H_{\mathrm{d-axis}} = 5$	11.1	0.0047	0.0003
$H_{\mathrm{U}} = 5$	16.4	0.0032	0.0004
$H_{\mathrm{I}} = 5$	156	0.0004	0.0005
$H_{\mathrm{I}_{12}} = 5$	106	0.0006	0.0005
$H_{\mathrm{I}_{23}} = 5$	159	0.0004	0.0005
$H_{\mathrm{I}_{34}} = 5$	124	0.0005	0.0006

DC voltage regulation, the slower it will get to trace its own set value P^*_{k0}. This is demonstrated in Figure 19, showing Terminal 2's response to step change of P^*_2 at 0.1 second using different $\mathbf{K}$'s solved by LMI optimization.

The next set of parameters to study is matrix $\mathbf{H}$. So far it's been set as identity matrix, which set the same uncertainty tolerance to all states. Influence of individual state's tolerance setting is discussed in this paragraph. Experimental results are summarized in Table 3. For comparison, we use the $\mathbf{K}$ solved by parameters $a_1 = 0.1$, $a_2 = 1$, $a_3 = 1$, and $\mathbf{H} = \mathbf{I}$ as baseline. Remind that $\mathbf{H}$ is set in diagonal form $\mathrm{diag}(\ldots, h_i, \ldots)$, so that uncertainty tolerance of the ith state can be independently adjusted by entry h_i. In our study case, we found h_is that are matching to the same type of states show similar effect to LMI result. So in Table 3, entries of H are tuned in groups, and one group at a time (a row). For example, $H_{\mathrm{q-axis}}$ is defined as a set of h_i's, of which the corresponding states are on the q-axis of AC subsystems. So $H_{\mathrm{q-axis}} = 5$ means only h_i's corresponding to AC-side q-axis states are changed to 5 while the rest parameters stay the same as baseline. From Table 3, we can tell the influence of each group of states' matching entries in $\mathbf{H}$:

- q-axis states of AC subsystems: These states are for reactive power. Due to the decoupling of real and reactive power control, tuning the corresponding entries $H_{\mathrm{q-axis}}$ in $\mathbf{H}$ does not influence the resulting $\mathbf{K}$.

- d-axis states of AC subsystems: These states are for real power. Increasing their corresponding entries $H_{\mathrm{d-axis}}$ reduces $\|\mathbf{K}\|$. This is in accordance to what we observed in Figure 18, where smaller $\|\mathbf{K}\|$ drives a group of real poles more negative. These poles are contributed by states for AC real power in open-loop system, according to participation analysis in Figure 15.

- DC voltages at terminals: Entries of $\mathbf{H}$ corresponding to DC voltages are included in set H_{U}. Increasing these parameters leads to slightly higher $\|\mathbf{K}\|$.

- DC currents on cables: Entries of $\mathbf{H}$ corresponding to DC currents are included in set H_{I}. The solved $\mathbf{K}$ shows the most sensitivity to this set of parameters. Increase these entries leads to tremendously higher $\|\mathbf{K}\|$. To further study their effects, the last three rows show the result when entries in this set are tuned individually, i.e. only one entry is set to 5 while the others stay the same as baseline. Notice the difference in sensitivity, which we find in consistent with the norm of corresponding row in $\mathbf{A}$ (Table 4).

- Figure 20 compares the resulting eigenvalues obtained by parameters in line 1 and line 3 to 5 of Table 3. As we've observed in Table 3, parameters in H_{I} and $H_{\mathrm{d-axis}}$ have the opposite effect, while the same change on H_{U} shows very little influence. When scale the whole uncertainty term $\alpha^2\mathbf{x}^\top\mathbf{H}^\top\mathbf{H}\mathbf{x}$ by a_1 instead of tuning entries in $\mathbf{H}$, the result (legend $a_1 = 0.5$ in Figure 20) will trade-off between the effect of H_{I} and $H_{\mathrm{d-axis}}$.

After synthesizing the experimental results of parameter tuning, we find the following topics worth further discussion:

The first is about sensitivity of LMI result to different entries in $\mathbf{H}$. Why do the matching entries of one group of states has significantly stronger influence compared to those of another group? Remind tchat in the LMI problem formulation (4.6), the term $\alpha^2\mathbf{x}^\top\mathbf{H}^\top\mathbf{H}\mathbf{x}$ is introduced as a boundary of uncertainty for the state space model. Does Table 3 implies that the controller or the close-loop system is highly sensitive to DC current's uncertainty? The following discussion shows that such implication is not correct.

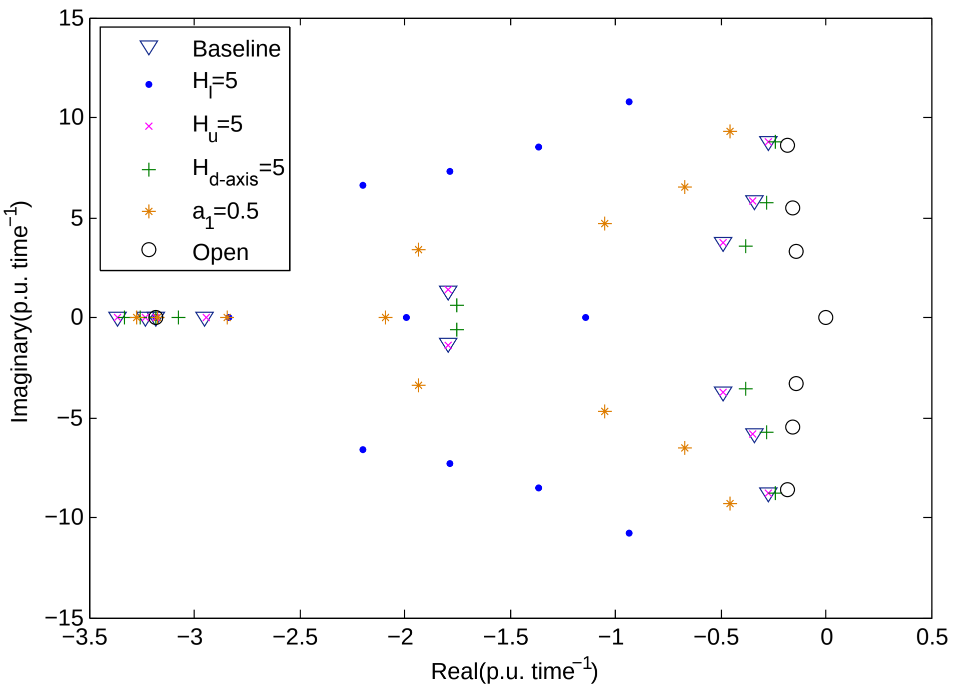

Figure 20: Close-loop eigenvalue with different parameter matrix $\mathbf{H}$ and coefficient a_1

It has been mentioned that the level of effect of h_i toward control matrix $\mathbf{K}$ is in consistent with norm of the ith row in system matrix $\mathbf{A}$. In other words, the higher absolute value the entries in row i have, the bigger effect h_i will impose on solved $\mathbf{K}$. This suggests strong dependence on system parameters and their units. For example, in per-unit system, coefficients for DC current dynamics are in general much larger than that of DC voltage; however, when using SI units for the same study case, it is the opposite. Table 4 lists the norm of selected $\mathbf{A}$'s row for the same study case in per unit and SI unit, demonstrating the difference caused by choices of unit. When applying LMI algorithm in the same system in SI unit, $\mathbf{K}$'s sensitivity to h_i changes accordingly. Thus we can conclude that h_i's effect to LMI result depends on unit and scaling of physical quantities, and cannot indicate system's robustness by itself. To further demonstrate that LMI algorithm's sensitivity to h_i is different from controller's sensitivity to disturbance on the ith state, a 0.01 p.u. disturbance is added to U_1 (Figure 21(a)) and I_{12} (Figure 21(b)) in simulation at initial condition. The control

Table 4: Norm of **A**'s row for state P_1, U_1, and DC currents

	$\|A(P_1,:)\|$	$\|A(U_1,:)\|$	$\|A(I_{12},:)\|$	$\|A(I_{23},:)\|$	$\|A(I_{34},:)\|$
Per unit	3.2	0.15	203	405	253
SI unit	1000	6667	300	574	367

matrix $\mathbf{K}$ is solved by baseline parameter $a_1 = 0.1, a_2 = a_3 = 1$ and $\mathbf{H} = \mathbf{I}$. Result in Figure 21 shows that both types of disturbance are mitigated in the close-loop system. Disturbance on U_1 results in larger system response, because it introduces a much larger change in real power considering the size of capacitor on DC side.

Now we know that effect of h_i depends on unit and scaling of physical quantities, we can use elements in the ith row of system matrix $\mathbf{A}$ as a rough guideline for choosing the tuning step of h_i: small norm of row i requires large changing step of h_i. Note that another way to obtain $\mathbf{H}$ is to derive model of uncertainty for each state and then try to find an upper bound in quadratic form. In this case, $\mathbf{H}$ is no longer parameter but part of the model. However, this could involve nonlinearity of system, uncertainty of measurement, as well as stochastic characteristic of power system, which are out of the scope of this work. Here, $\mathbf{H}$ is merely used as parameters that would influence the placement of close-loop eigenvalues.

The second discussion is on $\mathbf{H}$'s influence to close-loop eigenvalues. Remind that the reason to tune individual entries of $\mathbf{H}$ in addition to coefficient a_1 in (4.6) is to adjust response of a certain state. In terms of pole placement, it is also expected to help improve specified eigenvalues by tuning the matching h_i's found through participation analysis. Even though the mapping between eigenvalues and h_i is not one-to-one, it should provide more flexibility in placement of eigenvalues, comparing to tuning just a_1, which scale the uncertainty term as a whole. However, the result shows such flexibility is not achieved when using distributed control structure, i.e. $\mathbf{K}$'s nonzero pattern in form of Figure 13(a):

Figure 22 shows the close-loop eigenvalues resulted from tuning entries in set H_{I}, which are corresponding to current on DC cables. Note that we are looking at this set of parameters because: 1)their corresponding states are closely related to the crucial complex eigenvalues,

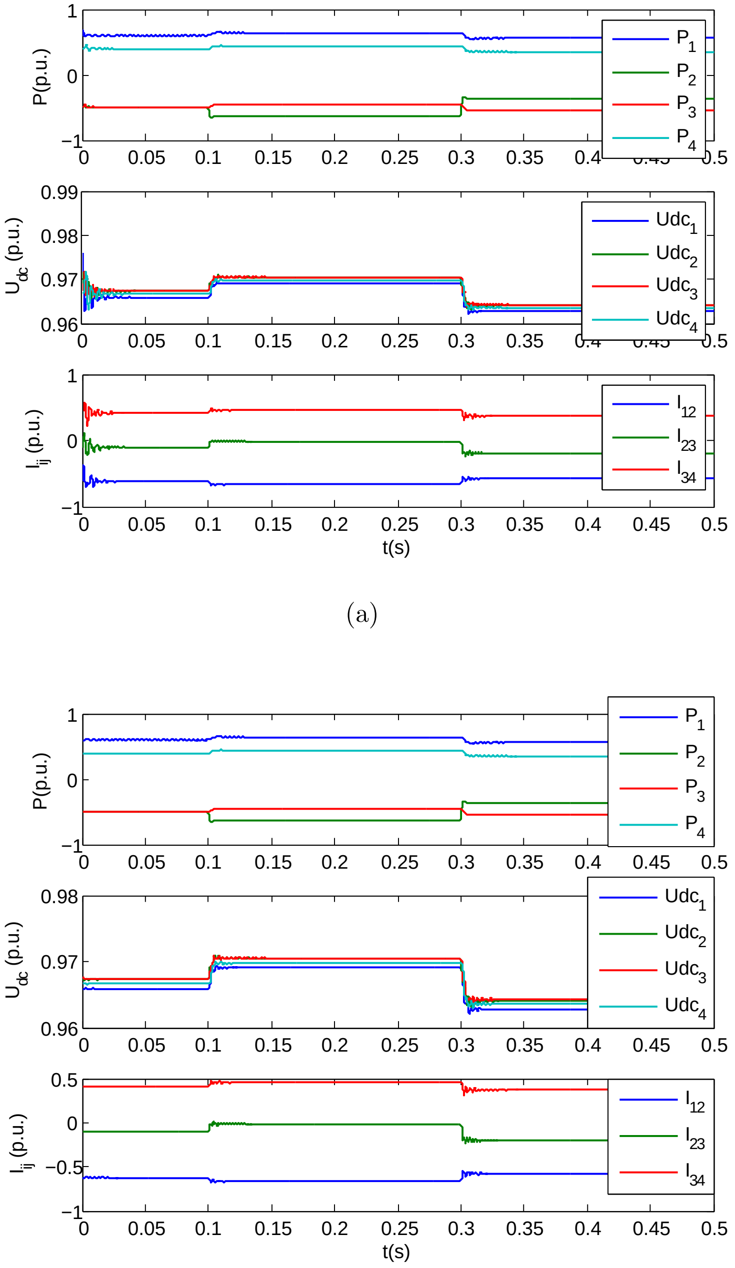

(a)

(b)

Figure 21: Close-loop system response to disturbance on different states at initial condition: (a) 0.01 p.u. disturbance is added on U_1 (b) 0.01 p.u. disturbance is added on I_{12}

which locate close to imaginary axis; 2)they are in the same unit, and thus have comparable influence on LMI result according to the first discussion. In Figure 22, the last four in legend are matching with the last four rows in Table 3. It can be observed that by changing individual entries in H_{I} (last three in legend), we end up influence all eigenvalues, instead of just the subset that are participated by h_i's matching state. Note that when only $H_{\mathrm{I}_{23}}$ is changed, the resulting eigenvalues overlap with the ones when all entries in H_{I} are changed at the same time. This is a sign that some poles are pushed further left then what is necessary to satisfy the linear inequality conditions in (4.6). Moreover, movement of all poles are following the trend that has been observed in Figure 18 when $\|\mathbf{K}\|$ changes. In other word, the same pole placement can be achieved by simply tuning coefficients a_1 in (4.6). So in this case, we do not get any benefit from tuning $\mathbf{H}$.

This can be explained by the reduced controllability caused by information constraint on matrix $\mathbf{K}$. Despite the MTDC system model is controllable, when using distributed control on the test case, we cannot improve behavior of a given state or a subset of modes without influence the rest. For example, if more damping is required on the complex eigenvalues, the resulting controller will also lead to faster response of DC voltage regulation and slower tracking of local real power reference. If such result is not satisfying, one should either turn to non-control method that improve open-loop system dynamics or consider adding communication between terminals. The later option will be further studied in this work.

Last but not least, a general guideline for LMI parameter tuning for distributed $\mathbf{K}$ is given in this paragraph. One can first adjust the relative importance of performance and control effort through coefficient a_1, while a_2 and a_3 are fixed as a group. When improvement is wanted on certain state or eigenvalue, one can proceed to tune the corresponding entries in $\mathbf{H}$. However, according to our second discussion, it is very likely that the resulting controller can also be obtained by tuning a_1, when controllability is limited by distributed $\mathbf{K}$. In this case, the function of $\mathbf{H}$ is merely for the convenience of user by providing a straightforward mapping to close-loop performance of individual states, which is beneficial when scale of system reach to a point that thorough analysis on pole movement becomes difficult. For example, it is shown in Figure 20 that LMI algorithm will balance the inherent trade-off between local and grid-level control performance when a_1 is tuned. One can adjust this

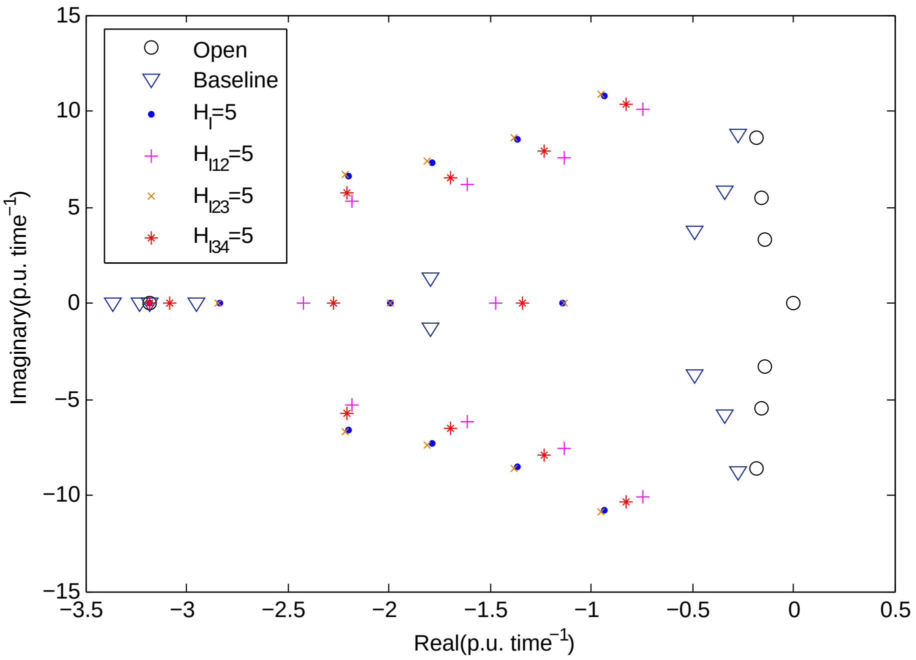

Figure 22: Close-loop eigenvalue with different choices of **H**

balance through parameters in set $H_{\mathrm{d-axis}}$ and H_{I}, without having to understand $\|\mathbf{K}\|$'s effect on each group of eigenvalues and their related states.

To summarize this section, we use the proposed LMI-based method to design distributed controller for the study case of a four-terminal system, of which the non-zero pattern of **K** is set in the form of Figure 13(a). Simulation result and close-loop eigenvalue shows that the solved controller can successfully regulate DC voltage and maintain power balance of the system. A closer look inside the resulting **K** shows that control effort will concentrate on the gain between relevant state and control output within a non-zero block. So the LMI optimization algorithm can also be used to choose droop gains when simple droop controller is preferred. To further understand the influence of LMI parameters, we tune the coefficients a_1, a_2, and a_3, as well as parameter matrix **H** and study the results. These results verify that trade-off between control performance and effort can be adjusted through the three coefficients. Furthermore, by studying participation factor and movement of eigenvalues as $\|\mathbf{K}\|$

increases, we find the inherent trade-off between performance of local real power tracking and system DC voltage regulation, for which the LMI optimization will automatically find a balance. We then show that such balance can be adjusted through tuning entries in **H**. Towards the end of this section, the tuning procedure is thoroughly discussed and summarized. We conclude that constraints on gain matrix **K**'s structure reduces controllability of system, and thus limit the flexibility on pole placement.

5.2 PARTIALLY PARTICIPATING VOLTAGE REGULATION

In this section, we consider a special case of distributed control, in which only a subset of terminals participate in DC voltage regulation. This scenario allows the terminals that are not in charge of grid stability to focus on their local control goals. An example of such partially participating voltage regulation was proposed in [51] for offshore wind integration. This control scheme includes several operating modes for normal operation and fault events. In each mode, DC voltage is regulated by either grid-side inverters or wind farm rectifiers, while the rest converters only control their local performance, such as MPPT or limiting fault current/voltage.

The described scenario can be achieved by configuring the matching non-zero pattern for gain matrix **K** in our LMI formulation. For demonstration, we consider the case that DC voltage is regulated by the two output terminals: Terminal 1 and Terminal 4, and they each use local measurement for feedback. In this case, non-zero pattern of gain matrix **K** is set in form of Figure 23(a), in which non-zero entries are denoted by dark gray. Compared to the basic distributed control case (Figure 13(a)) that we considered in Section 5.1, non-zero blocks for Terminal 2 and 3 are replaced by zeros as they do not contribute to system stabilization.

Applying the solved controller to our four-terminal test case, we get the time-domain response shown in Figure 23(b). In the top plot, when P_2^* is changed at 0.1s and 0.3s, only P_1 and P_4 react to balance the disturbance, meanwhile Terminal 2 and 3 are merely tracking their local references. In the lower two plots, it can be seen that the system is successfully

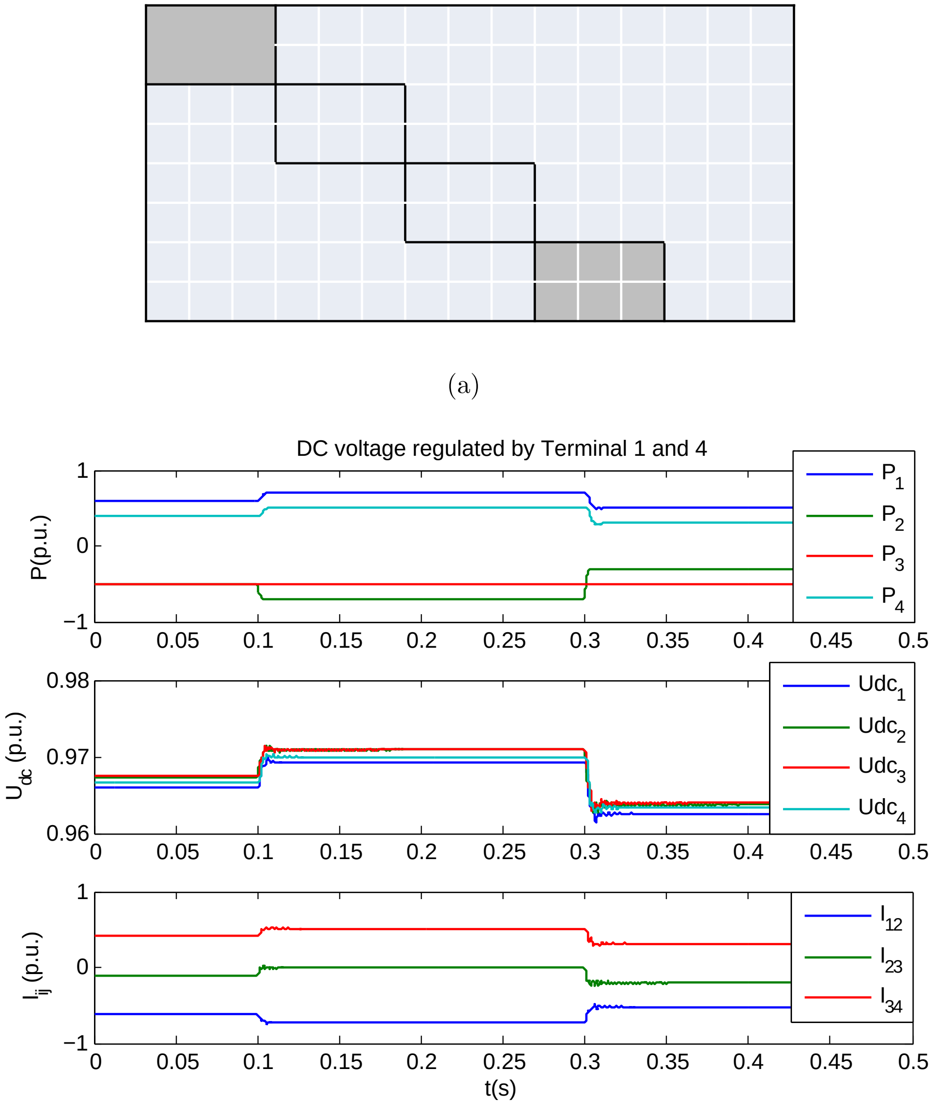

(a)

(b)

Figure 23: Partially participating DC voltage regulation by Terminal 1 and 4. (a) Non-zero pattern of gain matrix **K** (b) Simulation result

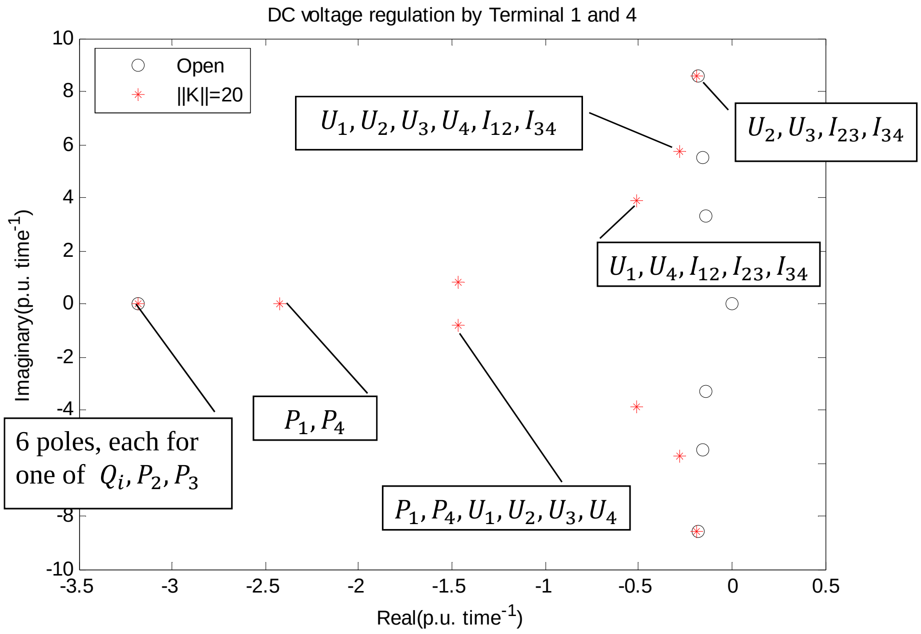

Figure 24: Corresponding eigenvalues for Figure 23(b) and their participating states

stabilized by the two output terminals. Close-loop eigenvalues of this system is plotted in Figure 24 to further verify that the system is stable. Through participation factor between the poles and the states, we observe two major differences comparing to the basic distributed controller (Figure 13(a)) studied in Section 5.1:

- Eigenvalues corresponding to real power control of Terminal 2 and 3 are not changed by solved **K**, which is clearly expected as the two do not contribute to voltage regulation, i.e. grid power balancing. It confirms that the two terminals are fully operated for their local control goals.

- One conjugate pair of complex eigenvalues related to U_2, U_3, I_{23}, and I_{34} are hardly moved by the controller. Corresponding to time-domain response in Figure 23(b), DC voltage U_2 and U_3 have longer settling time than U_1 and U_4. It implies that their related poles are not as well damped.

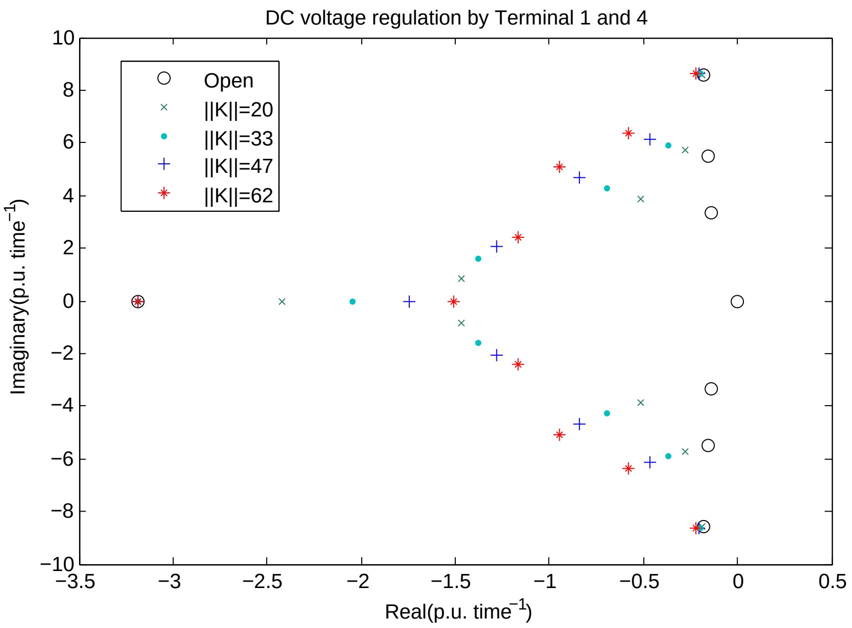

Figure 25: Close-loop eigenvalue with different values of $\|\mathbf{K}\|$, when Terminal 1 and 4 regulate DC voltage

Same as we studied in Section 5.1, trade-off between performance and control effort can be adjusted through LMI parameters in (4.6). To avoid duplication, we only compare the close-loop eigenvalues resulting from different norm value of solved $\mathbf{K}$ in this section (Figure 25). All controllers have the same non-zero pattern of Figure 23(a). Despite the uninfluenced poles for reactive power and input terminals' real power, we observe the inherent trade-off between local (poles related to P_1 and P_4) and grid-level (complex poles participated only by DC-side states) control performance. Same as what is found in Section 5.1 Figure 18, when $\|\mathbf{K}\|$ increases, the later group of poles move toward left while poles in the prior group move toward right. Compared to the controller in Section 5.1 , the major difference is the conjugate complex poles participated by U_2, U_3, I_{23}, and I_{34}. It is barely moved even with large control effort, which is sign of further loss of controllability. Because this pair of eigenvalue becomes almost uncontrollable with too little non-zero entries in $\mathbf{K}$, LMI algorithm sometimes encounter problem with certain parameters.

To sum up, we study the partially participating DC voltage regulation in this section. It is a special case of distributed control, in which only a subset of terminals contribute to grid-level control, allowing the rest terminals fully operated for their local control goals. Simulation result shows that the LMI-based approach still manage to stabilize the test case with only the two output terminals, despite longer settling time on some of the states. A further eigen analysis reveals that this level of limitation on **K** make some critical poles almost uncontrollable. As a result, their corresponding mode in system dynamics cannot be improved through controller.

5.3 COORDINATED VOLTAGE REGULATION

This section studies coordinated voltage regulation, in which communication is available among terminals. With the advantage of our configurable controller model, various network configurations can be easily implemented by just changing the nonzero pattern of gain matrix **K**. In practice, the resulting **K** can be implemented at local control level, in which controller of each terminal receive feedback from multiple terminals. The other possible implementation is to have a higher level central controller that has global observation, which, similar to secondary control in AC system, compensates the local distributed controllers. In this section, the same test case of Figure 14 is used, so results can be compared with the distributed scheme.

5.3.1 Voltage regulation by communicating local measurement

We first consider the case that each converter shares its local measurement with the other. The corresponding nonzero pattern is in form of Figure 13(b). Remind that, when assembling the system level state space model, the subsystems' states are stacked up on top while the coupling states are arranged at the end. So in Figure 13(b), the nonzero columns on the left are corresponding to the subsystems, meaning that measurements of local states are globally available to other terminals; on the other hand, the zero columns on the right indicate that

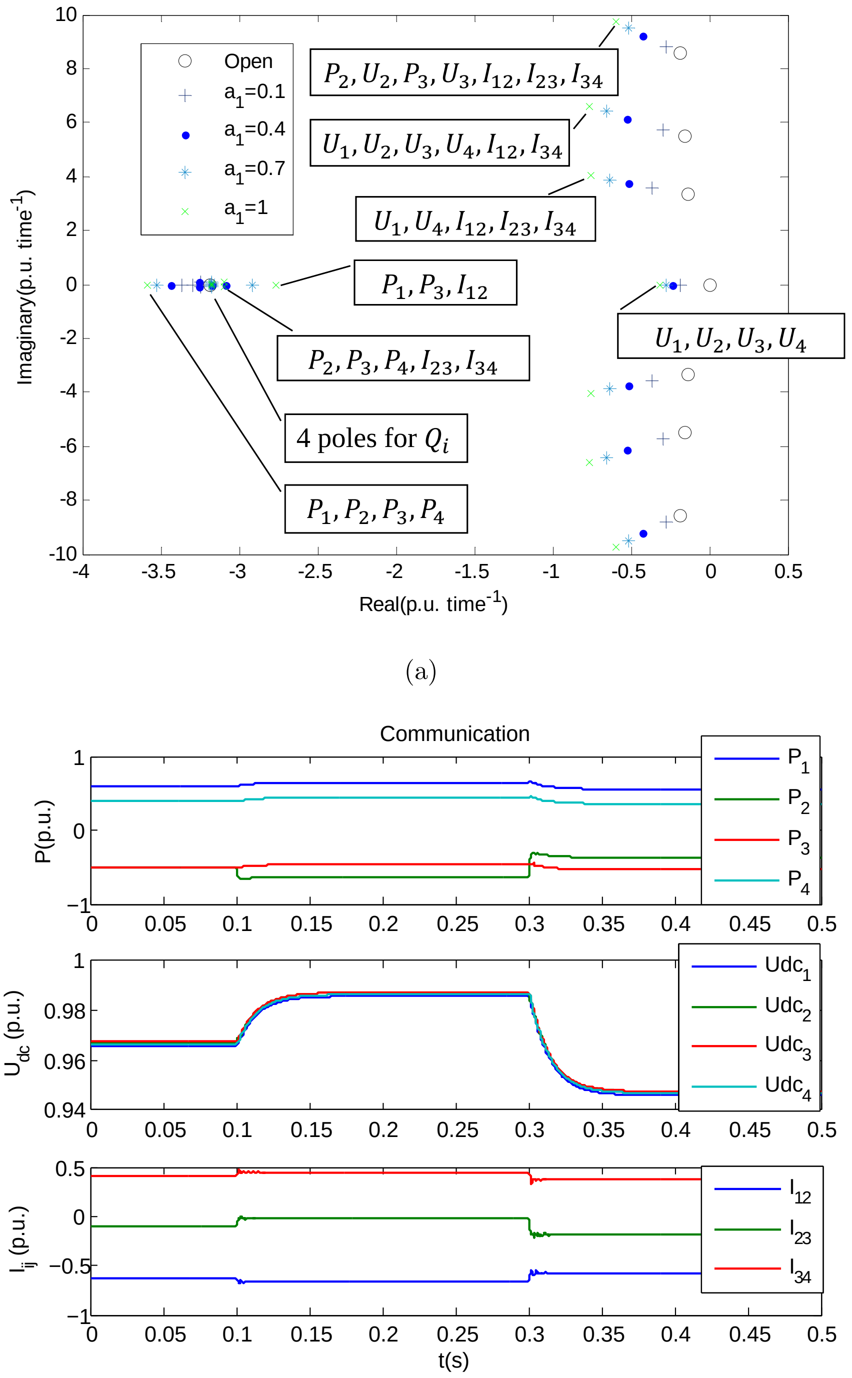

(a)

(b)

Figure 26: Coordinated DC voltage regulation: (a) Close-loop eigenvalue with different values of coefficient a_1 (b) Simulation result when $a_1 = 0.4$

current on DC cables are either not measured or the measurements are not feedback in real time to controllers in terminals.

As described in Section 4.2, specified nonzero pattern of gain matrix $\mathbf{K}$ is obtained by setting nonzero pattern of matrix $\mathbf{L}$ and $\mathbf{Y}$ accordingly in LMI optimization. While $\mathbf{L}$ is having identical nonzero pattern as $\mathbf{K}$, matrix $\mathbf{Y}$ has several options: diagonal nonzero entries, block-diagonal pattern with the same block-wise dimension as subsystems, and last but not least, one large nonzero block that covers all subsystems. All these nonzero patterns preserve $\mathbf{L}$'s pattern after right-multiplied by inverse of $\mathbf{Y}$, while the later has more variables to search than the prior. After experimenting with these possible non-zero patterns, only the last option gives non-negligible off block-diagonal entries in solved $\mathbf{K}$, which means the non-distributed control scheme is actually deployed. As a result, the last option of $\mathbf{Y}$'s nonzero pattern is used in all LMI optimization in this subsection. Even though it has the most nonzero entries to search, better result is found in this extended solution space.

Table 5: Coordinated control effort and performance with different values of a_1

a_1	$\lVert\mathbf{K}\rVert$	$\max(\lvert U_{k\infty} - U_{k0}\rvert)$ (p.u.)	U_k overshoot (p.u.)	U_k settling time (s)	I_{jk} overshoot (p.u.)	I_{jk} settling time (s)
0.1	17	0.027	0	0.081	0.073	0.035
0.4	43	0.020	0	0.058	0.042	0.022
0.7	62	0.016	0	0.048	0.030	0.017
1	78	0.014	0	0.045	0.023	0.011

We start with adjusting coefficient a_1 to roughly find a balance between system response and control effort. Meanwhile, the other parameters are fixed at: $a_2 = a_3 = 1$, $H_{\mathrm{U}} = 10$, and the rest of $\mathbf{H}$' diagonal entries is 1. The results are summarized in Table 5 and Figure 26(a). In Table 5, settling time is measured when a controlled output reaches and stays within the 2% error band of its final value.

In Table 5, when a_1 is increased, DC-side response is getting faster at the cost of larger control effort. However, in this case, what can be achieved in voltage regulation speed is relatively limited. This can be seen in Figure 26(a), where the DC voltage related eigenvalue on real axis displays sluggish movement as a_1 increase. Having this voltage related eigenvalue remain on real axis also implies smooth first order response on all terminals' DC voltage, which is why we see zero overshoot for voltage in Table 5. Figure 26(b) plots close-loop simulation result when $a_1 = 0.4$. One can see the first order dynamic on DC voltages in the middle plot. In the upper plot, all terminals contribute to counterbalance disturbance on P2 at 0.1s and 0.3s. And the system is successfully stabilized with regulated DC voltage.

It has been shown that communication among terminals leads to smoother control compared to the distributed case in Section 5.1. In the following paragraphs, we further tune the LMI algorithm to solve for different speed of response. Since a_1 along has little influence on DC voltage related eigenvalue, we use corresponding entries in matrix $\mathbf{H}$ to specify the relative importance of these states. For baseline, we take the LMI parameters that solved controller used in Figure 26(b), and only change entries in $\mathbf{H}$. Table 6 and Figure 27 summarize the close-loop performance of the resulting controllers.

The results shows that larger DC voltage related entries in $\mathbf{H}$ leads to solution with faster response of these states. Moreover, in this control structure, DC voltages preserve their smooth first order behavior even at high control speed. In Table 6, voltage overshoot remains zero for settling time as small as about 10 milli-seconds, which cannot be achieved using distributed controller in Section 5.1. Figure 27(a) shows the same characteristics of this coordinated control scheme in form of eigenvalue: with increased performance specification on DC voltages, their most related eigenvalue moves toward left along the real axis. Also observed in eigenvalues, oscillating poles can be further reduced when DC current related entries in matrix $\mathbf{H}$ are increased. An example is shown in Figure 27(a) by diamond markers. Comparing to the eigenvalues in star, one complex conjugate pair is moved onto real axis when DC current corresponding entries are raised from 1 to 2, leaving only two oscillating modes compared to four when using droop control.

Compared to distributed control scheme in Section 5.1, communication among terminals introduces two distinguish features in performance:

- The first is lower order dynamics on DC voltage. In eigenvalue analysis, DC voltage is consistently dominated by first order modes. The difference can be explained by comparing movement of poles under the two control schemes.

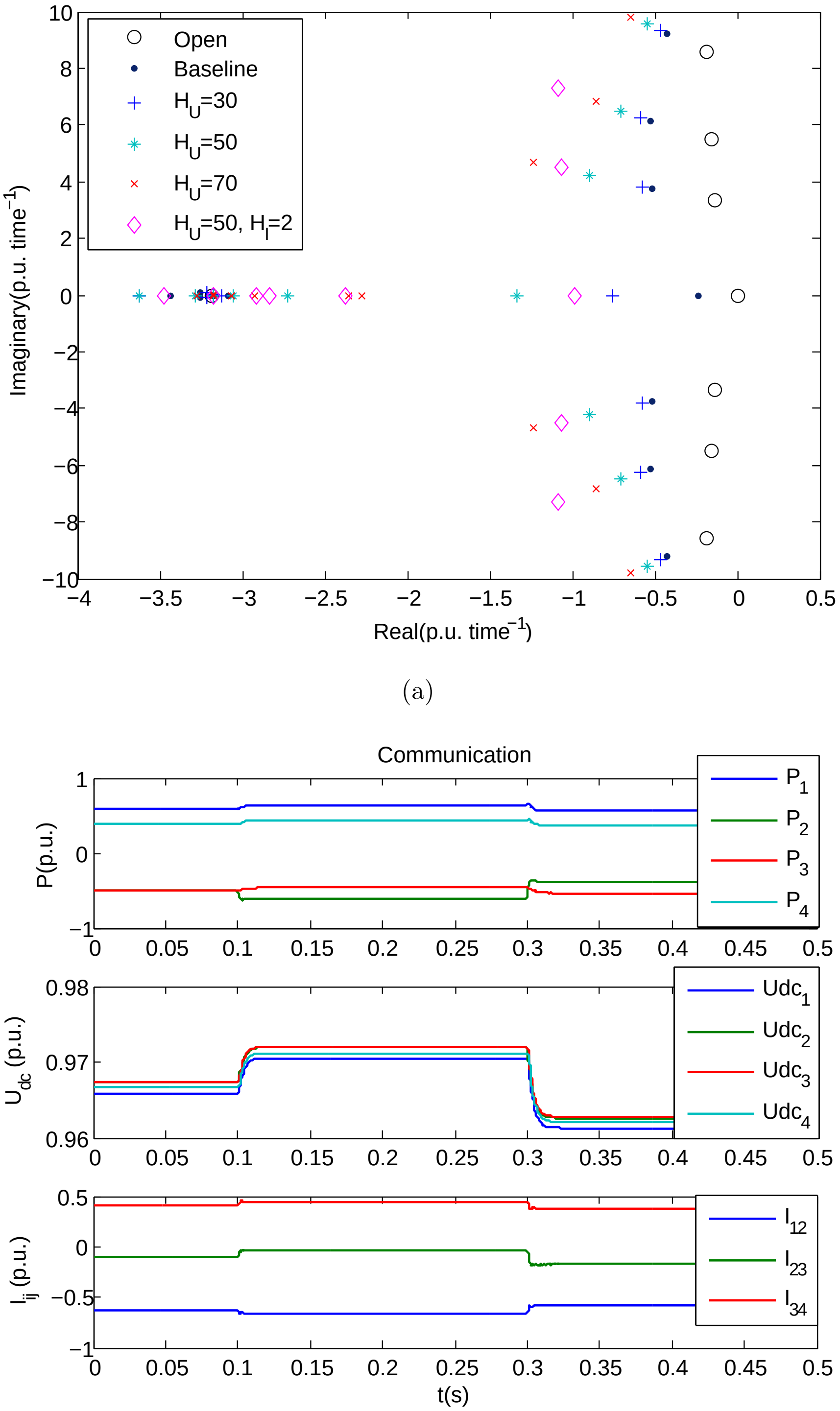

(a)

(b)

Figure 27: Coordinated DC voltage regulation under different choices of $\mathbf{H}$: (a) Close-loop eigenvalue with different $\mathbf{H}$ (b) Simulation result when $H_{\mathrm{U}} = 50$ and $H_{\mathrm{I}} = 2$

Table 6: Coordinated control effort and performance with different $\mathbf{H}$

Parameters	$\|\mathbf{K}\|$	Max voltage bias (p.u.)	U_k overshoot(p.u.)	U_k settling time (s)	I_{jk} overshoot(p.u.)	I_{jk} settling time (s)
Baseline	43	0.020	0	0.058	0.042	0.022
$H_{\mathrm{U}} = 30$	51	0.0055	0	0.018	0.026	0.018
$H_{\mathrm{U}} = 50$	66	0.0033	0	0.011	0.021	0.013
$H_{\mathrm{U}} = 70$	84	0.0023	0	0.0078	0.010	0.012
$H_{\mathrm{U}} = 50$, $H_{\mathrm{I}} = 2$	123	0.0047	0	0.014	0.0084	0.010

Let's first remind the trade-off between real power and DC voltage control. It has been observed in all scenarios that once feedback of DC voltage is introduced, some power related real poles will shift toward right as the voltage related real pole moves left. When control gain is increased, the voltage related pole will at some point merge with one of the power related pole and form an extra pair of complex poles, in other word, introducing one more oscillating mode.

Now comparing Figure 18 and Figure 27(a) for eigenvalue movement. When distributed control is applied, the extra oscillating mode forms at a relatively lower control speed and control gain. In contrast, when terminals communicate their local measurement, the merge of real poles does not happen during the tuning experiment at the same settling time range. Even though two real pole has come very close at the highest control speed that we tested. It is a sign that the local controllers are coordinated to reduce the right shift of power related poles, thus mitigate the side effect on local real power control and avoid unwanted oscillation.

- The second is the increased independence between DC voltages and DC currents related poles. Figure 27(a) has shown the different effects of DC voltage and current related entries in matrix $\mathbf{H}$. It is possible to improve the position of a subset of poles by fine tuning on **H** without pushing all poles unnecessarily faster. Although it is not possible to achieve individual pole placement due to limited control structure, we have more control over position of poles compared to the distributed control scheme.

Finally, the solved control gain **K** is examined. Using nonzero pattern as Figure 13(b), **K**'s dominant entries are the gains of DC voltage increments at each terminal ΔU_i, $i = 1, \dots, 4$ to a local control signal ΔP_k^*. If ignore the other very small entries, the solved controllers are equivalent to weighted feedback of communicated measurements:

$$\Delta P_k^* = \sum_{i=1}^{N} K_i \Delta U_i.$$

This control structure was proposed by Berggren et al. [20] in their patent for power flow control in DC network. This again verifies that the solved **K** converges to a solution in accordance with engineering designed control structure. If one want to use such weighted droop controller, the LMI-based algorithm provides a convenient way to determine control gains. Meanwhile, manual tuning of such controller can be challenging, if possible, due to increased number of parameters.

To summarize this section, we apply the proposed LMI-based method to the four-terminal study case with **K**'s non-zero pattern in form of Figure 13(b). Such control structure allows communication of local states among terminals. Simulation result and close-loop eigenvalue shows that the solved controller can successfully stabilize the system. Following the tuning procedure discussed in Section 5.1, we tune the close-loop system in different speed and study the resulting eigenvalues. Compared to distributed control scheme in Section 5.1, communication among terminals introduces two distinguish features: 1. First order DC voltage dynamic; 2. Increased capability of adjusting eigenvalue positions. Both effects benefit from coordination among terminals. In the end of this section, elements inside the non-zero block is studied to show the LMI-based method only assign gains between most relevant states and control signal. The resulting structure of gain matrix **K** is very similar to human designed controller when the same communication is available.

5.3.2 Voltage regulation by full-state feedback

In this section, we consider the case in which all measurements can be communicated. The corresponding nonzero pattern is in form of Figure 13(c), which is a full state feedback. Compared to scenario in previous section, control signal is decided not only based on states at each terminal but also measurements on cables. Such control scheme requires sensors and real-time communication available on cables. When full state feedback is possible, classic design methods like pole placement and linear-quadratic regulator(LQR) can also be used. Comparing to LMI-based algorithm, which numerically search for suboptimal solution, LQR can solve the optimal controller for a given set of weighting factors. So the purpose of this scenario is less for practical application but more for verification of LMI's solution against the optimal controller solved by LQR method.

Since the two optimization methods have different formulation and parameter sets, we compared the two by tuning them to the same desired pole position. For this experiment, the goal is to have the nominal mode, i.e. the DC voltage related real pole, close to -1.4, which leads to time constant of about 2.5ms.Then fine tuning is performed on DC current related parameters to mitigate oscillation caused by complex poles. The resulting LMI parameters are $a_1 = 0.1$, $a_2 = a_3 = 1$, $H_{\mathrm{U}} = 50$, $H_{13} = 0.5$ while the other diagonal entries of $\mathbf{H}$ is 1. On the other hand, LQR parameters that leads to comparable time domain performance are $\mathbf{R} = 5\mathbf{I}$, $\mathbf{Q}_{\mathrm{U}} = 1000$ while the other diagonal entries of $\mathbf{Q}$ is 1.

Using resulting gain matrix $\mathbf{K}$s solved by the two design methods, eigenvalues of close-loop systems are plotted in Figure 28. And the time domain simulation result are shown in Figure 29. The two sets of poles can be compared in three groups according to their open-loop participation factors in Figure 15.

- The first group is the single DC voltage related real pole, which is the nominal mode of the system. Both controllers can place it to desired position. This is consistent with what's observed in Section 5.3.1. When communication between terminals exists, it is relatively easy to adjust this pole along real axis without introducing extra oscillation modes. In practice however, control speed can be achieved is also limited by communication delay, which is not modeled in this work.

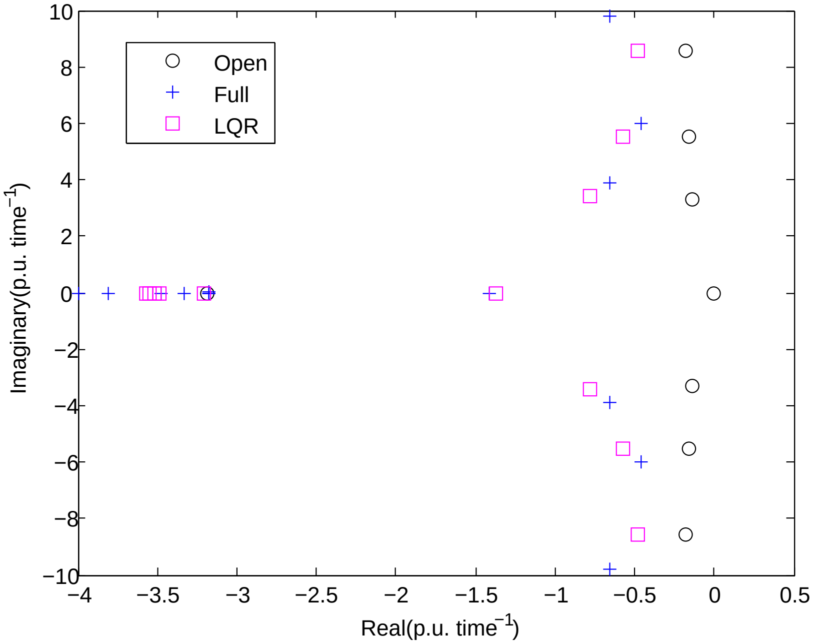

Figure 28: Close-loop eigenvalues using full state feedback solved by LMI and LQR methods

- The second is the group of DC current related complex poles, which are the oscillation modes of the system. Figure 28 shows that slightly better pole positions can be achieved by LQR the LMI solved control gain **K**. However, when comparing simulation results of the two in Figure 29, the difference in time domain performance is small enough that no obviously larger oscillation can be observed.

- The last group is the AC power and reactive power related real poles, which are already stabilized and controlled by local controllers. Comparing to LQR, LMI solved controller locates poles in this group a bit more toward left. This is considered a waste of control effort. Because these modes are already tuned sufficiently fast by local control. Further speeding up these modes is unnecessary and has little improvement on time domain performance (Figure.29), as the system's dynamic is dominated by the slower DC related modes. This implies that LMI solved controller is not as efficient as LQR. In this test case, $\|\mathbf{K}\|$ solved by LMI is 34.7% larger than that of LQR. It shows the

LMI-based method cannot guarantee optimal solution, which is the major limitation of this numerical method comparing to LQR.

In summary, this section studies coordinated voltage regulation, in which communication is available on all terminals and cables so that full-state feedback is possible. We use this test case to compare LMI and LQR solved controllers. By comparing close-loop eigenvalues and time domain simulation, the two can achieve the same performance on DC voltage regulation, and comparable close-loop dynamic on DC currents. However, the numerically solved controller by LMI is not as efficient as LQR, due to its unnecessary control effort on less critical modes that are already well controlled by local inner controllers.

5.4 SUMMARY

In this chapter, the proposed modeling and control design method is applied on a four-terminal HVDC system. Four different control topologies is tested by configuring the gain matrix **K** into different nonzero patterns in LMI algorithm. Under each control schemes, we demonstrate the tuning of LMI coefficients and study the resulting close-loop eigenvalues and time domain performance. It is concluded that the LMI method can find proper control gains under specified communication limitation and successfully stabilize the MTDC system under test. It is also demonstrated that the proposed method can be easily configured into various system and control topology settings.

To further understand how internal dynamics of the system is influenced by LMI parameters, eigenvalues are grouped and studied using the participation factor technique. By tracking the movement of poles, we reveal the two key pairs of trade-off in a MTDC system: 1. trade-off between control performance and effort; 2. trade-off between local real power tracking and system voltage regulation. We conclude that the LMI method can find a balance in both, and show how each can be adjusted through LMI parameters: the former by tuning weights in cost function and the later by adjusting elements in parameter matrix **H**. A detailed tuning procedure is then summarized and verified under different control schemes.

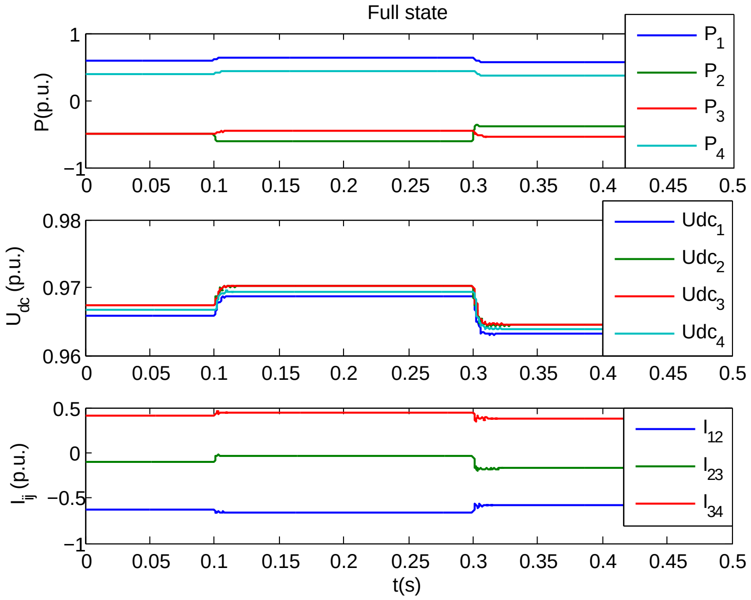

(a)

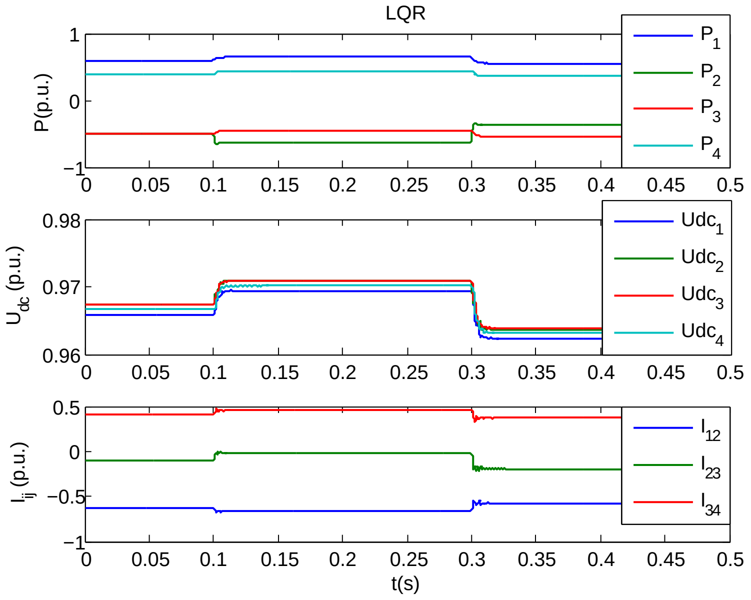

(b)

Figure 29: Simulation result, **K** solved by (a)LMI method (b)LQR method

The capability of different control topologies is also studied and compared. While distributed controller can already stabilize the system, it shows limited capability in pole adjustment due to the reduced level of controllability. When communication is allowed between terminals, the LMI algorithm is able to coordinate the terminals to greatly reduce oscillation and increase control of eigenvalue positions.

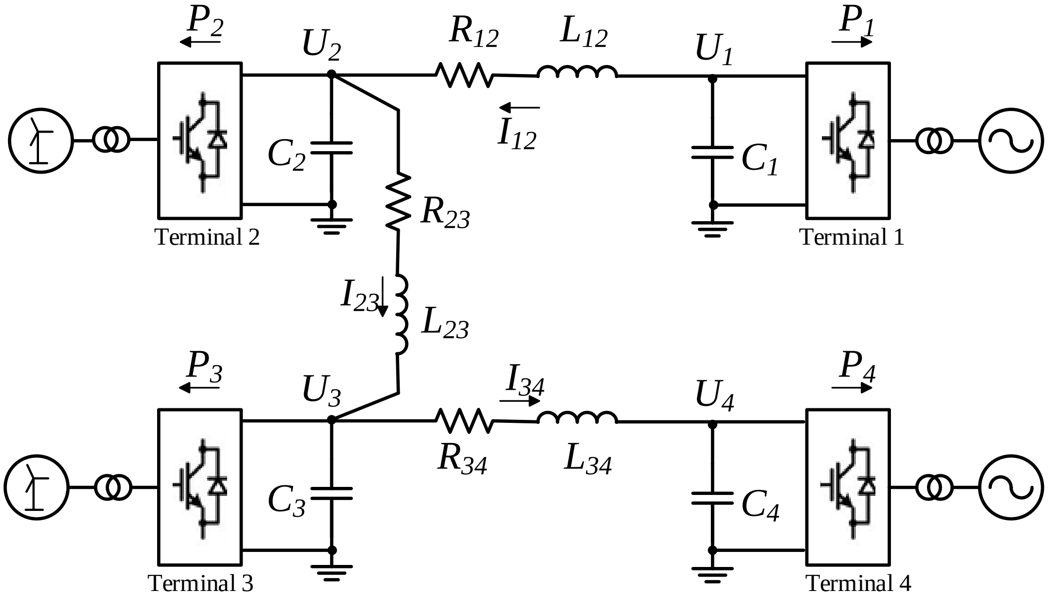

Figure 30: Study case of a four-terminal system with wind generation.

6.0 CASE STUDY OF A FOUR-TERMINAL SYSTEM FOR OFFSHORE WIND INTEGRATION

In this chapter, we study a second test case of off-shore wind integration. It is a variation of the test system investigated in Chapter 5. Figure 30 shows the setup of the system, terminal 1 and 4 are connected to AC grids while terminal 2 and 3 are connected to wind farms. The system parameters and operating points are shown in Table 7. All per unit values are based on nominal value of 100MW, 150kV and 50Hz. As it can be seen from operating power, the AC grid side terminals are exporting power from the DC system, while wind farm side terminals are injecting power. Operating voltage and power are solved by the numerical routine described in Section 3.3.

Table 7: Table of parameters for the offshore wind integration test case

DC grid parameters			
Parameter	Value (p.u.)	Parameter	Value (p.u.)
R_{12}	0.0022	L_{12}	0.0070
R_{23}	0.0011	L_{23}	0.0035
R_{34}	0.0018	L_{34}	0.0056
$C_k,\ k = 1, \dots, 4$	11		
Operating point			
Parameter	Value (p.u.)	Parameter	Value (p.u.)
P_{10}	0.6000	U_{10}	0.9659
P_{20}	-0.5000	U_{20}	0.9673
P_{30}	-0.5000	U_{30}	0.9674
P_{40}	0.3988	U_{40}	0.9667
Power control close-loop parameters			
Parameter	Value	Parameter	Value
$\tau_{dk},\ k = 1, 4$	1 ms	$\tau_{qk},\ k = 1, 4$	1 ms
$\tau_k,\ k = 2, 3$	0.6 s		

Compared to Table 1 in Chapter 5, the main difference in this model is the subsystem of terminal 2 and 3 are replaced by simplified wind farm model, which has much slower power dynamics due to the large mechanical inertia of wind turbines [36, 52, 53, 54].

6.1 NATURAL DYNAMICS ANALYSIS

Same as in Chapter 5, eigenvalue and participation factor of the open-loop system are studied to understand its dynamic response. Remind that the open-loop system is defined as the

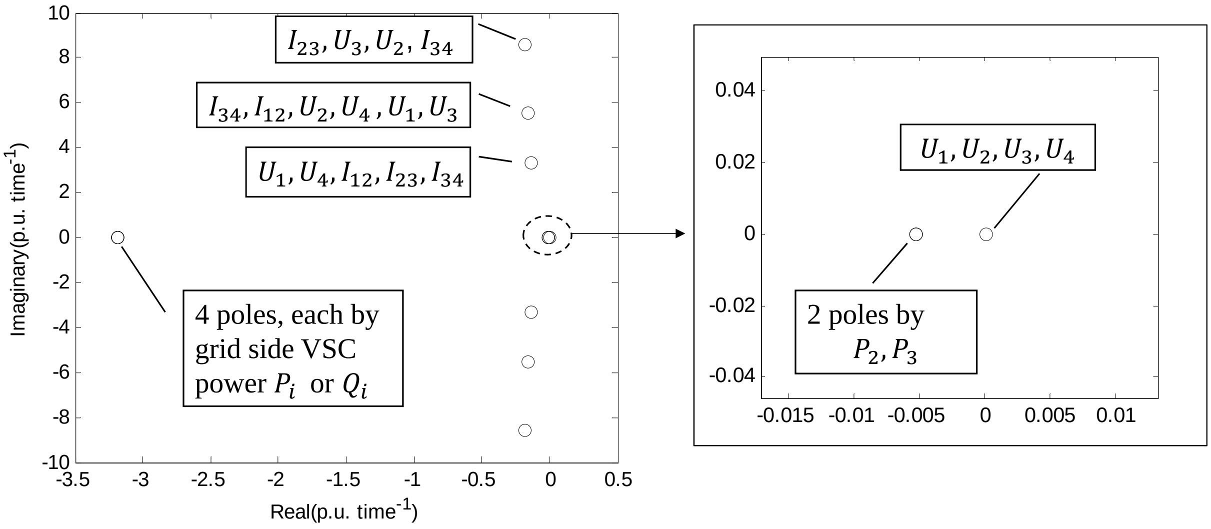

Figure 31: Eigenvalues of the offshore wind integration system, and their participating states

MTDC grid without system level power balancing control. Its input, $\begin{bmatrix} \cdots & \Delta P_k^* & \cdots \end{bmatrix}^\top$, are adjustment to the scheduled real power references. Figure 31 shows eigenvalues of the system's minimal realization. Remind that all eigenvalues are plotted in per-unitized scale, so real and imaginary axises are scaled by $2\pi f_0$, in which f_0 is the nominal frequency. Related states are listed in the attached text boxes of each real or complex conjugate pair of eigenvalues. From Figure 31, we can learn the following about the natural dynamics of the system:

- On the far left, there are 4 overlapping real poles. These fast first-order modes each independently represents a local close-loop control on d or q axis of the grid side converters.
- The three complex conjugate pairs are related to the natural dynamics of DC grid. These modes are the same as the test case in Chapter 5, because the same DC network is used.
- There are multiple poles near origin, which can be seen in the zoom-in plot on the right. The one marginal stable pole is related to DC voltages, which are not yet regulated. The rest overlapping poles are the very slow local mode of the wind generation side terminals.

6.2 POWER BALANCING CONTROL DESIGN

In the following sections, we use the proposed LMI-based method to design control for this test case. The following operation modes of wind integration MTDC system are considered:

Mode 1 Wind side terminals are fully in maximum power point tracking(MPPT) control, only grid side terminals contribute to power balancing and DC voltage regulation. This is the most common scheme for maximum power integration.

Mode 2 Only wind side terminals are in charge of power balancing. This is a safe mode to maintain system stability when there is a fault on grid side. It requires wind side VSCs operating on a bias from the maximum power point to reserve some generation capacity.

Mode 3 All terminals are contributing to voltage regulation. This scheme is for high penetration rate or limited grid side stability, such as a weak AC connection. It reduces the disturbance on grid side by sacrificing some efficiency on the wind side.

These control schemes can be easily modeled and design using our configurable controller model proposed in Chapter 4. Both mode 1 and 2 are partially participating voltage regulation schemes that can be specified using nonzero pattern of $\mathbf{K}$ similar in Section 5.2. And mode 3 is a standard distributed control which can be specified by nonzero pattern as Figure 13(a). The corresponding control gain matrix $\mathbf{K}$ can then be solved efficiently using the proposed LMI-based method. Close-loop analysis and simulation results for each operating mode are discussed in the following sections.

6.2.1 Grid side voltage regulation

Figure 32 shows the analysis on close-loop eigenvalues. To simplify the discussion, only LMI weight coefficient a_1 is swiped. And all other parameters are fixed. When a_1, which is the weight of stability boundary, is increased, the LMI algorithm is trying to find larger margin between the overall eigenvalues and the imaginary axis. From Figure 32, we can learn the following trends of close-loop dynamics under operating mode 1:

- On the right of Figure 32(a), one can see the slow real poles of wind side VSCs are untouched in close-loop. This indicates that their local MPPT control is not influenced.

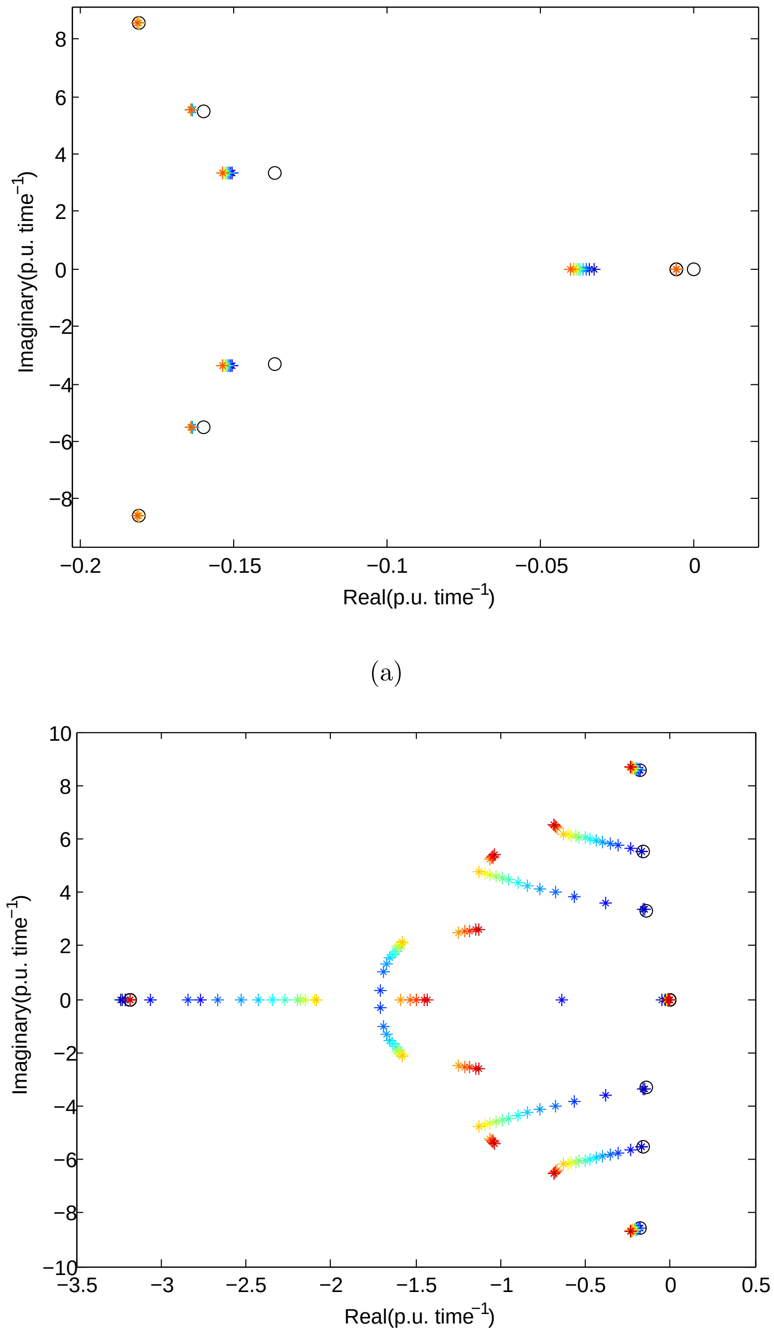

(a)

(b)

Figure 32: In operation mode 1, close-loop eigenvalues when weight coefficient a_1 increases: (a) a_1 from 0.001(blue) to 0.01(red) (b) a_1 from 0.01(blue) to 0.1(red)

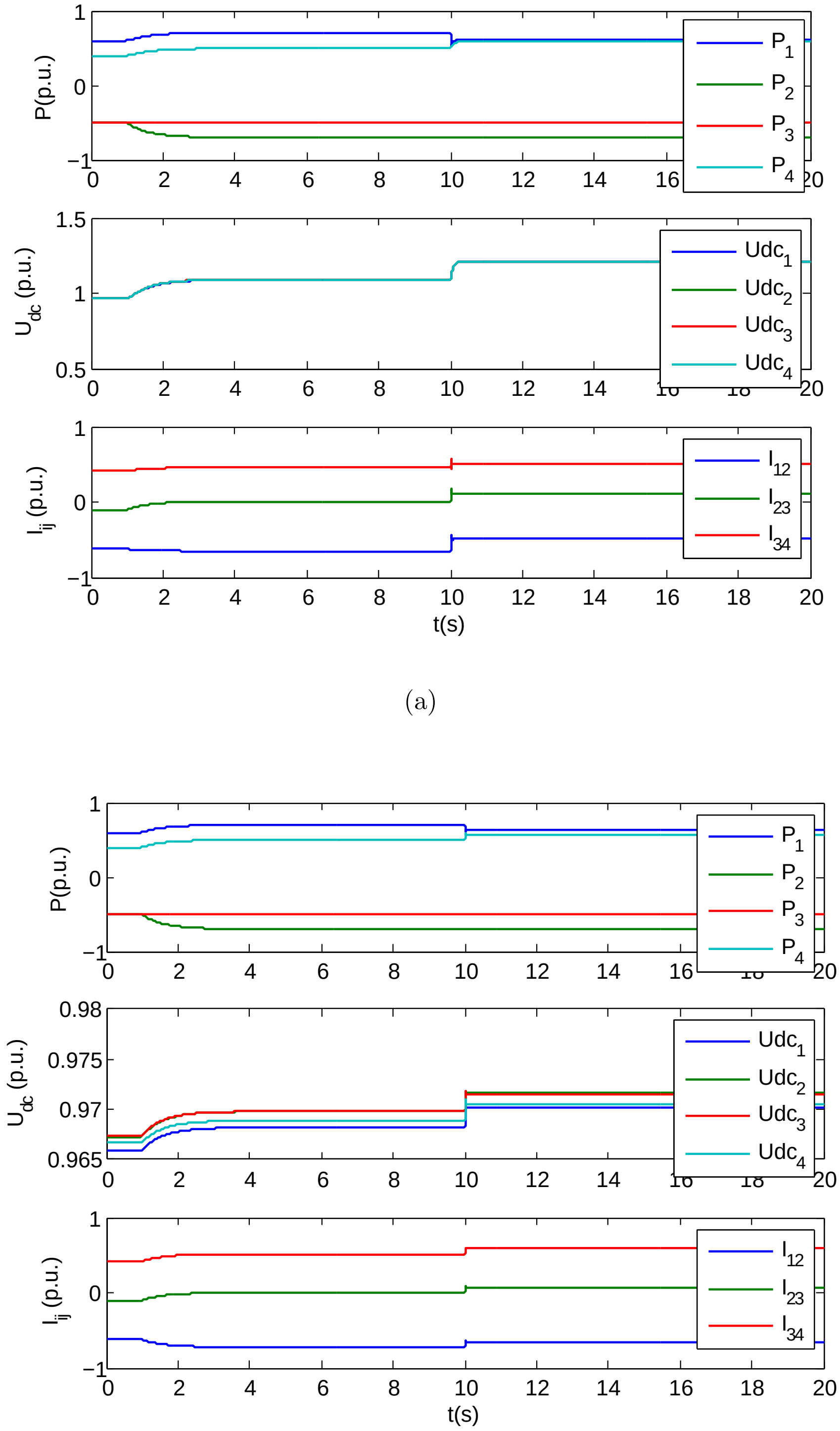

(a)

(b)

Figure 33: Simulation of operation mode 1: (a) $a_1 = 0.01$ (b) $a_1 = 0.07$

This is expected in this control scheme as terminal 2 and 3 are not participating in the system level control.

- For the critical real pole of DC voltages, it moves from marginal to stable as soon as a small voltage regulation control gain kicks in (see the right of Figure 32(a)). As a_1 getting larger in Figure 32(b). it moves left until joining with a grid side power related eigenvalue and formulate a new complex conjugate pair.

- From the fast real modes related to grid side VSC power control, we can again see in Figure 32(b) the trade-off between local and global control objectives. They are getting slower as the grid side VSCs contributing more to power balancing. Their local tracking of scheduled power transmission also expects larger bias.

- The 3 pairs of complex eigenvalues, which corresponds to higher order DC dynamics, are moving left but not showing the same level of change. The two pairs closer to real axis are much more sensitive to larger a_1. While the rest pair hardly moves. This is because the limited controllability with two terminals missing the global control, same as we concluded in Chapter 5

- When a_1 is increased above a certain point, the faster modes are turning around and move towards right. This implies that the capacities of grid side VSCs is almost used up. And the LMI algorithm can only sacrifice some more faster mode to keep dragging the slower modes leftwards. However, due to the limited controllability, we can get little performance improvement. So we should avoid a_1 entering the orange and red region.

Time domain simulation is presented in Figure 33 for two a_1 values. Figure 33(a) uses control gains solved when $a_1 = 0.01$, the corresponding eigenvalues are the dark blue points in Figure 32(b). And Figure 33(b) uses control gains solved when $a_1 = 0.07$, which is corresponding to yellow poles in Figure 32(b).

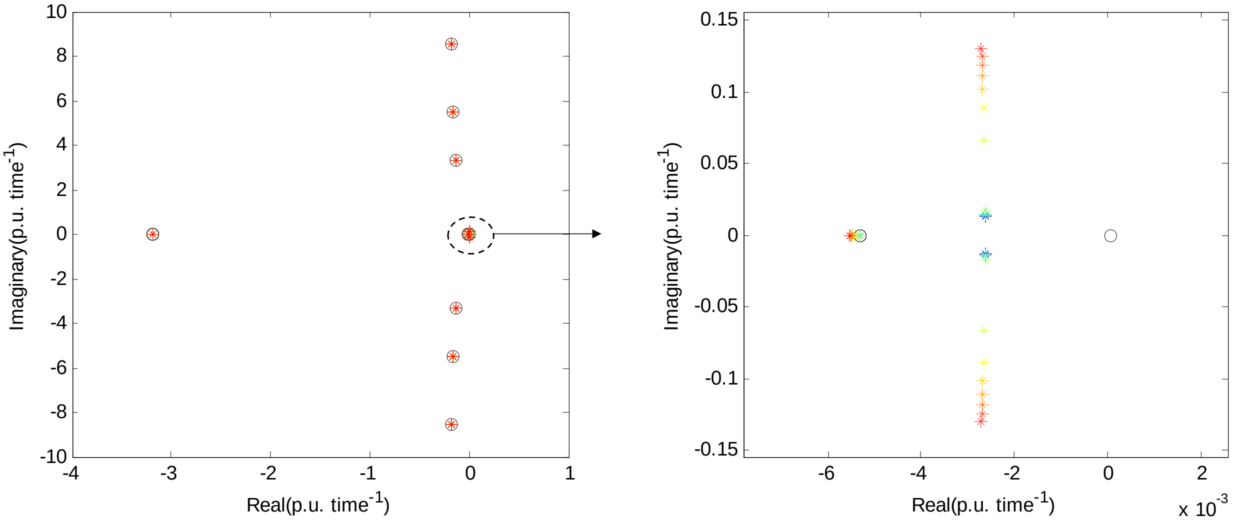

Figure 34: In operation mode 2, close-loop eigenvalues when weight coefficient a_1 increases from 0.001(blue) to 0.05(red).

6.2.2 Wind side voltage regulation

Figure 34 shows the analysis on close-loop eigenvalues for operating mode 2. Same as in mode 1, only LMI weight coefficient a_1 is swiped. Warmer color indicates larger value of a_1. From Figure 34, we can learn the following about close-loop dynamics under operating mode 2:

- On the most left, the fast real poles of grid side VSCs are not changed in close-loop. This shows that terminal 1 and 4's local control is not influenced because they are not participating in the system level control in this operation mode.

- Due to the limitation of response speed. Wind side terminals alone have no influence on the eigenvalues that are faster than themselves. That is why one can hardly observe any change in the full plot on the left. The natural oscillation poles corresponding to DC currents cannot be improved in this operating mode regardless how large the control effort is given by wind side terminals, because these dynamics are much faster.

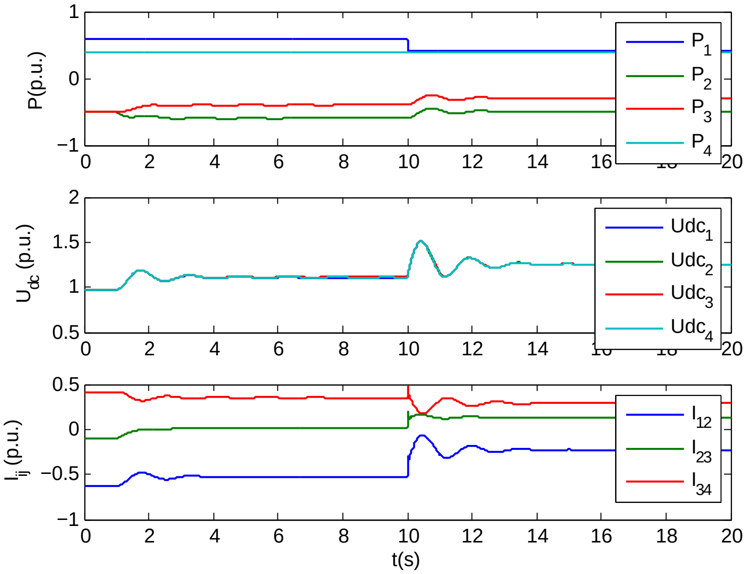

(a)

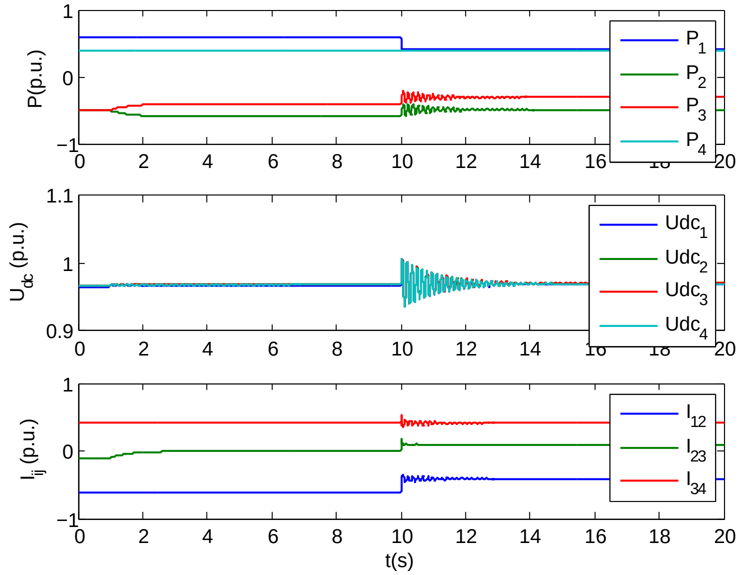

(b)

Figure 35: Simulation of operation mode 2: (a) $a_1 = 0.001$ (b) $a_1 = 0.05$

- The only eigenvalue can be improved is the critical marginal stable real pole. This mode cannot get faster then the dynamics of wind side VSCs. As a result we cannot expect good performance in this control scheme. But this safe mode does help stabilize the system when grid side terminals cannot.

Time domain simulation is presented in Figure 35 for two a_1 values. Figure 35(a) uses control gains solved when $a_1 = 0.001$, the corresponding eigenvalues are the blue points in Figure 34. And Figure 35(b) uses control gains solved when $a_1 = 0.05$, which is corresponding to red poles in Figure 34.

Note that when there are multiple grid connecting terminals, the chance that the MTDC system is regulated solely by wind side VSCs is very small. This scenario can be viewed as a worst case situation for grid side failure.

6.2.3 Full participating voltage regulation

Figure 36 shows the analysis on close-loop eigenvalues for operating mode 2. Again, in this section, only LMI weight coefficient a_1 is swiped.

It can be seen that the eigenvalue movements in Figure 36 is almost identical to Figure 32. This is because the slow wind side VSCs cannot improve any dynamic modes that are faster than themselves, as we have shown in Figure 34.

The only difference can be observed is on the critical real pole. Thus the zoom-in plots are compared in Figure 37. In grid side voltage regulation (Figure 37(a)), the critical pole is getting faster and faster towards left when a_1 increases. However, when wind side VSCs join the effort, this dynamic mode splits into two real poles, with one dragged towards the slower wind turbine dynamics. The more wind side terminals participate, the slower this pole will get.

This shows that when grid side terminals have enough capacity, bring in the wind side terminals to system level control is not a good idea in term of performance.

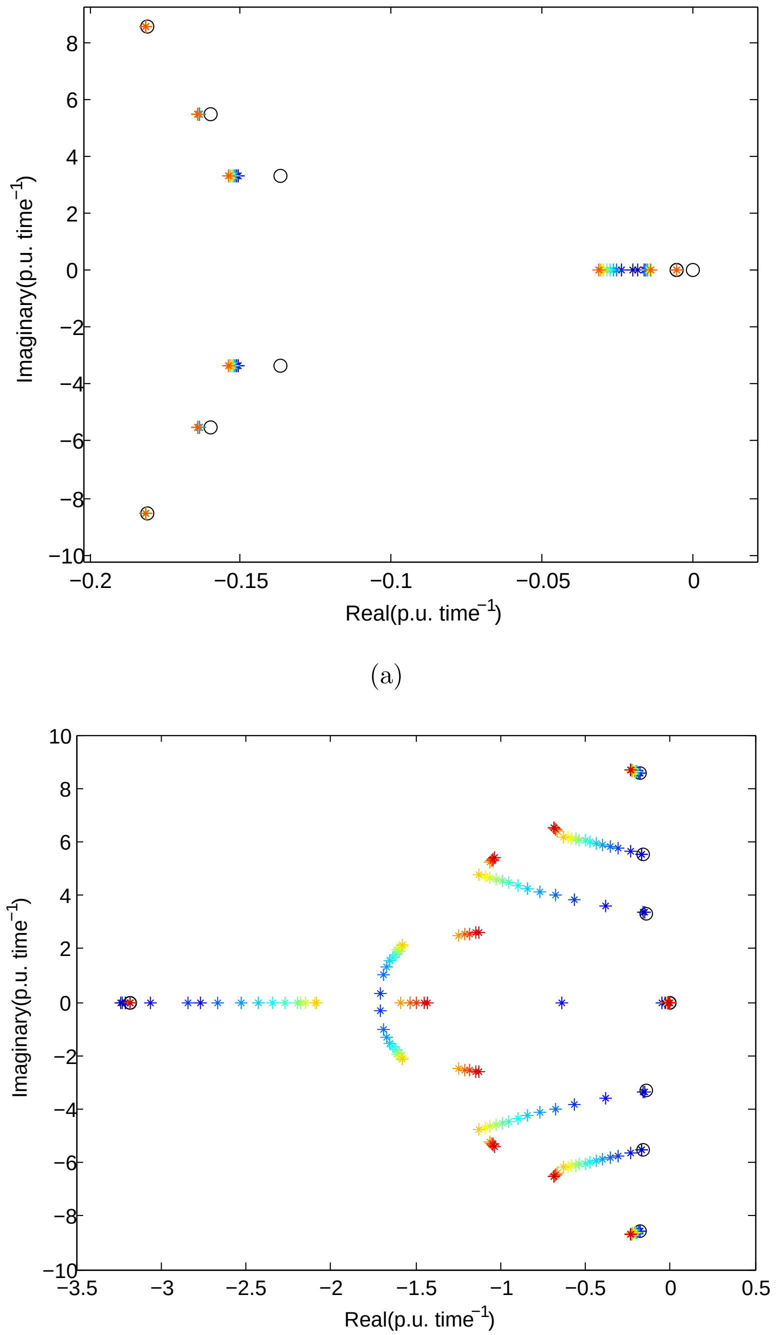

(a)

(b)

Figure 36: In operation mode 3, close-loop eigenvalues when weight coefficient a_1 increases: (a)a_1 from 0.001(blue) to 0.01(red) (b)a_1 from 0.01(blue) to 0.1(red)

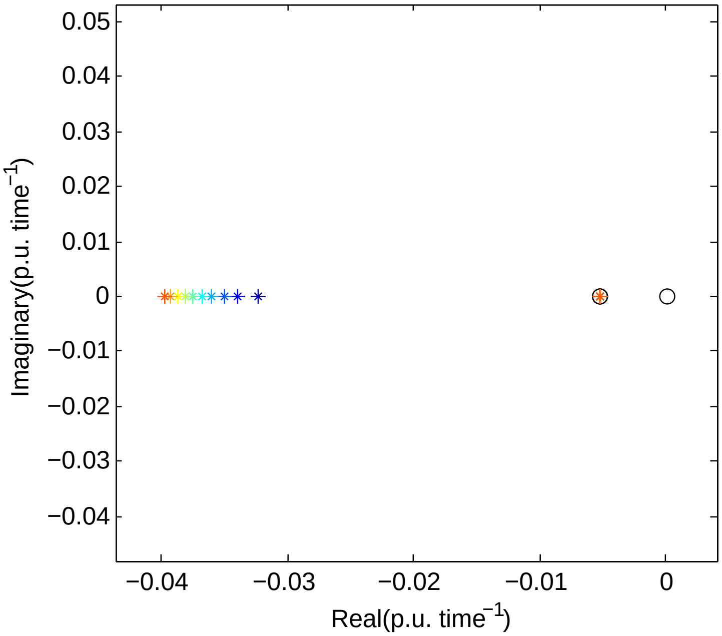

(a)

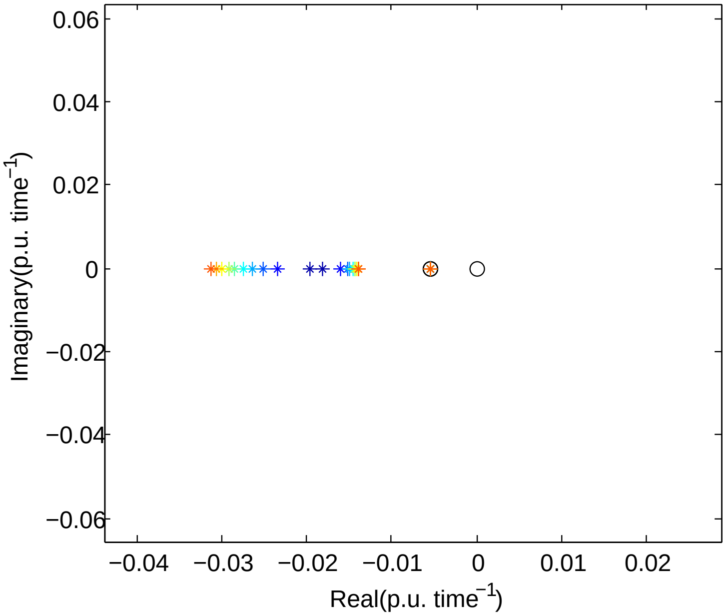

(b)

Figure 37: Compare critical poles in operation mode 1(a) and 3(b), when weight coefficient a_1 changes from 0.001(blue) to 0.01(red)

6.3 SUMMARY

In this chapter, a 4-terminal MTDC system for off-shore wind integration is studied. It is a variance of the case used in Chapter 5. The slow local dynamics of wind farm connected VSC is modeled using our two-stage modeling procedure. The proposed control design method is then applied to address 3 possible operation modes of wind integration system. Close-loop performance of the three control scheme is studied through analytical analysis and simulation.

7.0 CONCLUSIONS AND FUTURE WORK

7.1 CONCLUSIONS

VSC-MTDC systems are showing great potential on several crucial grid applications: On transmission level, integrating massive renewables; and provide better isolation between different AC areas On micro-grid level, it can serve as an efficient backbone to tie in distributed generation and storage to loads. Compared to the maturing technology on device level, more research effort is needed on the system and operation level.

In this thesis, the modeling and control problems for a general VSC-MTDC are investigated. A comprehensive solution for MTDC systems from modeling to control design is introduced. Our methodology contains:

- A two-stage modeling procedure derived for arbitrary MTDC setups. It is a small signal average modeling method in state space. The first stage models the local dynamics, while system dynamics and coupling are considered in the second stage. The procedure can be applied to various MTDC applications.
- A reconfigurable controller that can represent different control structure and communication constraints. In our case study, we have shown that multiple existing control strategies in literature can be described by our control formulation.
- A LMI-based control design algorithm. The control problem is formulated into a standard LMI problem, which can be efficiently solved by multiple convex optimization tools. Detailed guidelines on LMI parameter tuning is introduced and demonstrated in multiple use cases

We have demonstrated in our test cases that the proposed method can help one easily explore a large design space of various system setups, applications, and control strategies. Benefit of the proposed method includes:

- Solve different MTDC problems in one unified procedure: modeled and formulated into the same form, and solved by the same optimization method.
- Transfer controller tuning problem from a large set of control gains to a few LMI parameters with clear performance indication. Make the complex MIMO control problem more manageable.

Two MTDC systems for different application are studied. For each application, multiple control structures are designed and evaluated. These forms a good set of use cases for the proposed method. From these examples, we obtain the following understanding for MTDC control problems:

- There are two key pairs of trade-off in a MTDC system: 1. trade-off between control performance and effort; 2. trade-off between local real power tracking and system voltage regulation. We conclude that the LMI method can find a balance in both, and show how each can be adjusted through LMI parameters: the former by tuning weights in cost function and the later by adjusting elements in parameter matrix $\mathbf{H}$. The detailed tuning procedure is summarized and verified under different use cases.
- The capability of different control topologies is also studied and compared. While distributed controller can already stabilize the system, it shows limited capability in pole adjustment due to the reduced level of controllability. When communication is allowed between terminals, the LMI algorithm is able to coordinate the terminals to greatly reduce oscillation and increase control of eigenvalue positions.
- When fast and slow VSC subsystems co-exist in one MTDC system. The slow ones won't contribute to the system dynamics that is faster then itself. Natural dynamics of the system can only be changed by a terminal whose local control is faster.

7.2 FUTURE WORK

The following is a list of possible future work:

- Formulate and solve secondary DC voltage control and DC power flow control using the proposed control design method. Both problems are proved to be very important in AC grid, and could be useful in an MTDC system when its scale gets larger and topology gets more complex. The general control architecture is supported by our controller formulation.
- Evaluate the change of system's natural dynamics in different operating points. Current small signal analysis is only good for a specified operating condition. However, a key potential of MTDC systems is to support different power transmission or deliver direction. Understand the influence of changing operating point and design control accordingly can be a promising direction for advanced MTDC systems.

BIBLIOGRAPHY

[1] G. Reed, B. Grainger, A. Sparacino, and Z.-H. Mao, “Ship to grid: Medium-voltage DC concepts in theory and practice,” *IEEE Power and Energy Magazine*, vol. 10, no. 6, pp. 70 –79, Nov. 2012.

[2] S. Muyeen, R. Takahashi, and J. Tamura, “Operation and control of HVDC-connected offshore wind farm,” *IEEE Transactions on Sustainable Energy*, vol. 1, no. 1, pp. 30 –37, Apr. 2010.

[3] L. Xu, L. Yao, and M. Bazargan, “DC grid management of a multi-terminal HVDC transmission system for large offshore wind farms,” in *SUPERGEN ’09 International Conference on Sustainable Power Generation and Supply*, Apr. 2009, pp. 1 –7.

[4] L. Xu, B. Williams, and L. Yao, “Multi-terminal dc transmission systems for connecting large offshore wind farms,” in *2008 IEEE Power and Energy Society General Meeting - Conversion and Delivery of Electrical Energy in the 21st Century*, july 2008, pp. 1 –7.

[5] L. Xu, L. Yao, and C. Sasse, “Grid integration of large DFIG-based wind farms using VSC transmission,” *IEEE Transactions on Power Systems*, vol. 22, no. 3, pp. 976 –984, Aug. 2007.

[6] W. Lu and B.-T. Ooi, “Optimal acquisition and aggregation of offshore wind power by multiterminal voltage-source HVDC,” *IEEE Transactions on Power Delivery*, vol. 18, no. 1, pp. 201 – 206, Jan. 2003.

[7] N. R. Chaudhuri, R. Majumder, and B. Chaudhuri, “System frequency support through multi-terminal dc (MTDC) grids,” *IEEE Transactions on Power Systems*, vol. PP, no. 99, p. 1, 2012.

[8] J. Dai, Y. Phulpin, A. Sarlette, and D. Ernst, “Coordinated primary frequency control among non-synchronous systems connected by a multi-terminal high-voltage direct current grid,” *IET Generation, Transmission & Distribution*, vol. 6, no. 2, pp. 99 –108, Feb. 2012.

[9] T. Haileselassie and K. Uhlen, “Primary frequency control of remote grids connected by multi-terminal HVDC,” in *2010 IEEE Power and Energy Society General Meeting*, july 2010, pp. 1 –6.

[10] D. Van Hertem, M. Ghandhari, and M. Delimar, “Technical limitations towards a supergrid: A european prospective,” in *2010 IEEE International Energy Conference and Exhibition*, Dec. 2010, pp. 302 –309.

[11] J. Blau, “Europe plans a north sea grid,” *IEEE Spectrum*, vol. 47, no. 3, pp. 12 –13, Mar. 2010.

[12] R. Wu, S. B. Dewan, and G. R. Slemon, “Analysis of an ac-to-dc voltage source converter using PWM with phase and amplitude control,” *IEEE Transactions on Industry Applications*, vol. 27, no. 2, pp. 355–364, 1991.

[13] V. Blasko and V. Kausa, “A new mathematical model and control of a three-phase ac-dc voltage source converter,” *IEEE Transactions on Power Electronics*, vol. 12, no. 1, pp. 116–123, 1997.

[14] A. Yazdani and R. Iravani, *Voltage-Sourced Converters in Power Systems: Modeling, Control, and Applications.* Hoboken, NJ, USA.: John Wiley & Sons, Inc., 2010.

[15] H. Clark, A.-A. Edris, M. El-Gasseir, K. Epp, A. Isaacs, and D. Woodford, “Softening the blow of disturbances,” *IEEE Power and Energy Magazine*, vol. 6, no. 1, pp. 30 –41, January-February 2008.

[16] S. Cole, J. Beerten, and R. Belmans, “Generalized dynamic VSC MTDC model for power system stability studies,” *IEEE Transactions on Power Systems*, vol. 25, no. 3, pp. 1655 –1662, Aug. 2010.

[17] F. Bianchi and O. Gomis-Bellmunt, “Droop control design for multi-terminal VSC-HVDC grids based on lmi optimization,” in *2011 50th IEEE Conference on Decision and Control and European Control Conference (CDC-ECC).* IEEE, 2011, pp. 4823–4828.

[18] E. Prieto-Araujo, F. Bianchi, A. Junyent-Ferre, and O. Gomis-Bellmunt, “Methodology for droop control dynamic analysis of multiterminal VSC-HVDC grids for offshore wind farms,” *IEEE Transactions on Power Delivery*, vol. 26, no. 4, pp. 2476 –2485, Oct. 2011.

[19] N. R. Chaudhuri and B. Chaudhuri, “Adaptive droop control for effective power sharing in multi-terminal DC (MTDC) grids,” *IEEE Transactions on Power Systems*, vol. PP, no. 99, p. 1, 2012.

[20] B. Berggren, R. Majumder, C. Sao, and K. Linden, “Method and control device for controlling power flow within a dc power transmission network,” Jan. 5 2012, WO Patent WO/2012/000549.

[21] M. Ilic, “From hierarchical to open access electric power systems,” *Proceedings of the IEEE*, vol. 95, no. 5, pp. 1060 –1084, May 2007.

[22] P. Kundur and G. K. Morison, “Power system control: requirements and trends in the new utility environment,” in *Bulk Power System Dynamics and Control–IV Restructuring*, pp. 257–263.

[23] J. Baillieul and P. Antsaklis, “Control and communication challenges in networked real-time systems,” *Proceedings of the IEEE*, vol. 95, no. 1, pp. 9–28, 2007.

[24] D. D. Siljak and A. I. Zecevic, “Control of large-scale systems: beyond decentralized feedback,” *Annual Reviews in Control*, vol. 29, pp. 169–179, 2005.

[25] A. I. Zecevic and D. D. Siljak, *Control of Complex Systems: Structural Constraints and Uncertainty*. Springer, 2010.

[26] H. Wu, “Decentralized adaptive robust control for a class of large scale systems with uncertainties in the interconnections,” *International Journal of Control*, vol. 76, pp. 253–265, 2003.

[27] H. Tamura and T. Yoshikawa, *Large-Scale Systems Control and Decision Making*. New York: Marcel Dekker, 1990.

[28] M. Jamshidi, *Large-Scale Systems: Modelling, Control and Fuzzy Logic*. Upper Saddle River, NJ, USA: Prentice-Hall, 1997.

[29] N. Sandell and M. Athans, “Solution of some nonclassical lqg stochastic decision problems,” *IEEE Transactions on Automatic Control*, vol. AC-19, no. 2, pp. 108–116, 1974.

[30] R. Bellman, “Special issue on large systems,” *IEEE Transactions on Automatic Control*, vol. AC-19, no. 5, pp. 465–465, 1974.

[31] N. Sandell, P. Varaiya, M. Athans, and M. G. Safonov, “Survey of decentralized control methods for large scale systems,” *IEEE Transactions on Automatic Control*, vol. AC-23, no. 2, pp. 108–128, 1978.

[32] P. Antsaklis and J. Baillieul, “Special issue on networked control systems,” *IEEE Transactions on Automatic Control*, vol. 49, no. 9, pp. 1421–1423, 2004.

[33] ——, “Special issue on technology of networked control systems,” *Proceedings of the IEEE*, vol. 95, no. 1, pp. 5–8, 2007.

[34] N. Chaudhuri, R. Majumder, B. Chaudhuri, and J. Pan, “Stability analysis of VSC MTDC grids connected to multimachine ac systems,” *IEEE Transactions on Power Delivery*, vol. 26, no. 4, pp. 2774 –2784, Oct. 2011.

[35] L. Zhang, L. Harnefors, and H.-P. Nee, “Interconnection of two very weak ac systems by VSC-HVDC links using power-synchronization control,” *IEEE Transactions on Power Systems*, vol. 26, no. 1, pp. 344 –355, Feb. 2011.

[36] N. P. Strachan and D. Jovcic, "Stability of a variable-speed permanent magnet wind generator with weak ac grids," *IEEE Transactions on Power Delivery*, vol. 25, no. 4, pp. 2779–2788, 2010.

[37] K. Areerak, S. Bozhko, G. Asher, and D. Thomas, "DQ-transformation approach for modelling and stability analysis of AC-DC power system with controlled PWM rectifier and constant power loads," in *EPE-PEMC 2008 13th Power Electronics and Motion Control Conference*, Sep. 2008, pp. 2049 –2054.

[38] S. R. Sanders, J. M. Noworolski, X. Z. Liu, and G. C. Verghese, "Generalized averaging method for power conversion circuits," *IEEE Transactions on Power Electronics*, vol. 6, no. 2, pp. 251–259, 1991.

[39] C. Schauder, M. Gernhardt, E. Stacey, T. Lemak, L. Gyugyi, T. Cease, and A. Edris, "Operation of ±100 MVAr TVA STATCON," *IEEE Transactions on Power Delivery*, vol. 12, no. 4, pp. 1805–1811, 1997.

[40] G. Beccuti, G. Papafotiou, and L. Harnefors, "Multivariable optimal control of HVDC transmission links with network parameter estimation for weak grids," *IEEE Transactions on Control Systems Technology*, vol. PP, no. 99, pp. 1–1, 2013.

[41] M. Durrant, H. Werner, and K. Abbott, "Model of a VSC HVDC terminal attached to a weak ac system," in *Proceedings of 2003 IEEE Conference on Control Applications*, vol. 1, Jun. 2003, pp. 178 – 182 vol.1.

[42] A. Farag, M. Durrant, H. Werner, and K. Abbott, "Robust control of a VSC HVDC terminal attached to a weak ac system," in *Proceedings of 2003 IEEE Conference on Control Applications*, vol. 1, Jun. 2003, pp. 173 – 177 vol.1.

[43] L. Zhang and H.-P. Nee, "Multivariable feedback design of VSC-HVDC connected to weak ac systems," in *2009 IEEE Bucharest PowerTech*, jul 2009, pp. 1 –8.

[44] P. Mitra, L. Zhang, and L. Harnefors, "Offshore wind integration to a weak grid by VSC-HVDC links using power-synchronization control: A case study," *IEEE Transactions on Power Delivery*, vol. PP, no. 99, pp. 1–1, 2013.

[45] L. Tang and B.-T. Ooi, "Elimination of harmonic transfer through converters in VSC-based multiterminal dc systems by ac/dc decoupling," *IEEE Transactions on Power Delivery*, vol. 23, no. 1, pp. 402–409, 2008.

[46] L. Xu and L. Yao, "DC voltage control and power dispatch of a multi-terminal HVDC system for integrating large offshore wind farms," *IET Renewable Power Generation*, vol. 5, no. 3, pp. 223 –233, May 2011.

[47] M. Grant and S. Boyd, "CVX: Matlab software for disciplined convex programming, version 2.1," http://cvxr.com/cvx, Mar. 2014.

[48] J. Löfberg, "YALMIP : A toolbox for modeling and optimization in MATLAB," in *Proceedings of the CACSD Conference*, Taipei, Taiwan, 2004. [Online]. Available: http://users.isy.liu.se/johanl/yalmip

[49] S. Boyd, L. El Ghaoui, E. Feron, and V. Balakrishnan, "Linear matrix inequalities in systems and control theory," *Philadelphia, PA:SIAM, 1994*, 1994.

[50] F. Palacios-Quinonero and J. Rossell Garriga, "Decentralized control with information structure constraints," in *15th International Workshop on Dynamics and Control, Barcelona, Spain*, 2009, pp. 111 – 118.

[51] O. Gomis-Bellmunt, J. Liang, J. Ekanayake, and N. Jenkins, "Voltage-current characteristics of multiterminal HVDC-VSC for offshore wind farms," *Electric Power Systems Research*, vol. 81, no. 2, pp. 440–450, 2011.

[52] J. A. Baroudi, V. Dinavahi, and A. M. Knight, "A review of power converter topologies for wind generators," *Renewable Energy*, vol. 32, no. 14, pp. 2369 – 2385, 2007.

[53] A. Rolan, A. Luna, G. Vazquez, D. Aguilar, and G. Azevedo, "Modeling of a variable speed wind turbine with a permanent magnet synchronous generator," in *IEEE International Symposium on Industrial Electronics*, july 2009, pp. 734 –739.

[54] C. Tang, M. Pathmanathan, W. L. Soong, and N. Ertugrul, "Effects of inertia on dynamic performance of wind turbines," in *Power Engineering Conference, 2008. AUPEC'08. Australasian Universities.* IEEE, Dec 2008, pp. 1–6.